The Dissertation Committee for Arvind Reddy Battula Certifies that this is the approved version of the following dissertation:

Optical Near-field Effects for Submicron Patterning and Plasmonic Optical Devices

Committee:

Shaochen Chen, Supervisor

John R. Howell

Gennady Shvets

Ofodike A Ezekoye

Li Shi

Optical Near-field Effects for Submicron Patterning and Plasmonic Optical Devices

by

Arvind Reddy Battula, B. Tech.; M.S.

Dissertation

Presented to the Faculty of the Graduate School of

The University of Texas at Austin

in Partial Fulfillment

of the Requirements

for the Degree of

Doctor of Philosophy

The University of Texas at Austin

December, 2007

Dedication

To my daughter, wife and parents

Acknowledgements

First, I would like to sincerely express thanks to my advisor, Prof. Shaochen Chen, for his continuous support and guidance in my doctoral study. I especially thank him for his encouragement, understanding and open-mindedness. He has allowed me the freedom to work independently and without his help my PhD would not be successful.

I also thank my committee members, Prof. John R. Howell, Prof. Gennday Shvets, Prof. Ofodike A. Ezekoye, Prof. Li Shi for serving on my dissertation committee and providing advices on my dissertation.

It has been a pleasure to work with past and present members of Prof. Chen's Nano-Opto-Bio Engineering Lab (NOBEL) at the University of Texas at Austin, particularly Dr. Senthil Theppakutai, Dr. Yi Lu, Dr. Dongbing Shao, David Fozdar, Carlos Augilar and Li-Hsin Han. In particular, I would like to Dr. Senthil Theppakutai for helping me learn using lasers and conducting some experiments.

Finally, I would not have been able to finish my PhD without the love, encouragement and support from my family. I would like to thank my wife Deepti for her understanding and support. Also, I appreciate and thank my parents Meena and Ramana and my brother Anand for their unending encouragement. At last, I am very thankful to my friends Mahadevan, Anshuman and Shreenath for their support.

Arvind Reddy Battula

University of Texas at Austin

Austin, TX

Optical Near-field Effects for Submicron Patterning and Plasmonic Optical Devices

Publication No._____

Arvind Reddy Battula, Ph.D.

The University of Texas at Austin, 2007

Supervisor: Shaochen Chen

Metallic films with narrow and deep subwavelength gratings or holes having a converging-diverging channel (CDC) can exhibit enhanced transmission resonances for wavelengths larger than the periodicity of the grating or hole. Using the finite element method, it is shown that by varying the gap size at the throat of a CDC, the spectral locations of the transmission resonance bands can be shifted close to each other and have high transmittance in a very narrow energy band. Additionally, the transmission of light can be influenced by the presence of the externally applied magnetic field **H**. The spectral locations of the transmission peak resonances depend on the magnitude and the direction of **H**. The transmission peaks have blue-shift with the increase in **H**.

A new multilayer thermal emitter has been analyzed in the visible wavelength range. The proposed emitter has large temporal and spatial coherence extending into the far field. The thermal emitter is made up of a cavity that is surrounded by a thin silver grating having a CDC on one side and a one-dimensional (1D) photonic crystal (PhC) on

the other side. The large coherence length is achieved by making use of the coherence properties of the surface waves. Due to the nature of surface waves the new multilayer structure can attain the spectral and directional control of emission with only *p*-polarization. The resonance condition inside the cavity is extremely sensitive to the wavelength, which would then lead to high emission in a very narrow wavelength band.

In addition a new tunable plasmonic crystal (tPLC) was proposed, where the plasmonic or polaritonic mode of a metallic array can be combined with the photonic mode of a hole array in a dielectric slab for achieving negative refraction and still posses an extra degree of freedom for tuning the tPLC as a superlens to operate at different frequencies. The tunability of the single planar tPLC slab is demonstrated numerically for subwavelength imaging (FWHM $0.38\lambda \sim 0.42\lambda$) by just varying the fluid in the hole array, thereby enabling the realization of ultracompact tunable superlens and paving the way for a new class of lens.

An aggressive pursuit for decreasing the minimum feature size in high bandgap materials has lead to various challenges in nanofabrication. However, it is difficult to achieve critical dimensions at sub-wavelength scale using traditional optical lithography. A new technique to create submicron patterns on hard-to-machine materials like silicon carbide (SiC) and borosilicate glass with a laser beam is demonstrated. Here the principle of optical near-field enhancement between the spheres and substrate when irradiated by a laser beam has been used for obtaining the patterning.

Table of Contents

List of Figures

Chapter 1: Near-field optics

1.1 INTRODUCTION

During the past two decades near-field optics has drawn much attention, because it overcomes the diffraction limit of conventional optics. Although, the physics of near-field optics was a well established research area before mid 1970s, its actual and systematic investigation began with the invention of the scanning tunneling microscope (STM) where a weak electric current passes through the tip and surface [1-4]. This STM has inspired many follow-up studies with different surface interaction mechanisms, which in general can be called scanning probe microscopes (SPM).

The optical near-field has been extensively studied in the past decade using the near-field scanning optical microscope (NSOM) [5] which is a combination of SPM and optical field. The strength of the local electromagnetic interaction between a specimen surface and the scanning probe tip is mapped to produce a nanometer scale resolution image. In NSOM the tip and sample surface are at a distance much smaller than the wavelength of the light, but still far from the intrinsic contact. The optical image with super-resolution can be achieved with NSOM due to the fact that in the near-field of matter the electromagnetic fields have both propagating and evanescent fields. It is believed that the latter part of the field has much higher spatial frequency information due to its large wavevector number. The performance of NSOM is dependent on the optical near-field enhancement which is defined as the local maximum field intensity over the incident field intensity and it is dependent on many factors.

The surface limiting a solid body locally modifies the physical properties of many materials and this gives rise to the concept of the near-field. It can be defined as the extension of the field inside a given material to the outside. This is due to the linear,

homogeneous, and isotropic properties of the space-time that impose a continuous variation of the field amplitudes and energies across the interface [4]. Also, the concept of the near-field and far-field has originated from the microwave technology. The near-field can be understood by analyzing the electric and magnetic fields of an element that can be described by equations with three components having different powers of 'r', the distance from the element [6]. The component proportional to '1/r' is called radiation term and it defines the energy flow away from the element. The component with '$1/r^2$' is called induction term and the component with '$1/r^3$' is called the electrostatic field strength term and it represents the electric charge in the element. Among the three components it can be clearly assessed that the '$1/r^2$' and '$1/r^3$' terms are more dominant in the near-field or in the Fresnel zone. On the other hand the '1/r' term is dominant in the far-field. There is no clear boundary between the near-field and far-field. So, it can be imagined that there is a transition region between them.

The amplitude of the near-field decays very rapidly along the direction perpendicular to the interface giving rise to the evanescent nature of the near-field. Hence the surface or interface can be considered as a privileged place to generate, guide, manipulate and detect evanescent waves. There are two important categories for interfacial near-fields. The first corresponds to the spontaneous near-field, i.e., a field produced in one material due to the permanently established field in another material. The other category is surface near-fields that can only be produced by applying an external excitation. Both optical near-fields and surface plasmon polaritons excited at the interface are good illustrations of this category. This second phenomenon has a special interest because they can be manipulated at will by an external operator [4]. In order to engineer and optimize a particular nano-optical field distribution model-based estimates have to be applied to determine the magnitude of the field enhancement factor. In

addition the spatial distribution of the enhancement is also important to understand the field enhancement.

1.2 SURFACE PLASMON POLARITONS

Surface plasmon polaritons (SPPs) are an electromagnetic excitation that propagates in wave like form along the planar interface between a metal and a dielectric medium (Fig. 1.1). The amplitude of SPPs decays exponentially with increasing distance into each medium from the interface. Hence, SPPs can be regarded as surface electromagnetic waves confined to the near vicinity of the dielectric-metal interface. This confinement of the SPPs leads to the enhancement of the electromagnetic fields and has extreme sensitivity to the surface conditions [7]. Devices exploiting this sensitivity of the SPPs are widely used in the chemo- and bio-sensors [8]. The relative ease of manipulating SPPs on surface and its intrinsic two-dimensional nature opens an opportunity for their applications to photonics and optoelectronics for scaling down optical and electronic devices to nanometric dimensions.

Under normal conditions SPPs cannot be excited directly with external light on a smooth metal interface, since its wavevector is greater than the photon wavevector. For the same reason the SPPs propagating on the smooth metal interface cannot be transformed into light in the adjacent dielectric medium. Hence using conventional (far-field) measurements SPPs cannot be observed unless the scattering in light occurs due to surface defects. With the development of SPMs like scanning near-field optical microscopy (SNOM) it became possible to study the SPPs electromagnetic field in the near-field of the surface where it exists [9].

3

1.2.1 Surface plasmon propagation at a metal and dielectric interface

A plasmon is defined as the quanta of the collective excitation of free electrons in solids. In free-electron metals plasma effects are most pronounced. The dielectric constant of metal can be expressed using free electron model as

$$\varepsilon_m(\omega) = 1 - \left(\frac{\omega_p}{\omega}\right)^2 \tag{1.1}$$

where ω_p is the frequency of the bulk longitudinal electron excitations, or plasma frequency. The electromagnetic properties of the metals related to the plasma effects are significantly different from the properties of the ordinary dielectric materials in the frequency range below plasma frequency where the real part of a dielectric constant is negative. The wavevector of light in this frequency range is imaginary, and hence there are no propagating electromagnetic modes in such a medium [9].

A combined excitation of a surface plasmon and a photon is called SPP. Surface plasmon (SP) is the electron plasma oscillation near a metal surface that originated from the broken translational invariance in the direction perpendicular to the surface. The SP frequency (ω_{SP}) on a semi-infinite flat metal surface can be determined from Re[$\varepsilon_m(\omega_{SP})$ = -ε_i, where $\varepsilon_m(\omega)$ is the frequency dependent metal dielectric constant and ε_i is the dielectric constant of the adjacent material. For free-electron metal in contact with a vacuum as the adjacent medium $\omega_{SP} = \dfrac{\omega_p}{\sqrt{2}}$ [9].

The electromagnetic field of a SPP at a metal-dielectric interface can be obtained by applying Maxwell's equations in each medium along the corresponding boundary conditions. The latter expresses the continuity of the tangential components of the electric and magnetic fields across the interface and these fields would vanish infinitely far from the interface. In order to introduce the main parameters in describing SPPs, let us consider a dielectric material with an isotropic, real and positive dielectric constant (ε_d) in

the half space $x_3 > 0$, and a metal with an isotropic, frequency-dependent, complex dielectric function $\varepsilon_m(\omega) = \varepsilon_1(\omega) + i\varepsilon_2(\omega)$ in the half-space $x_3 < 0$ (Fig. 1.1). First a *p*-polarized or transverse magnetic (TM) wave is considered in this structure and it propagates in the x_1-direction. A TM wave has magnetic vector perpendicular to the plane of incidence (the plane defined by the direction of propagation and the normal to the interface).
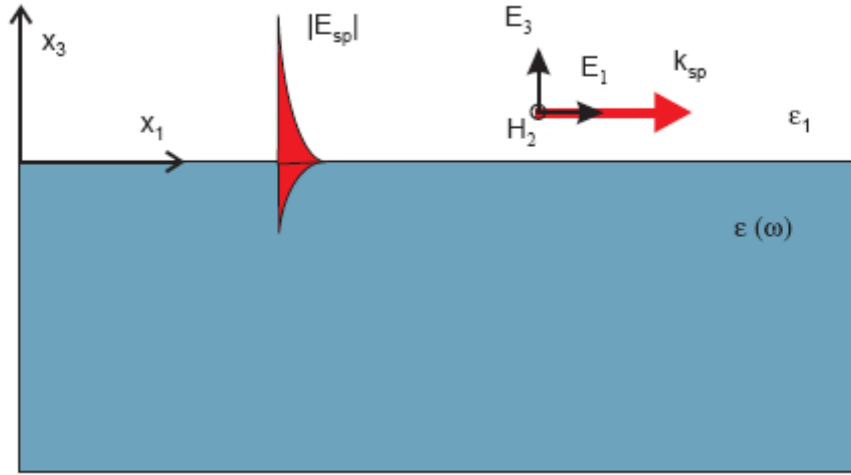
Figure 1.1: Surface plasmon polariton wave form propagation at the metal and dielectric interface [7].

The solution of Maxwell's equations that are wavelike in the x_1-direction can be written as follows

$$H_d(\mathbf{x},t) = (0,A,0)\exp\left[ikx_1 + ik_3^{(d)}x_3 - i\omega t\right]$$

$$E_d(\mathbf{x},t) = -A\frac{c}{i\omega\varepsilon_d}\left(-ik_3^{(d)},0,ik\right)\exp\left[ikx_1 + ik_3^{(d)}x_3 - i\omega t\right] \qquad (1.2)$$

in the region $x_3 > 0$ with 'A' as the amplitude, k and k_3^0 as the wave vector in x_1 and x_2 direction, 'ω' is the frequency and 'c' is the speed of light.

$$H_m(\mathbf{x},t) = (0,B,0)\exp\left[ikx_1 + ik_3^{(m)}x_3 - i\omega t\right]$$

$$E_m(\mathbf{x},t) = -B\frac{c}{i\omega\varepsilon_m(\omega)}\left(-ik_3^{(m)},0,ik\right)\exp\left[ikx_1 + ik_3^{(m)}x_3 - i\omega t\right] \qquad (1.3)$$

in the region $x_3 < 0$. If we now apply Maxwell's equation $\nabla \cdot \mathbf{E} = 0$ then the following equations are obtained

$$E_{x_3 m} = -E_{x_1 m}\frac{k}{k_3^{(m)}}$$

$$E_{x_3 d} = -E_{x_1 d}\frac{k}{k_3^{(d)}} \qquad (1.4)$$

In order to find the relation between H_{x2} and E_{x1} we can use the Maxwell's equation $\nabla \times \mathbf{E} = -\mu\dfrac{\partial \mathbf{H}}{\partial t}$ (Faraday's law of electromagnetic induction) and assuming $\mu = \mu_0$. The resulting equations are

$$H_{x_2 m} = \frac{\omega E_{x_1 m}\varepsilon_d\varepsilon_o}{k_m^{(m)}}$$

$$H_{x_2 d} = \frac{\omega E_{x_1 d}\varepsilon_m\varepsilon_o}{k_m^{(d)}} \qquad (1.5)$$

Finally we can apply the interface or boundary condition at $x_1 = 0$. At this interface the tangential components of $\mathbf{H}$ and $\mathbf{E}$ are continuous, thus $H_{x_2 m} = H_{x_2 d}$ and $E_{x_1 m} = H_{x_1 d}$, along with $A = B$. By using these boundary conditions the following simple relationship between relative permittivity and the normal components of the wave vector in both media can be obtained.

6

$$\frac{\varepsilon_m(\omega)}{k_3^{(m)}} = \frac{\varepsilon_d}{k_3^{(d)}} \tag{1.6}$$

If we have a truly trapped surface plasmon wave with exponential decay into both media then we need $ik_3^{(m)} > 0$ and $ik_3^{(d)} < 0$. Also we know that

$$\left(k_3^m\right)^2 + (k)^2 = \varepsilon_m(\omega)(k_o)^2$$
$$\left(k_3^d\right)^2 + (k)^2 = \varepsilon_d(k_o)^2 \tag{1.7}$$

where $k_o = \omega/c$. Hence by using the above equation (1.7) with the constraints of exponential decay for s surface wave we obtain the following relations

$$k_3^m = -i\sqrt{\left((k)^2 - \varepsilon_m(\omega)(k_o)^2\right)}$$
$$k_3^d = i\sqrt{\left((k)^2 - \varepsilon_d(k_o)^2\right)} \tag{1.8}$$

The above equation (1.8) requires $(k)^2 > \varepsilon_d(k_o)^2$ and $(k)^2 > \varepsilon_m(\omega)(k_o)^2$. Thus both the normal wave vector components are imaginary and are of opposite sign. This along with the equation (1.6) gives that in order to have SPP wave the two adjacent media need to have dielectric constant of opposite sign. This would then lead to a conclusion that the 'k' in the dielectric medium is greater than the maximum photon wave vector available in the dielectric, $\sqrt{\varepsilon_d}\,k_o$. In the metal medium the condition on 'k' is satisfied automatically with the ε_2 negative. By substituting equation (1.8) into equation (1.6) we obtain the following equation.

$$k_{SP} = k = k_o\sqrt{\frac{\varepsilon_m(\omega)\varepsilon_d}{\varepsilon_m(\omega) + \varepsilon_d}} \tag{1.9}$$

where 'k_{SP}' is the parallel wave vector of the SPP. For the SPP wave to be propagating on the surface then 'k' needs to be real. This can be achieved for $\varepsilon_m < 0$ when $|\varepsilon_m| > \varepsilon_d$. Thus

7

by solving the Maxwell's equations and boundary conditions it has been shown that a trapped surface wave like SPP can be obtained with real 'k', provided $|\varepsilon_m| > \varepsilon_d$ and $\varepsilon_m < 0$. In order to illustrate the result obtained in Eq. (1.9), let us use the free-electron model Eq. (1.1) for dielectric function of metal. The corresponding dispersion curve is shown in Fig. 1.2.
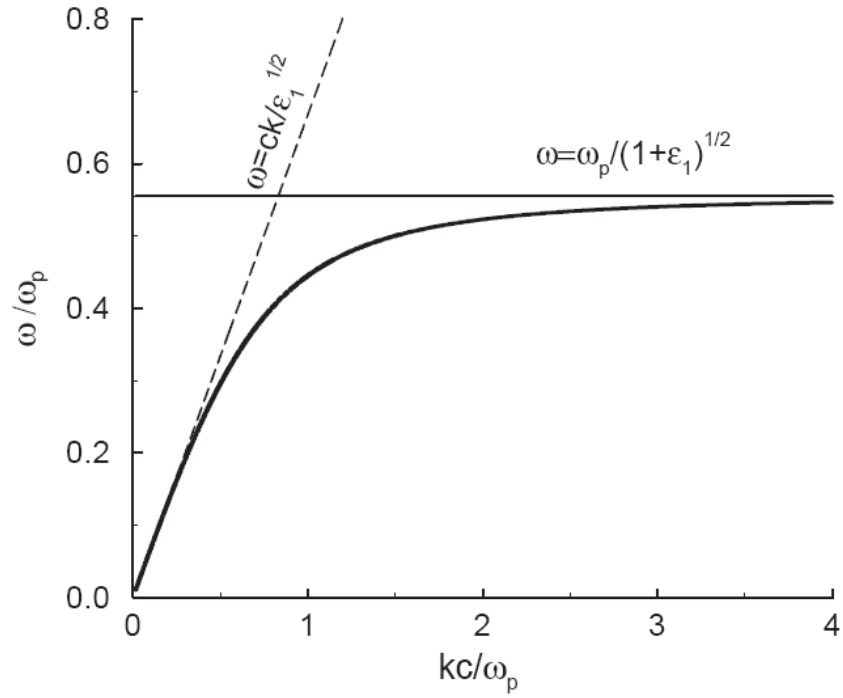
Figure 1.2: Dispersion curve (dark continuous line) of a surface plasmon polariton at a planar smooth dielectric-metal interface. Also plotted is the dispersion curve (dashed line) of the light in the dielectric medium and the corresponding surface plasmon frequency [7].

The dispersion curve of the SPP is towards the right of the dispersion curve of light in the dielectric medium, $\omega = \dfrac{ck_o}{\sqrt{\varepsilon_d}}$, the so-called dielectric light line. This is due to the requirement of the normal wave vector 'k_3^d' be imaginary and positive for the SPP electromagnetic field decay exponentially into the dielectric medium. Consequently, the SPPs cannot radiate light into the dielectric medium and also they cannot be excited with conventional illumination schemes from the adjacent dielectric medium. The electric field of SPP has a component that is parallel to the direction of propagation and another component that is perpendicular to the surface. The ratio of transverse and longitudinal components of the electric field in the dielectric medium is given by the following equation

$$\frac{E_{3d}}{E_{1d}} = i\frac{k}{k_3^d} = i\sqrt{\left(\frac{-\varepsilon_m(\omega)}{\varepsilon_1}\right)} = i\sqrt{\left(\frac{\omega_p^2 - \omega^2}{\varepsilon_1 \omega^2}\right)} \tag{1.10}$$

where the last expression is obtained by using the free electron model expression (1.1) assumed for metal, $\varepsilon_m(\omega)$. The transverse component is dominant at low frequencies and with small wave vectors for which the dispersion curve is close to the dielectric light line. For very large wave vectors the transverse and longitudinal components are comparable and they are equal at the frequency given by $\dfrac{\omega_p}{\sqrt{\varepsilon_1 + 1}}$ [7].

Let's now consider *s*-polarized or transverse electric (TE) wave for the structure shown in Fig. 1.1. In TE polarization the electric vector is perpendicular to the plane of

incidence. The solutions of the Maxwell's equations are wavelike in the x_1-direction and are localized to the interface as shown below

$$E_d(\mathbf{x},t) = (0, A, 0)\exp\left[ikx_1 + ik_3^{(d)}x_3 - i\omega t\right]$$
$$H_d(\mathbf{x},t) = A\frac{c}{i\omega}\left(-ik_3^{(d)}, 0, ik\right)\exp\left[ikx_1 + ik_3^{(d)}x_3 - i\omega t\right]$$

(1.11)

in the region $x_3 > 0$, and

$$E_m(\mathbf{x},t) = (0, B, 0)\exp\left[ikx_1 + ik_3^{(m)}x_3 - i\omega t\right]$$
$$H_m(\mathbf{x},t) = B\frac{c}{i\omega}\left(-ik_3^{(m)}, 0, ik\right)\exp\left[ikx_1 + ik_3^{(m)}x_3 - i\omega t\right]$$

(1.12)

in the region $x_3 < 0$. The boundary conditions of continuity of the tangential components of the electric and magnetic fields across the interface ($x_3 = 0$) yields the following equations

$$A = B, \ A\frac{c}{i\omega}k_3^{(d)} = B\frac{c}{i\omega}k_3^{(m)}$$

(1.13)

and the above equation (1.13) can be simplified as follows

$$\left(k_3^{(d)} - k_3^{(m)}\right)A = 0$$

(1.14)

It can observed from the equation (1.13) that when the imaginary parts of the '$k_3^{(d)}$' and '$k_3^{(m)}$' have to be of opposite sign for the electromagnetic wave to be localized to the dielectric-metal interface ($x_3 = 0$), the only solution is possible when $A = B = 0$. Thus TE or *s*-polarized SPP cannot exist in the structure depicted in Fig. 1.1.

1.2.2 Optical excitation of surface plasmons

In order to excite SPPs by the *p*-polarized light incident on a planar metal surface from the adjacent dielectric medium then there are two conditions that have to be

satisfied. The first one is that the frequency of the incident light must be equal to the frequency of the SPP. This condition is easily satisfied due to the energy balance. The next condition is that the component of the wave vector of the incident light parallel to the surface or interface in the dielectric medium ($\sqrt{\varepsilon_d}\,\dfrac{\omega}{c}\sin(\theta)$, where '$\theta$' is the angle of incidence) must equal the SPP wave vector (equation (1.9)). However from the dispersion curve (Fig. 1.2) it can be concluded that the SPP wave vector or wavenumber is larger than the magnitude of the wave vector of the light in the adjacent dielectric medium. Therefore special experimental arrangements have to be designed to provide the necessary wave vector matching or conservation. Hence the photon and SPP wave vectors can be matched either by using the either the photon tunneling that can be achieved in the total internal reflection geometry (Kretschmann and Otto configurations) or though the diffraction effects of the gratings (Fig. 1.3).

In Kretschmann geometry (Fig. 1.3a), a thin metal film can be illuminated through a dielectric prism at an angle of incidence (θ) greater than the critical angle for total internal reflection [7]. The wave vector of the light is increased in the optically denser medium. At a particular 'θ' the in-plane wave vector of the photon would coincide with the SPP wave vector at the air-metal interface. The resonant light tunneling through the metal film occurs and then light is coupled to the SPPs. The wave vector conservation is achieved by the following relation.

$$k_{SP} = \frac{\omega}{c}\sqrt{\varepsilon_{prism}}\,\sin(\theta) \tag{1.15}$$

11

At these resonant conditions, a sharp minimum can be observed in the reflectivity from the prism-metal interface as the light couples to SPPs at 100% efficiency [7]. When the metal film thickness increases the efficiency of the SPP excitation decreases since the tunneling of photons decreases with the thickness increase. The SPP cannot be excited on the interface of the prism and metal, since the wave vector of the SPP at this interface is greater than the photon wave vector in the prism at all angles of incidence. Therefore in order to excite SPPs on the internal metal interface an additional dielectric layer with a refractive index smaller than the prism should be deposited between the prism and the metal film (Fig. 1.3b). In such two-layer geometries the photon tunneling through the dielectric layer can provide the resonant excitation of the SPPs on the inner surface of the metal film. Hence the SPPs can be excited on both the inner and the outer surfaces of the metal film at different angles of incidence [7].
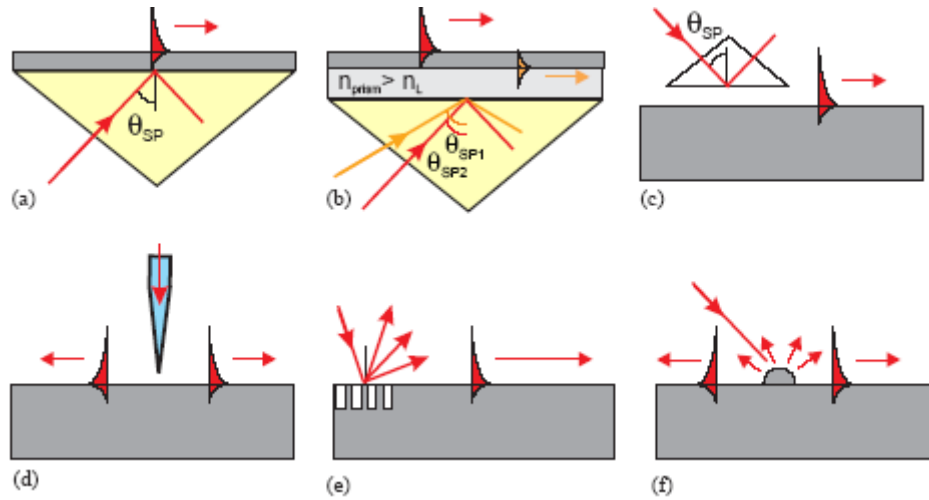
Figure 1.3: Surface plasmon polariton excitation configurations: (a) Kretschmann geometry, (b) two-layer Kretschmann geometry, (c) Otto geometry, (d) excitation of with scanning near-field optical microscopy, (e) diffraction on a grating, and (f) diffraction on surface features [7].

For when the metal film thickness increases then the Kretschmann geometry cannot be used. Instead Otto configuration (Fig. 1.3c) can be used where a prism with total internal reflection is placed close to the metal surface. This time the photon tunneling occurs through the thin air gap between the prism and the surface [7]. Another way to provide the wave vector conservations for SPP excitation is by using the diffraction of the gratings. If a diffraction grating is created on part of an otherwise smooth metal film then the some of wave vector components of the diffracted light can coincide with the SPP wave vector to couple and resonantly excite SPs. Wave vector conservation between the diffraction on a periodic structure to the SPPs is given by the following relation [10].

$$k_{SP} = \frac{\omega}{c} n_s \sin(\theta)\mathbf{u}_{12}\delta_p \pm p\frac{2\pi}{D}\mathbf{u}_1 \pm q\frac{2\pi}{D}\mathbf{u}_2 \qquad (1.16)$$

where $\delta_p = 1$ for the a p-polarized (with respect to the surface plane) incident light and 0 for a the s-polarized light, $\mathbf{u}_{12}$ is the unit vector in the in-plane component of the wave vector of the incident light, n_s is the refractive index of the medium through which the metal film is illuminated, $\mathbf{u}_1$ and $\mathbf{u}_2$ are the unit lattice vectors of the periodic structure, D is the period of the structure which is assumed to be same in both the x_1 and x_2 directions, and p and q are the integer numbers corresponding to the diffraction order of the light that couple to the excited SPPs. Depending on the metal film thickness and grating profile depth SPPs can be excited on both air-metal and substrate-metal surfaces [7].

There is one more approach to resonantly excite the SPPs and it is possible through diffraction of light from surface features (Fig. 1.3f). The SPPs are excited on both sides of the interface and propagate in directions to both the left and right edge of

the sample. The use of the SNOM to study the SPP has introduced a new technique that provides the possibility of exciting SPP locally at a given place on a surface [11] (Fig. 1.3d). Circular SPP waves can be launched using illumination through a SNOM fiber tip. This technique can be treated as either a diffraction or tunneling mechanism for exciting SPPs. The former case is due to the near-field coupling of the diffracted light from the subwavelength aperture of the fiber tip into the SPPs. The latter case is due to the photon tunneling that takes place from the fiber tip to the metal surface and also only evanescent field components are generated at the aperture. This SNOM fiber tip for SPP excitation is similar to the Otto geometry except for the local excitation of SPPs is possible with sub-wavelength precision. The SPPs have longitudinal nature and so for all of the configurations described above the exciting light should have an electric field component perpendicular to the metal surface or parallel to the propagation direction of the excited SPPs [7].

1.3 OPTICAL NEAR-FIELD ENHANCEMENT

This optical near-field enhancement by micro-spheres can be explained by Mie scattering and Rayleigh scattering. When the diameter of the sphere is equal to or greater than the laser wavelength, light is scattered elastically and the field is enhanced several times at the exit side of the spheres. Mie theory calculations show that this enhancement is due to both near-field and scattering effects. Such optical enhancement can lead to local melting or even vaporization of the substrate materials for nanoscale surface patterning. On the other hand Rayleigh scattering would take place when the diameter of the sphere is less than the wavelength of the light. In this case, the sphere is treated as a

14

dipole radiator and the electric field enhancement is at its sides along the direction of polarization of the incident light and there is hardly any focusing [12].

It has been reported that the optical near field intensity enhancement changes dramatically with the size of the sphere and also with the distance between the sphere and the substrate [13-15]. Figure 1.4a shows the optical near-field intensity distribution obtained by [15] on the silicon substrate for wavelength λ = 532 nm, and corresponding to a silica microsphere (n = 1.37) 1.76 μm in diameter. The resulting peak intensity obtained is 14.65 times the incident intensity. Also it is shown that the obtained intensity enhancement is centered on a circular area of radius smaller than the sphere. When the microsphere is elevated to a distance from the silicon surface then the near-field intensity peak decreases dramatically and the focusing area becomes much bigger (as shown in Fig. 1.4b).
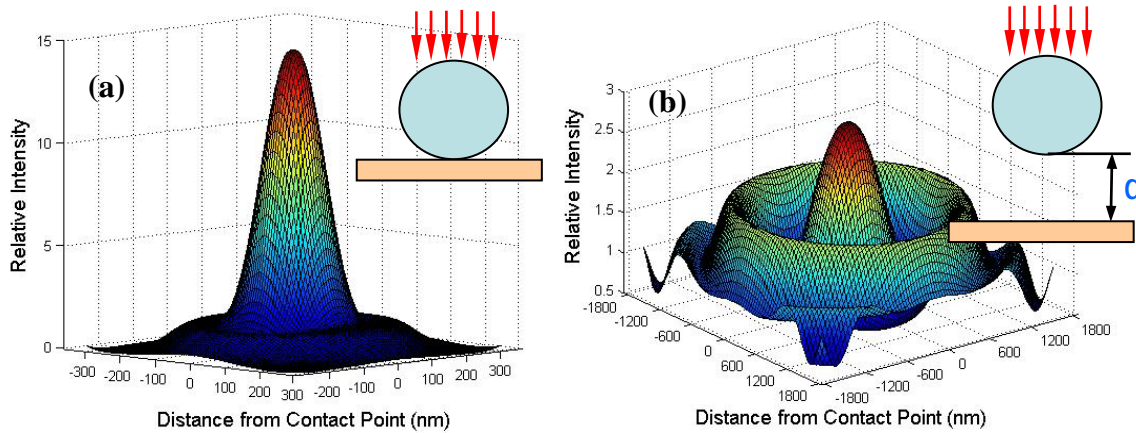
Figure 1.4: Optical near-field intensity enhancement on silicon surface due to laser-microsphere interaction (λ = 532 nm, silica microsphere 1.76 μm in diameter) when the microsphere is (a) on the substrate, and (b) elevated 1.76 μm above the surface [15].

The optical near-field enhancement on the surface is dependent on the wavelength, diameter of the microsphere, and distance from the sphere. Fig. 1.5 shows the enhancement variation with respect to the distance from the sphere for various wavelengths and two different sphere diameters. From Fig. 1.5, it can be observed that the enhancement is highest for a bigger sphere diameter, lower wavelength and when the sphere is near the surface. As the wavelength increases the enhancement decreases. Also, with the increase in the distance from the sphere the enhancement decreases and the rate of decrease is large for the lower wavelengths. When the wavelength is high the enhancement is low and becomes insensitive to the variation in the distance from the sphere. The reduction in sphere diameter would also decrease the enhancement.
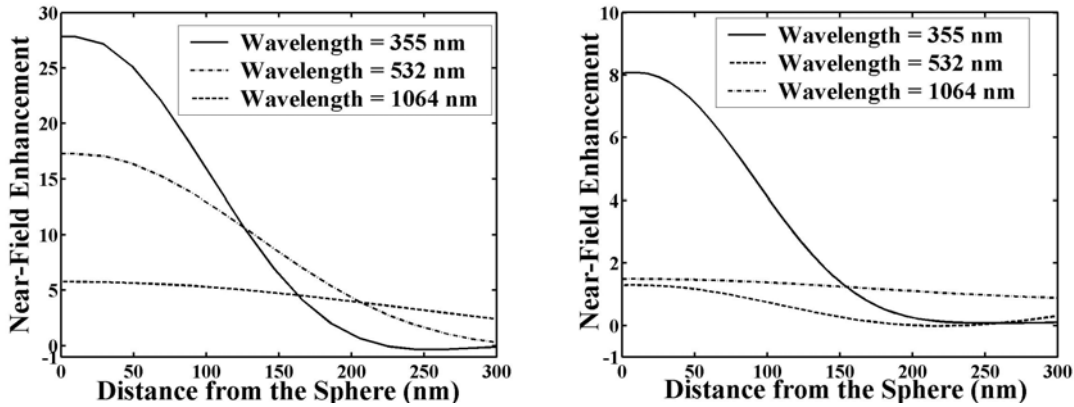
Figure 1.5: Optical near-field intensity enhancement on silicon surface due to laser-microsphere interaction for different wavelength with varying distance from the sphere and (a) 1.76 μm in diameter, (b) 640 nm in diameter.

1.4 Dissertation overview

The goals of this dissertation are to pattern high bandgap materials in a sub-micron scale using optical near-field effects and to design and analyze plasmonic optical devices. To understand the plasmonic nature of the optical devices that were designed, numerical computation was performed using the Finite Element Method (FEM).

Chapter 2 is about extraordinary transmission (EOT) through subwavelength holes and apertures in metallic films. It will be discussed on how the EOT spectral locations can be tuned by introducing an extra degree of freedom in the geometrical parameter and also by using an external magnetic field. In chapter 3, a very unique design of sub-micron scale thermal emitter is proposed and analyzed. This new design has the emission properties similar to a laser. Chapter 4 has another new design of photonic crystal with plasmonic or metallic structures along with an extra degree of freedom to tune the dispersion properties. This new tunable plasmonic crystal can be used for sub-wavelength imaging. In chapter 5, experimental results of the direct parallel patterning of Silicon carbide (SiC) and borosilicate glass will be discussed. Finally in chapter 6, a brief summary of the current work along with the future recommendations is discussed.

Reference

[1]. G. Binnig, K. H. Frank, H. Fuchs, N. Garcia, B. Reihl, H. Rohrer, F. Salvan, A. R. Williams, "Tunneling Spectroscopy and Inverse Photoemission - Image and Field States", *Physical Review Letters*, **55**, 991-994 (1985).
[2]. G. Binnig, H. Rohrer, C. Gerber, E. Weibel, "7x7 Reconstruction on Si(111) Resolved in Real Space", *Physical Review Letters*, **50**, 120-123 (1983).
[3]. G. Binnig, H. Rohrer, C. Gerber, E. Weibel, "Tunneling through a Controllable Vacuum Gap", *Applied Physics Letters*, **40**, 178-180 (1982).
[4]. C. Girard, C. Joachim, S. Gauthier, "The physics of the near-field", *Reports on Progress in Physics*, **63**, 893-938 (2000).

[5]. E. Betzig, J. K. Trautman, "Near-Field Optics - Microscopy, Spectroscopy, and Surface Modification Beyond the Diffraction Limit", *Science*, **257**, 189-195 (1992).

[6]. J. D. Kraus, *Antennas* (McGraw-Hill, New York,, ed. 1st, 1950).

[7]. A. V. Zayats, I. I. Smolyaninov, A. A. Maradudin, "Nano-optics of surface plasmon polaritons", *Physics Reports-Review Section of Physics Letters*, **408**, 131-314 (2005).

[8]. G. Boisdé, A. Harmer, *Chemical and biochemical sensing with optical fibers and waveguides*, The Artech House optoelectronics library (Artech House, Boston, 1996).

[9]. A. V. Zayats, I. I. Smolyaninov, "Near-field photonics: surface plasmon polaritons and localized surface plasmons", *Journal of Optics a-Pure and Applied Optics*, **5**, S16-S50 (2003).

[10]. H. Raether, *Surface plasmons on smooth and rough surfaces and on gratings*, Springer tracts in modern physics 111 (Springer-Verlag, Berlin ; New York, 1988).

[11]. B. Hecht, H. Bielefeldt, L. Novotny, Y. Inouye, D. W. Pohl, "Local excitation, scattering, and interference of surface plasmons", *Physical Review Letters*, **77**, 1889-1892 (1996).

[12]. Y. Lu, S. C. Chen, "Nanopatterning of a silicon surface by near-field enhanced laser irradiation", *Nanotechnology*, **14**, 505-508 (2003).

[13]. H. J. Munzer, M. Mosbacher, M. Bertsch, J. Zimmermann, P. Leiderer, J. Boneberg, "Local held enhancement effects for nanostructuring of surfaces", *Journal of Microscopy-Oxford*, **202**, 129-135 (2001).

[14]. O. Watanabe, T. Ikawa, M. Hasegawa, M. Tsuchimori, Y. Kawata, "Nanofabrication induced by near-field exposure from a nanosecond laser pulse", *Applied Physics Letters*, **79**, 1366-1368 (2001).

[15]. A. J. Heltzel, S. Theppakuttai, J. R. Howell, S. C. Chen, "Analytical and experimental investigation of laser-microsphere interaction for nanoscale surface modification", *Journal of Heat Transfer-Transactions of the Asme*, **127**, 1231-1235 (2005).

Chapter 2: Tuning the extraordinary optical transmission through metallic film having subwavelength apertures

2.1 INTRODUCTION

In late 1980's the concept of photonic crystals emerged, which initiated new studies of gratings, as examples of one-dimensional (1D) periodic media [1, 2]. Since then some theoretical studies have been done on the transmission gratings, but they did not receive much attention because it was thought that the transmission through the subwavelength apertures is very low according to the standard aperture theory by Bethe [3], which states that the transmission through a subwavelength circular hole ($r \ll \lambda$) in an infinitely thin perfectly conducting metal sheet would scale uniformly with the ratio of r to λ to the power of four. But, an extraordinary transmission (EOT) of several orders of magnitude more than Bethe's prediction has been reported through an array of subwavelength holes milled in an opaque metal screen [4]. The underestimation of transmission by Bethe's theory is because it is too idealized to consider the surface modes that might be involved and also propagating of evanescent modes that could be excited inside the holes [5]. Subsequently, enhanced transmission through hole arrays in metal films has been studied in great detail both theoretically and experimentally. This has sparked renewed interest in studying the transmission gratings (or slits), which are 1D version of the hole structures studied by [4], to explain the underlying physics for enhanced transmission. However, the transmission properties between slit and hole arrays have a fundamental difference. In a slit waveguide there is always a propagating mode inside the channel, whereas in a hole waveguide all modes are evanescent when hole

19

diameters are smaller than half the wavelength and there is a cutoff frequency for transmission [6]. Hence the slit and hole array structures have very different propagation mechanisms. But, it is believed in general that the EOT phenomenon is mainly due to the surface plasmons polariton (SPP) modes trapped at the interface of metal and dielectric. The SPPs are actually quanta of collective plasma oscillations localized at interface of a metal and dielectric [7]. However not all agree on the same SPP mechanism for the enhanced transmission phenomena [8, 9]. Nevertheless, according to several other theoretical and experimental studies the enhanced transmission process through subwavelength metallic hole array (MHA) can be divided into three steps: the coupling of light to SPPs on the incident surface, transmission through the holes to the second surface and then re-emission from the second surface [5].

The dielectric response, $\varepsilon(\omega)$, of a metal is governed mainly by its free electron plasma and for frequencies smaller than the plasma frequency the real part of '$\varepsilon(\omega)$' is negative, which makes it behave like a photonic insulator at those frequencies. Negative 'ε' has another consequence: the metal-dielectric interface can support surface electromagnetic modes called SPPs as discussed in chapter 1. The dispersion relation of these modes for a flat interface does not cross the light cone and so SPP cannot be excited by a direct incident plane wave. However, if the metal-dielectric interface is modulated periodically, the SPP bands fold allowing the external radiation to excite the SPP modes [6]. Therefore, when the frequency (ω) and the in-plane wave vector ($k_{\parallel}$) of the light scattered by the grating vector match the surface mode (or SPP mode) of the structure the transmittance and reflectance are modified [10]. Hence the physics behind the enhanced transmission in metallic subwavelength apertures was initially considered as the coupling

of the incident light via diffraction to the SPP modes of the metallic structure [4, 11]. This type of explanation was expected since surface plasmons are responsible for a type of grating anomalies, as was previously established [12]. Due to the range of energies and incident angles considered in the present study, the energetic positions of the SPP modes coincide with the *Wood-Rayleigh anomaly* [13]. This anomaly in the transmission spectra is due to the vanishing or emerging of a diffracted order above or below the grating in vacuum. There is one more kind of anomaly that appears in Transverse Magnetic (TM-) polarized reflection or transmission spectra of metallic gratings, which is called the *resonance anomaly* [13]. For this anomaly the SPP resonance modes on lower and upper surfaces of the gratings are excited when one of the diffracted waves is coupled to the SPP modes. However, there are other kinds of electromagnetic resonances, like the cavity modes or waveguide resonances, which may also play an important role in enhanced transmission [14]. It was reported that in order to have high transmission through metallic gratings the waveguide mode resonance in the channel is the only effective way, even at the SPP resonance mode excitation wavelength [15].

For the transmission process through subwavelength holes or gratings, diffraction plays a central role. When a plane wave is incident on grating array, the diffraction leads to evanescent wave. After the transmitted evanescent wave reaches the far end of the array it gets diffracted again producing a propagating transmitted wave. Therefore the transmission enhancement occurs when the diffraction aids in coupling the incident light and the SPP modes of the silver metal structure [10]. It was also reported that for lamellar transmission metallic gratings there are two transmission resonances: coupled SPP modes on both the horizontal surfaces of the metallic grating for $\lambda \sim d$, and cavity or waveguide

modes located inside the slits for $\lambda \gg d$ [16]. Diffraction is independent of the array material, but the arrays made of a metal such as silver (Ag) have shown higher transmittance when compared to metals like nickel (Ni) [17].

The EOT phenomenon through subwavelength MHAs milled in opaque metal screen [4] has generated considerable interest and promoted subwavelength apertures as a core element of new optical devices. This is because of the simplicity with which the spectral properties can be tuned and scaled. EOT in THz region has been observed recently in both metallic [18-21] and semiconductor hole arrays [22-24]. In the millimeter wave and terahertz (THz) region the two-dimensional (2D) MHAs act as band-pass filters also known as frequency-selective surfaces (FSSs). However, in those frequency regions the metal surfaces act as perfect conductors on which the SPPs excitation cannot be expected. But, it has been proven both theoretically [25] and experimentally [26] that the resonantly excited SPP-like mode plays an important role in the high transmission in the THz region.

The manipulation of light at the subwavelength scale have several geometric variables, such as hole shape, periodicity, interface media, film thickness, aperture size and so on. In the previous work, different hole shapes like elliptical [27], rectangular [28], C-shaped [29, 30], X-shaped [31], coaxial [32] and so on have been studied. It was found that a hole shape change from circular to rectangular increases the normalized transmission by an order of magnitude with a large red-shift in the spectra [28]. But, it was noted that the influence of the hole shape is dramatically different in terahertz (THz) region from that in the optical region [20, 21]. Also, hole lattices with different symmetry are studied and it is found that the spectrum shape and transmission efficiency depend

22

strongly on the rotational symmetry [33]. In addition, it was observed that when the index of refraction filled in the metallic hole arrays increases then the peak transmission would have a red-shift [34, 35]. Similarly, when the surrounding dielectric constant is increased then a red-shift along with a reduction in the transmission amplitude is observed [24]. Furthermore, the thickness of the metal film strongly effects the coupling interaction of the SPPs on both incident and transmitted surfaces. It was found that when the hole depth is large then the SPPs on the two surfaces are uncoupled and the transmission increases exponentially with the decreasing depth [36]. It is observed in the THz region the EOT can be achieved at an array thickness of only one third of the skin depth [37].

The SPPs are attracting much attention due to their possible applications for light control at nanoscale. For example, the plasmon resonance condition of a nanoshell is sensitive to the relative size of the core and shell layers [38]. Similarly, gyrotropic media with magento-optical Faraday and Kerr effects have derived a great interest for applications in submicron scale to control the light [39, 40]. In recent times both the magnetized films with perforated holes and magnetized pillars included in a dielectric have been studied for their plasmonic aspects [41-43]. Following the report of extraordinary transmission through subwavelength holes [4], a study was conducted on the idea of how the transmission peaks would depend in the presence of a static, in-plane magnetic field [42]. It was concluded in the study that the transmission peaks depend not only on the plasma frequency but also on the magnitude and direction of an applied static magnetic field **H**. However the study has treated the cylindrical holes as dielectric inclusions in a conducting host that occupies the entire volume in between the infinitely conducting plates of a large capacitor. Transmission through ferromagnetic Co films

perforated with holes was determined experimentally and it was concluded that the magneto-optic (MO) Kerr effect is suppressed in the wavelength range where there is an enhanced transmission. Lately, a study [44] has been reported with simultaneous enhancement of both transmittance and MO Faraday and Kerr effect in a bilayer system of a metallic film perforated with subwavelength hole arrays and a uniform dielectric film magnetized perpendicular to its plane. Nevertheless none of the above studies have considered a finite metal film with the effect of different directions of the **H** on the transmission peaks.

2.2 COMPUTATIONAL SET-UP

2.2.1 General theory of Maxwell's equation

The Maxwell's equations in differential form with no sources, i.e., no current vector ($\vec{J} = 0$), no charge ($\rho_\upsilon = 0$) and by substituting the constitutive equations for an isotropic homogeneous medium are given below:

$$\nabla \times \vec{\text{E}} = -\mu \frac{\partial \vec{H}}{\partial t} \qquad (2.1)$$

$$\nabla \times \vec{\text{H}} = \varepsilon \frac{\partial \vec{\text{E}}}{\partial t} \qquad (2.2)$$

$$\nabla \cdot \vec{\text{E}} = 0 \qquad (2.3)$$

$$\nabla \cdot \vec{H} = 0 \qquad (2.4)$$

where $\vec{\text{E}}$ and $\vec{\text{H}}$ are the electric field and magnetic field intensity respectively. 'ε' and 'μ' are permittivity and permeability of the medium respectively. The electromagnetic

24

field distribution can be assumed to be a harmonic propagation wave and it is given as follows

$$\vec{E} = \vec{E}_o \, \boldsymbol{exp}\left[i\left(\vec{k} \cdot \vec{r} - \omega t\right)\right] \tag{2.5}$$

$$\vec{H} = \vec{H}_o \, \boldsymbol{exp}\left[i\left(\vec{k} \cdot \vec{r} - \omega t\right)\right] \tag{2.6}$$

where, '$\vec{k}$' is the wavevector and 'ω' is the frequency. Hence by substituting the eq. (2.5) & (2.6) into eq. (2.2) & (2.1) respectively would give the following equations.

$$\vec{\nabla} \times \vec{E} = i\omega\mu\vec{H} \tag{2.7}$$

$$\vec{\nabla} \times \vec{H} = -i\omega\varepsilon\vec{E} \tag{2.8}$$

Substituting $\vec{E}$ from eq. (2.8) into eq. (2.7) gives the following equation

$$\vec{\nabla} \times \left(\frac{1}{-i\omega\varepsilon} \vec{\nabla} \times \vec{H}\right) = i\omega\mu\vec{H} \tag{2.9}$$

The above eq. (2.9) after few further simplifications and with a TM or *p*-polarization for lamellar gratings (magnetic field is along the direction of gratings) would be the following equation with $\mu = \mu_o$ and $\varepsilon = \varepsilon_r\varepsilon_o$, where μ_o and ε_o are the permeability and permittivity of vacuum or air. Also $c = \dfrac{1}{\sqrt{\varepsilon_o\mu_0}}$ and $k = \dfrac{\omega}{c}$, where c is the speed of light in air.

$$\vec{\nabla} \cdot \left(\frac{1}{\varepsilon_r} \vec{\nabla} H_z\right) + k^2 H_z = 0 \tag{2.10}$$

The above equation is a partial differential equation (PDE) called Helmholtz equation with the variable H_z. The PDE can be solved using finite element method (FEM). The FEM numerical simulation is carried out by using commercially available

software FEMLAB 3.1i. The following sections give the details of the computational study that has been done.

2.2.2 Two-dimensional computation domain for gratings and governing equations

In Fig. 2.1 we show a schematic view of the three different structures in vacuum that were studied with the definition of different parameters: the period of grating (d), the aperture width (a), the grating thickness (t), and the gap at the throat (g). Although the transmission resonances of the gratings depend on their period, aperture width and thickness, they are fixed in this study to explore the effect of different gap sizes at the throat. The gap sizes were varied from 0.5 μm to 5 nm. It is plausible to use Maxwell's equation when the absolute lower limit of the length of macroscopic domain is 10 nm [45]. In addition, the optical absorption spectrum of 30 nm spherical metallic particles calculated by solving Maxwell's equations agreed well with the experimental results [46]. Therefore, it is assumed that the results obtained in the present study for gap of 5 nm will be rational. Nevertheless, it should be pointed out that the effects discussed in this study do apply for any other range of grating parameters provided that the aperture width is very small in comparison to the grating period. Also the frequency of incident light has to be well below the plasma frequency of the metal [16]. The dielectric function of gold described in this study is from the tables reported in [47]. The transmission for metallic lamellar gratings with Transverse Electric (TE) polarization suffers a cut-off wavelength [48]. Hence, we have analyzed the metallic gratings with only TM polarization (magnetic field vector parallel to the gratings) in order to study whether the enhanced transmission could be achieved for any desired wavelength with the CDC structure. Therefore the

resulting governing equation for the time harmonic electromagnetic fields, with the dependent variable as magnetic field in the z-direction (H_z) is given by eq. (2.10). Commercially available finite element software (FEMLAB 3.1i) was used for solving the governing equation. A 2D computational domain surrounded by periodic boundary conditions and perfectly matching layer (PML) [49] was used (Fig. 2.2). The transmittance of the grating was calculated from the obtained electromagnetic field distributions. Since the proposed study has a structure that is periodic in 1D and has the length of the grating larger than the period of the grating, then the resulting computational domain would be a 2D domain.

In the 2D computational domain the plane wave is generated from a small subdomain as shown in Fig. 2.2 and the governing equation for this source subdomain is given as follows.

$$\vec{\nabla} \cdot \left(\frac{1}{\varepsilon_r} \vec{\nabla} H_z \right) + k^2 H_z = f \tag{2.11}$$

where f is scalar value and is taken as ' $e^{(ik\sin(\theta)x)}$ ' in order to generate a plane wave with an angle of incidence 'θ'. The governing equation for the remaining subdomains (air, metal and PML) is same as eq. (2.10), except with a change in the dielectric constant that depends on the respective medium.
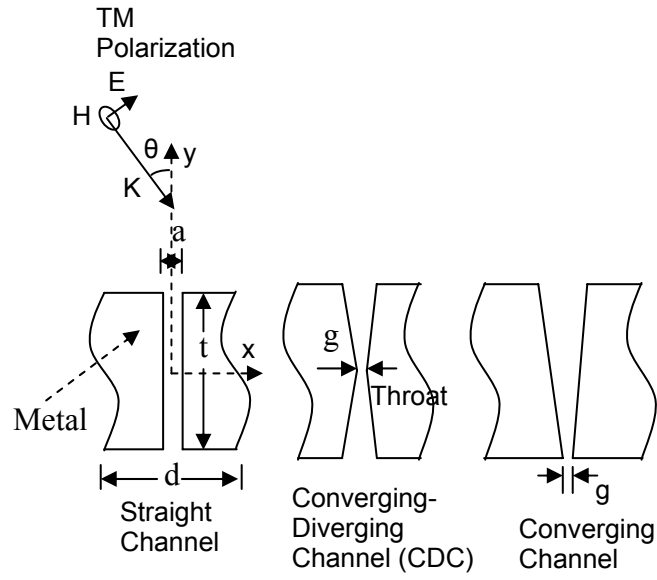
Figure 2.1: Schematic view of the lamellar transmission metallic gratings in vacuum with grating parameters as period (d) = 3.5 μm; aperture (a) = 0.5 μm; thickness (t) = 3.0 μm.
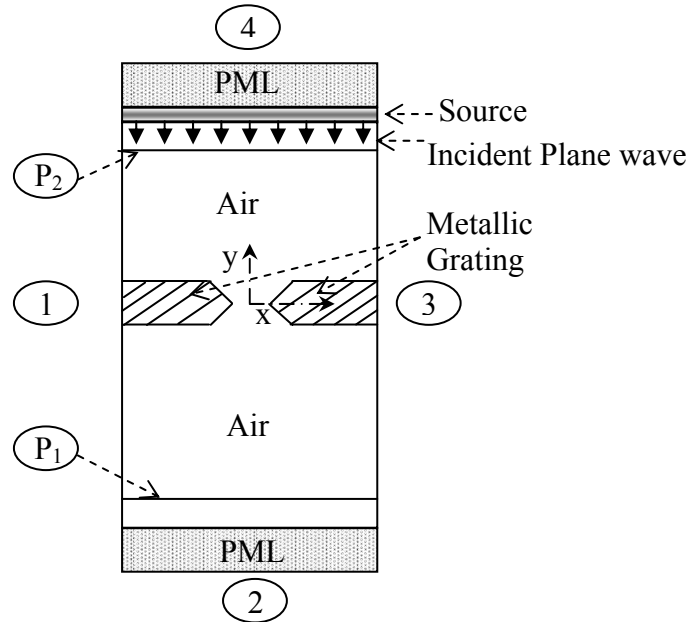
Figure 2.2: Outline of the 2D computational domain for the numerical study.

2.2.3 Boundary conditions, Interface conditions and absorbing boundary layer

The boundary conditions that will be used for the computational study is either a phase-shifted boundary condition or a perfect electric conductor. The phase-shifted boundary condition is used between boundaries ① & ③ (Fig. 2.2) and is given as follows.

$$\mathrm{H}_{z,3} = \mathrm{H}_{z,1}\, exp\big[ik\, sin(\theta)d\big] \tag{2.12}$$

The boundary condition for the perfect electric conductor is taken on boundaries ② and ④ (Fig. 2.2). It is given in mathematical form as follows.

$$\mathrm{E}_x = 0 \quad \text{or} \quad \vec{n}\cdot\left(\frac{1}{\varepsilon_r}\vec{\nabla}\mathrm{H}_z\right) = 0 \tag{2.13}$$

The interface condition between metal and air is taken as the tangential component of electric field to be continuous and is

$$\mathrm{E}_{t,air} = \mathrm{E}_{t,metal} \quad \text{or} \quad \left(\vec{n}\cdot\left(\frac{1}{\varepsilon_r}\vec{\nabla}\mathrm{H}_z\right)\right)_{t,air} = \left(\vec{n}\cdot\left(\frac{1}{\varepsilon_r}\vec{\nabla}\mathrm{H}_z\right)\right)_{t,metal} \tag{2.14}$$

The outgoing waves are absorbed by using a perfectly matched layer (PML) as suggested in [49]. The dielectric constant of the PML varies anisotropically as

$$\varepsilon_{r,PML} = \begin{pmatrix} \dfrac{s_y s_z}{s_x} & 0 \\ 0 & \dfrac{s_x s_z}{s_y} \end{pmatrix} \tag{2.15}$$

where $\qquad s_\zeta(\zeta,\omega) = a_\zeta(\zeta) + i\dfrac{\sigma_\zeta(\zeta)}{\zeta\,\omega}\, x,y,z, \qquad a_\zeta(\zeta) = 1 \tag{2.16}$

2.2.4 Transmission calculations

The transmittance (τ) and reflectance (η) for the metallic grating is calculated as follows

$$\tau = \frac{\left(H_z \cdot H_z^*\right)_{P1,F}}{\left(H_z \cdot H_z^*\right)_{P1,I}} \tag{2.17}$$

where $\left(H_z \cdot H_z^*\right)_{P1,F}$ is the incident magnetic field intensity at plane P_1 as shown in the Fig. 2.2, when there is no metallic grating and replaced with air instead. Similarly, $\left(H_z \cdot H_z^*\right)_{P1,I}$ is the final transmitted magnetic field intensity through the metallic grating. Hence, the eq. (2.17) would give transmittance. The reflectance is calculated by the following equation.

$$\eta = \frac{\left(\left(H_z - \dfrac{H_z}{ik\cos(\theta)}\right) \cdot \left(H_z - \dfrac{H_z}{ik\cos(\theta)}\right)^*\right)_{P2,F}}{\left(H_z \cdot H_z^*\right)_{P1,I}} \tag{2.18}$$

where $\left(H_z - \dfrac{H_z}{ik\cos(\theta)}\right)_{p2,F}$ is the reflected magnetic field at plane P_2 as shown in the Fig. 2.2.

2.2.5 Verification and Validation

The computational results are verified by refining the mesh size and since the linear system solver in FEMLAB 3.1i is a direct UMFPACK there is no iteration. Fig. 2.3 shows the magnetic field intensity inside a slab of thickness '2a' for the TM polarization and for both non-absorbing (n = 1.5) and absorbing (n = 1.5 + 0.05i) medium. These results match well with those given by [50].
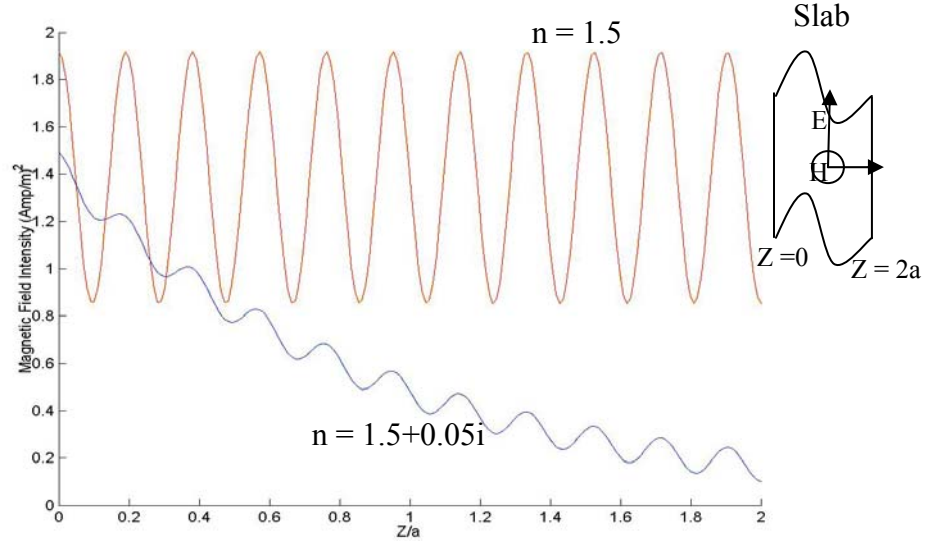
Figure 2.3: Magnetic field intensity inside the slab for different media.

2.2.6 Three-dimensional computation for holes

Figure 2.4 shows a schematic view of the square array of holes having CDC shape in a metallic film with the definition of different parameters: the period of hole array (d), the aperture size (A), the thickness of the metallic film (t), slope or angle of the CDC shape (θ) and the gap at the throat (g). Figure 2.4b shows cross-sectional view of the CDC channel with an angle (θ), which would relate 'A' and 'g' by a simple equation g = A − tan(θ)*t. The metallic film considered for the CDC hole array study is silver (Ag) and for most part of the study a fixed value for the period (d = 19.0 μm) and thickness (t = 2.0 μm) is used. Also, for the present study we considered the frequency to be around 100 THz or 20 μm wavelength. The silver dielectric constant is fit into the Drude model with

31

$\varepsilon = \varepsilon_\infty - \omega_p / (\omega^2 + i\gamma\omega)$ by taking $\varepsilon_\infty = -175.0$, $\omega_p = 1.1 \times 10^{16}$, and $\gamma = 10.51 \times 10^{13}$ in order to fit the empirical data given by [51] in the 100 THz frequency region. The electromagnetic fields were assumed to be time harmonic and the resulting governing equation for the steady-state distribution is given by eq. (2.10).

(a)   (b)
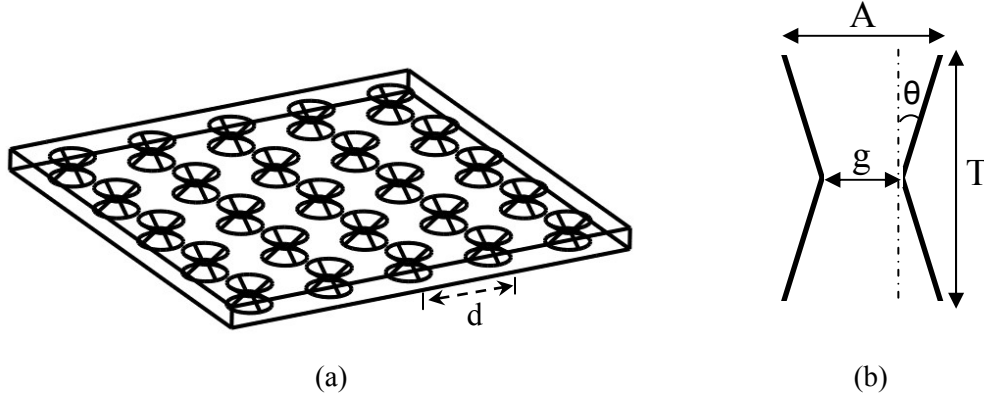
Figure 2.4: (a) Schematic view of silver metallic hole array having periodicity 'd' with converging-diverging channels (CDC), (b) cross-sectional view of the CDC shape with aperture (A), thickness (t), slope or angle (θ) of CDC shape and gap at the throat (g).

In the current study the transmission through a thin Ag film perforated with hole pair under different externally applied **H** is also considered. The holes are in rectangular shape and constitute a square lattice of period 'd' as shown in Fig. 2.5. The thickness of the Ag film is 'h' with the holes having width 'w' and length '*l*'. The spacing in between the holes is given by 's'. Throughout the current study, we choose d = 600 nm, h = 300 nm, s = 60 nm, and l = 400 nm. The 3D numerical modeling is performed with a finite element method (FEM) by using commercially available software (COMSOL 3.2a). The metallic material dielectric function (ε) is characterized by using a Drude model $\varepsilon = \varepsilon_\infty -$ $\omega_p / (\omega^2 + i\gamma\omega)$ for the frequency dependence. The silver dielectric constant is fit into the

Drude model by taking $\varepsilon_\infty = 7.9$, $\omega_p = 1.29 \times 10^{16}$, and $\gamma = 3.21 \times 10^{13}$ in order to fit the empirical data given by [51]. The optical properties of the Ag have a directional sensitivity to the externally applied **H** and result in strong anisotropy. The applied **H** enters through Hall-to-Ohmic resistivity ratio [42]. The local permittivity tensor (ε_m) of the Ag dielectric function can be obtained from [42, 52] and is given below for **B** $\parallel z$.

$$\varepsilon_m = \varepsilon_\infty - \frac{4\pi}{i\pi\rho_m}; \rho_m = \frac{4\pi}{\omega_p^2 \tau} \begin{bmatrix} 1 - i\omega\tau & -\omega_c\tau & 0 \\ -\omega_c\tau & 1 - i\omega\tau & 0 \\ 0 & 0 & 1 - i\omega\tau \end{bmatrix}; \tau = \frac{1}{\gamma} \tag{2.19}$$

The magnetic field enters the 'ε_m' tensor through the cyclotron frequency 'ω_c' (= $e\mathrm{B}/mc$) and this appears only in the antisymmetric off-diagonal elements of ρ_m.
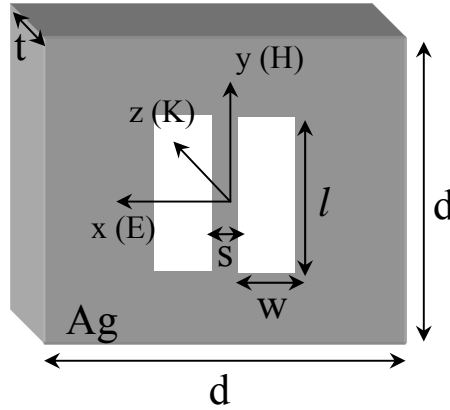
Figure 2.5: Schematic figure of light incident on a thin Ag film perforated with square array of rectangular hole pair having d = 600 nm; t = 300 nm; w = 60 nm; l = 400 nm; s = 60 nm.

33

The 3-dimensional (3D) numerical modeling is carried out by commercially available finite element software (COMSOL 3.2a). The computational domain considered is a single unit cell surrounded by either periodic boundary conditions as described in the above section or by perfectly matching layer (PML) as given in [49]. The light is incident normal to the film surface (**k** ∥ z) with transverse magnetic (TM) polarization and the transmittance is calculated from the obtained electromagnetic field distributions. In order to validate the 3D numerical model, transmission through a subwavelength hole array is calculated and is compared with the result obtained by [53]. The results obtained agreed with the theoretical results (Fig. 2.6).
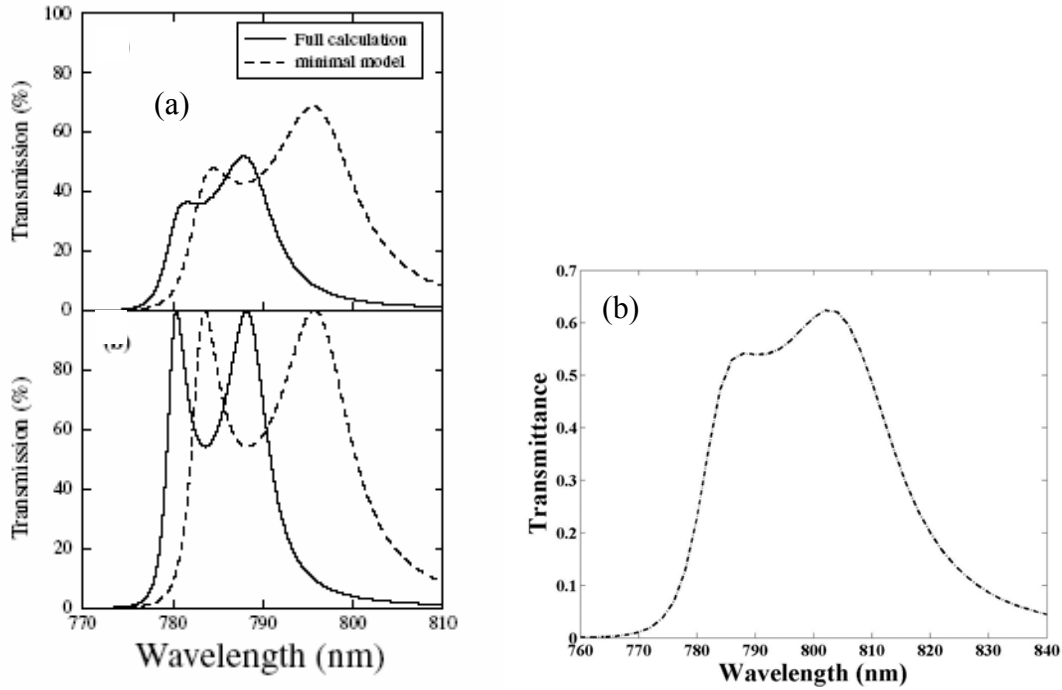
Figure 2.6: Comparison between the (a) theoretical results [53] and (b) numerical results.

34

2.3 TRANSMISSION THROUGH METALLIC SUBWAVELENGTH APERTURES HAVING CONVERGING DIVERGING CHANNEL (CDC)

The effect of hole channel shape on the transmission characteristics has not received considerable attention. The hole size along with the channel shape will have significant impact on the transmission efficiency because the holes are expected to mediate the SPP coupling between both surfaces. Hence in the present study the subwavelength hole having converging diverging channel (CDC) is studied specifically along with straight channel for transmission properties. This proposed CDC shape would still allow similar EOT effects but, would give an extra degree of freedom in the geometric variable to tune the transmission spectrum. Hence CDC shaped holes or gratings can be used for practical purposes where a high transmission is required. We also provide a physical insight into the mechanism for the shift of the resonant bands.

2.3.1 Metallic gratings with CDC

Figure 2.7a shows the zero-order transmittance for normal incident radiation as a function of wavelength for different channel configurations. The CDC with 5 nm gap at the throat has a remarkable transmission in a very narrow wavelength band. The two transmission peaks for the straight channel are identified as the SPP & waveguide coupled resonance ($\sim$ 3.9 µm) and waveguide resonance ($\sim$ 7.4 µm) [16]. Although the two transmission peaks seen for the converging channel are located at almost the same resonance wavelengths as for the straight channel, the transmittance is much lower, which is explained later. For CDC, the locations of transmittance peaks have changed in spectral positions and are approaching each other as the gap at throat decreases, as seen in

Fig. 2.7a. This would lead to a high transmission in a very narrow wavelength band and the transmittance is almost negligible everywhere else in the considered wavelength range. A closer look at Fig. 2.7a would also tell that the resonances for CDC occur at wavelengths which had lower transmittance with a straight channel. Similar kind of behavior can be observed at different wavelengths for the silver gratings (Fig. 2.7b)
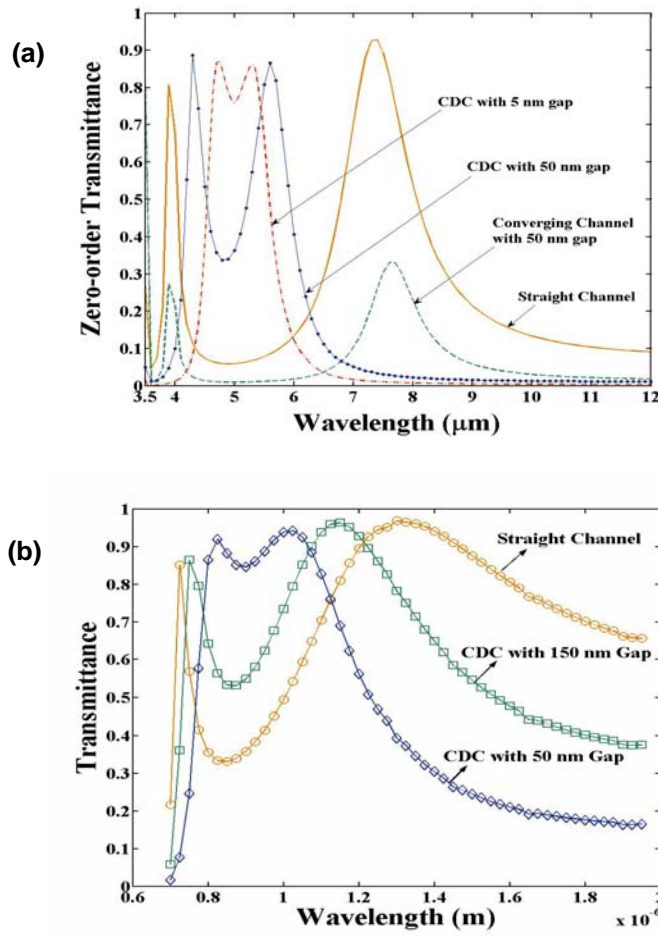
Figure 2.7: Zero-order transmittance for a normal incident plane wave on lamellar gratings in vacuum for different channel configurations, but with the same grating parameters as (a) d = 3.5 μm, a = 0.5 μm and t = 3.0 μm in gold film. (b) d = 650 nm, a = 300 nm and t = 500 nm in silver film.

By varying the angle of incidence 'θ' we can calculate the photonic band structure (PBS), $\omega(k_x)$, of these transmission resonances or surface excitations of the metallic gratings. Using the PBS, both the spectral position and the width of transmission peaks can be found. In Fig. 2.8a we show the PBS of a grating with straight channel in vacuum. Also, we show the energetic positions of the SPP modes (white dashed lines) for a nearly flat metal surface. Fig. 2.8a shows that there are two transmission resonance bands, with the higher energy band following close to the SPP mode energetic positions and the other band present at lower energy (~ 0.17 eV) is almost independent of 'θ'. This result is in close agreement to that obtained previously [16]. When the channel shape is changed to CDC the locations of the high transmission resonance bands in the PBS change from their previous energy positions and the bands appear to approach each other (Fig. 2.8b-2.8d). Fig. 2.8b shows that the CDC with 100 nm gap at throat broadens the higher energy band and contracts the lower energy band in comparison to the straight channel (Fig. 2.8a). This is because the change in channel shape affects the wavevector of the propagating wave inside the channel, which in turn might make the phases of the standing wave across the grating to be in- or out-of tune. The phases across the grating have to be in-phase for a Fabry-Perot or waveguide kind of resonance to occur, which is necessary for the high transmission to occur in SPP resonant metallic gratings [15]. Also, the lower energy band (Fig. 2.8b) is now dependent on 'θ' at higher angles. In addition, the transmittance above the first order diffraction limit has increased for higher 'θ', when compared to that of a straight channel (Fig. 2.8a). With further decrease in the gap at throat to 50 nm (Fig. 2.8c) the band at the lower energy has become more dependent on 'θ' and the transmittance above the first order diffraction has increased more, but now

37

over a shorter range of energy spectrum when compared to that of the 100 nm gap (Fig. 2.8b). Fig. 2.8d shows that with a 5 nm gap at the throat the transmission above the first order diffraction at higher θ has a Gaussian distribution over the energy spectrum. Also, it is shown that the two resonance bands have now almost merged together with negligible transmittance everywhere else below the first order diffraction limit. Hence, it should be pointed out that with very small gap at the throat the transmission over the entire energy spectrum could be made high only in a very narrow band. This means that there would be only one transmission band at a particular gap near the throat where the previous high and low energy bands mix or overlap to give a single '*hybrid band*'. Fig. 2.8a-2.8d shows quantitatively; when the gap at the throat decreases from 500 nm to 5 nm, the separation between the two transmission bands for very small angles also decreases from 0.145 eV to 0.025 eV. Moreover, the transmission near the first order diffraction limit decreases with the decrease in gap at the throat (Fig. 2.8).
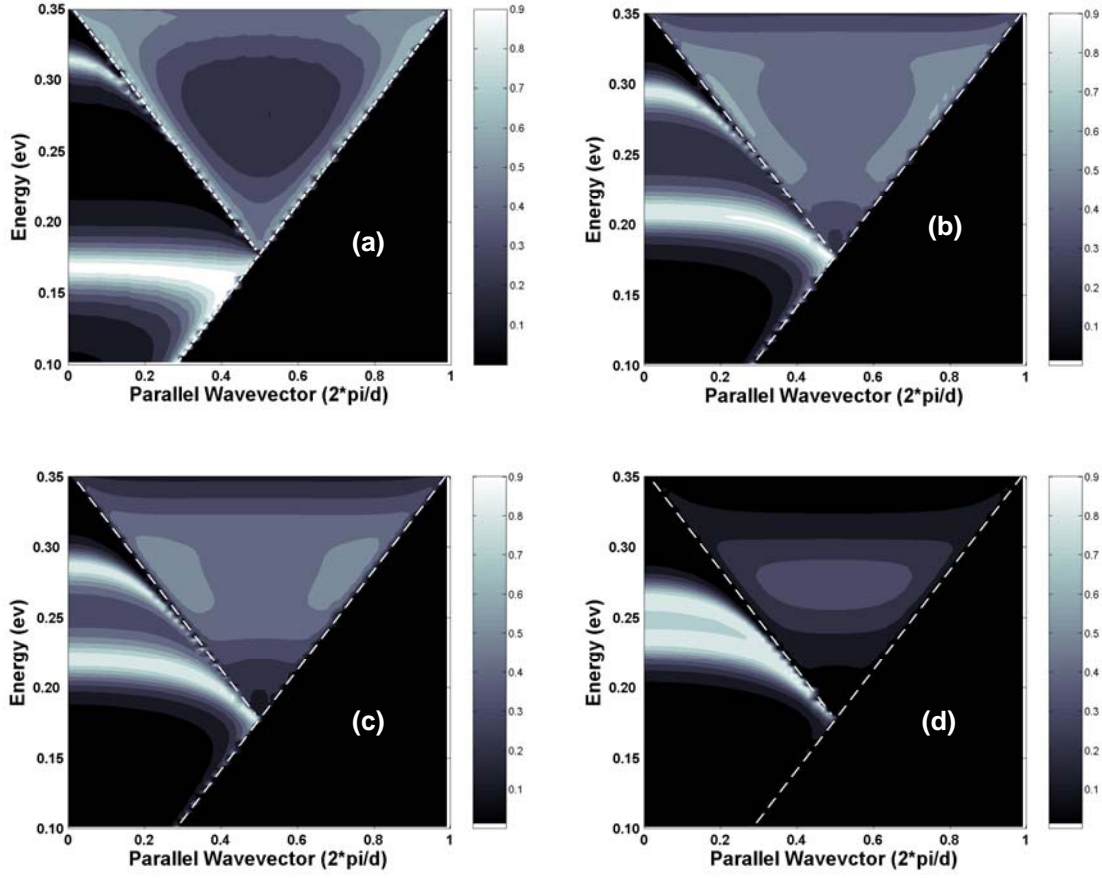
Figure 2.8: Photonic band structure of the surface plasmons responsible for the transmission resonances of gold gratings in vacuum with slit shape as (a) straight channel, (b) CDC with g = 100 nm, (c) CDC with g = 50 nm, and (d) CDC with g = 5 nm. The grating parameters are fixed at d = 3.5 μm, a = 0.5 μm, and t = 3.0 μm. Also seen in figures are energetic positions (white dashed lines) of the SPP modes.

The evolution of this hybrid band can be seen in Fig. 2.9a, where the transmittance of CDC as a function of wavelength and gap size at the throat is shown. We can see that at ~ 7.4 μm wavelength (which corresponds to the waveguide resonance of the straight channel) the decrease in gap size at the throat would result in decrease of the transmittance. At slightly smaller wavelengths the transmittance which was low for the

straight channel would increase when gap sizes decrease and reach a maximum before decreasing any further with the decrease in gap sizes. This clearly indicates that at any given wavelength the transmittance can be made high by carefully selecting the right gap size at throat. Also, it is shown in Fig. 2.9a, around 5 μm wavelength the transmittance keeps increasing until the gap at throat is very small. At wavelengths smaller than 5 μm, the transmittance increases and decreases with the gap sizes as before. This trend continues until the wavelength is close to 3.9 μm (which corresponds to the SPP & waveguide coupled resonance of the straight channel). At 3.9 μm wavelength the transmittance variation with the gap sizes is same as that of at 7.4 μm. This indicates that the change in the channel shape from straight to CDC would lead to lower transmittance at wavelengths where already a waveguide resonance condition in the channel exists. For wavelengths lower than 3.9 μm, the transmittance is always very low for all the gap sizes at throat. Similarly kind of behavior in the visible-UV wavelength range is also observed with the aluminum CDC gratings as shown in Fig. 2.9b. Here in this figure it has been shown that a single transmission resonance band shifts in the spectral location with the change in the gap at the throat of the CDC.
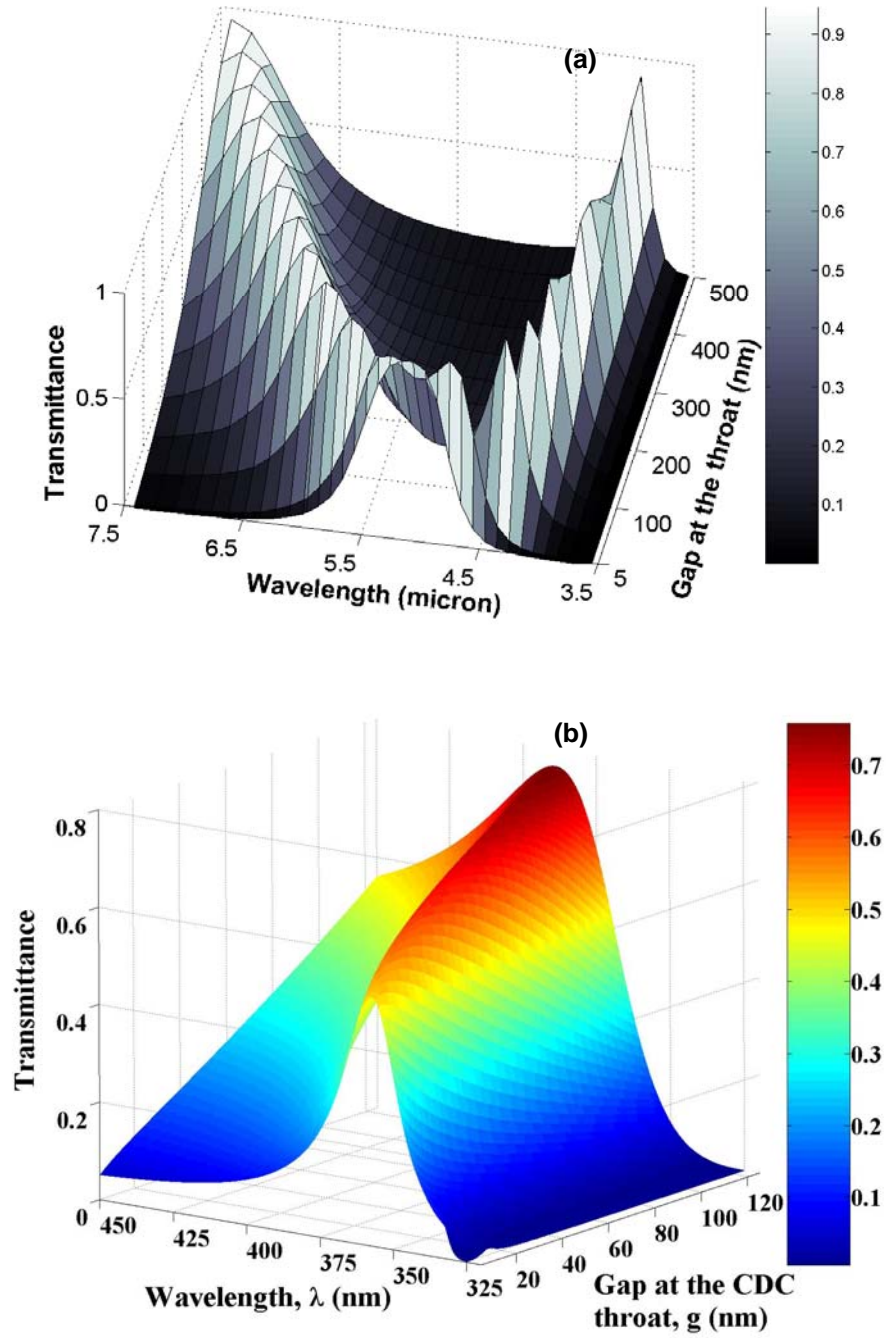
Figure 2.9: Transmittance in vacuum for CDC gratings as a function of the wavelength and distance at the gap of throat for the (a) gold gratings having d = 3.5 μm, a = 0.5 μm, and t = 3.0 μm. (b) aluminum gratings having d = 315 nm, a = 125 nm and t = 100 nm.

In order to study the individual role played by the converging and diverging part of the CDC, the transmittance of a channel with only converging shape is also calculated with the gaps at throat decreasing. Fig. 2.10 shows the transmittance at ~ 6.35 µm incident wavelength for both CDC and converging channel with different gaps near the throat. It is shown that the transmittance for the converging channel decreases with the decrease in gaps at throat, whereas for CDC the transmittance increases until a certain gap at throat (~ 200 nm) and then decreases after that point, but remains higher than the converging channel transmittance for all gaps. This shows that changing the channel shape from straight to only converging would not result in higher transmittance. Also, both the converging and diverging part of CDC would play a combined role that would result in higher transmittance.
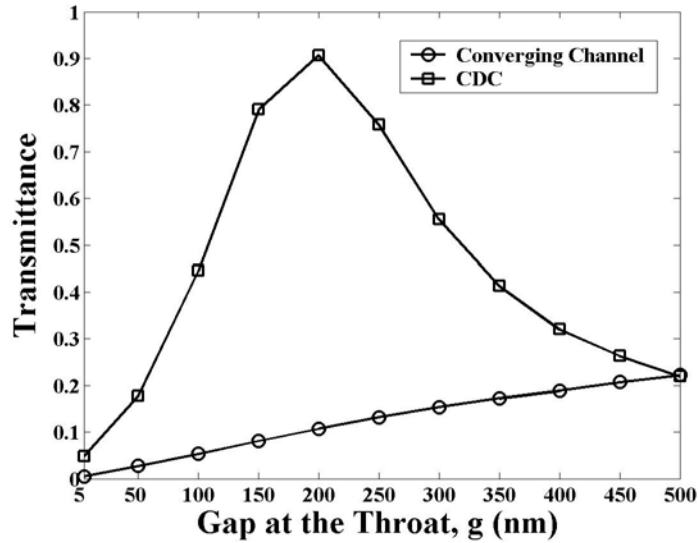
Figure 2.10: Transmittance of a gold grating in vacuum with channel shape as CDC and converging at incident wavelength of 6.35 µm and with the grating parameters as d = 3.5 µm, a = 0.5 µm and t = 3.0 µm.

The normalized magnitude of the x-component electric field ($|E_x|$) along the center line of the channel at ~ 6.35 μm wavelength for the converging channel and CDC are shown in Fig. 2.11. The variation of $|E_x|$ in the channel is proportional to the distribution of charges on the metallic grating channel surfaces. Also by looking at the $|E_x|$ distribution along the channel would tell whether the wave inside the channel is in-phase or out-of-phase. In Fig. 2.11a, we show that when the gap is 500 nm, the wave inside the channel is an out-of-phase standing wave. This is because the minimum magnitude (or node) is not at the center of the channel and the magnitudes near the end of channels (or anti-nodes) are not equal. This indicates that at the end of channel, the dipoles have unequal strength which could be due to the destructive interference of the wave inside the channel [48]. The surface charges oscillate between these two anti-nodes leading to the surface current that couples to the incident light and transmits it to the other side of grating. With the decrease in gaps near the throat, the node moves further away from the center and hence the wave inside the channel goes more out-of-phase. Also, when the gap near the throat keeps decreasing, the dipole at the throat starts to gain in strength and become stronger than the dipole at the other end of channel. This causes very less net current or energy to flow out of the channel. Similarly, by looking at the $|E_x|$ distributions in Fig. 2.11b, we show that the wave inside the channel of CDC is a standing wave for different gaps near the throat. As the gap in CDC keeps decreasing, the node keeps moving toward the center of channel. Also, the magnitudes of $|E_x|$ at two anti-nodes are increasing and becoming equal. This shows that the CDC shape of the channel is aiding the wave inside the channel to become an in-phase standing wave. The condition for in-phase resonance inside the channel is given by [15] $2Kt + \Delta\phi = m2\pi$,

where 'K' is the wavevector of the resonance and '$\Delta\phi$' is the phase change on the aperture of the slits. The role of throat is that for various gap sizes the length of the channel surface would change and hence would result in having different resonance wavevector. This can be seen from Fig. 2.10 and Fig. 2.11b where it is shown that at 6.35 µm wavelength the high transmittance happens at 200 nm gap near the throat, which has a standing wave inside the channel that is in-phase. A small decrease in the gap from 200 nm makes the standing wave inside the channel to go out-of-phase and so the transmittance decreases. When the gap at throat becomes smaller, then the charges at throat gain strength, just like in the case of converging channel (Fig. 2.11a). This would not allow light to transmit more efficiently.
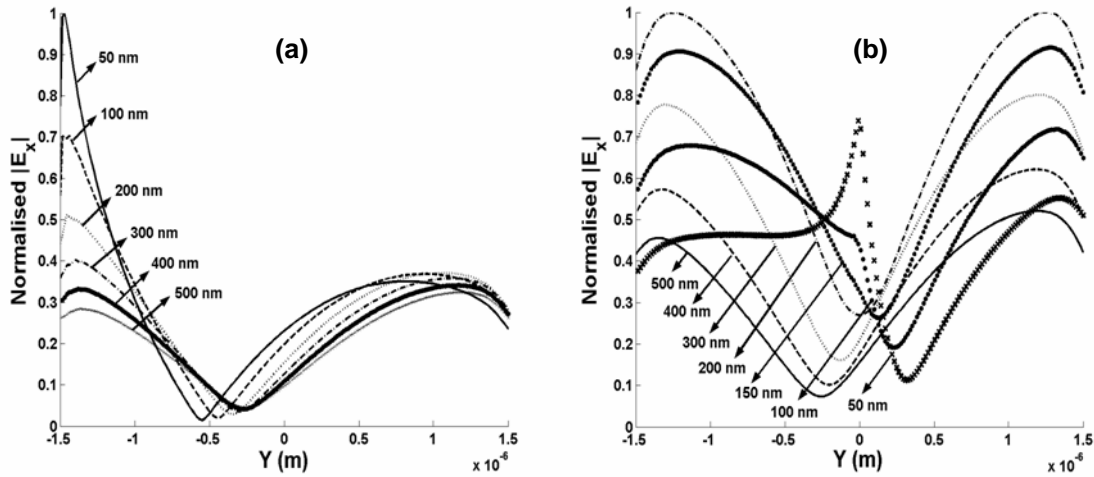
Figure 2.11: Normalized electric field x-component ($|E_x|$) at an incident wavelength of 6.35 µm along the channel center line of a gold grating in vacuum with (a) converging channel and (b) CDC for different gaps at the throat and grating parameters as d = 3.5 µm, a = 0.5 µm and t = 3.0 µm.

2.3.2 Metallic holes with CDC

Figure 2.12 shows the transmission spectrum for Ag MHAs having various aperture sizes. The transmission spectrum changes when the aperture size decreases. But, the magnitude of the transmission peak remains the same when the aperture size increase and this is unexpected according to the Bethe power law model [3]. According to the model the transmissivity for a single hole should vary with $(A/\lambda)^4$, where 'A' is the aperture size and 'λ' is the wavelength of light. This could be because the transmission through the holes might have reached saturation with respect to the open air fraction of the metallic film [54]. The full width at half maximum (FWHM) of the transmission peaks becomes smaller when the aperture size decreases. The peak of the transmission has a blue-shift when the aperture size decreases, which is in agreement with the result reported by [54].
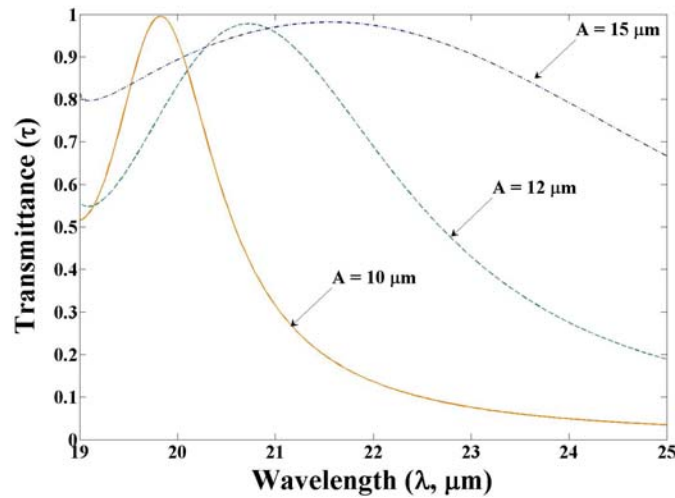
Figure 2.12: Transmission spectrum for a silver metallic hole array with a straight channel shape having period (d) = 19 μm, thickness (t) = 2 μm and different aperture sizes (A).

45

Figure 2.13 shows the transmission spectrum for different MHAs having CDC shape and straight channel shape. For CDC shape smaller throat sizes 'g' are considered while the aperture size 'A' is fixed at 10 μm. It can be observed that the straight channel has a broader transmission peak. When the channel shape is changed to CDC then the transmittance peaks become narrower along with a blue-shift. The peak location for blue-shift is larger when the throat gets smaller. In addition the decay of the transmission after the peak is largest for the CDC shape MHA with smaller throat when compared to the other cases. Also, it is to be noted that the transmission peak magnitudes do not decrease with the CDC shape.

Figure 2.14 shows the transmittance of MHAs at $\lambda = 20$ μm for two different aperture sizes with varying 'g'. For A = 10 μm the MHA with a straight channel (g = 10 μm) has higher transmission when compared to the CDC shape with different throat sizes. The transmission decreases exponentially with the decrease in the throat size and reaches '0' value asymptotically. For A = 12 μm the transmission for the straight channel (g = 12 μm) is not the highest. But, the CDC shape with approximately g = 9.75 μm has an almost perfect transmittance and is the highest. Hence, it can be seen from Fig. 2.14 that when A = 12 μm the transmittance increases as the throat size reduces until it reaches a maximum transmission and then decreases exponentially with the decrease in the 'g'. This suggests that the CDC shape with a particular 'g' aids the mediation of SPP mode coupling between the incident and transmitted surfaces. Similar kind of behavior was observed previously in gold metallic gratings having CDC shape [26]. It is to be noted that the small variation in transmittance for A = 12 μm near the peak is due to the numerical calculations with different mesh densities.

46
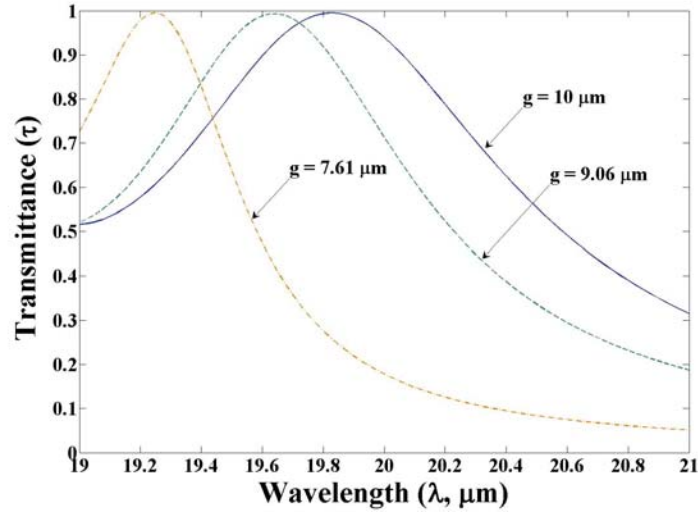
Figure 2.13: Transmission spectrum for silver metallic hole array with converging-diverging channel having period (d) = 19 μm, thickness (t) = 2 μm, aperture (A) = 10 μm and different gaps at the throat (g).
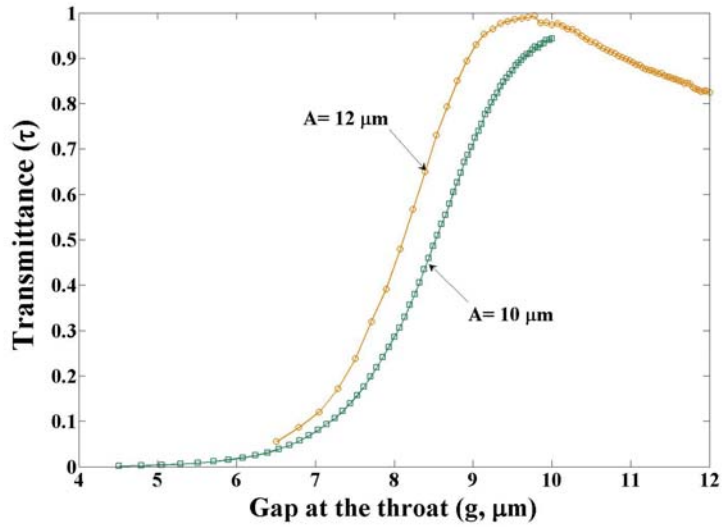
Figure 2.14: Transmittance at wavelength (λ) = 20 μm for silver metallic hole array with converging-diverging channel having period (d) = 19 μm, thickness (t) = 2 μm, different aperture sizes (A) and varying gaps at the throat (g).

47

Figure 2.15 shows the transmittance of the MHA for varying film thickness (t) at two different wavelengths. For the straight channel MHA with t = 2 μm the transmittance is maximum at λ = 19.825 μm (Fig. 2.13). At this wavelength the transmittance through the straight channel MHA does not vary much with 't' (Fig. 2.15). In the CDC case the transmittance is maximum with t = 2 μm at λ = 19.25 μm (Fig. 2.13). At this wavelength the transmittance would increase as the film thickness increases until it reaches a maximum for 't' around 1.9 μm (Fig. 2.15) and then would decrease with the increase in thickness. There is a small dip in the transmittance near the peak. This indicates that the CDC shape MHAs are sensitive to the film thickness when compared to the straight channel MHAs.
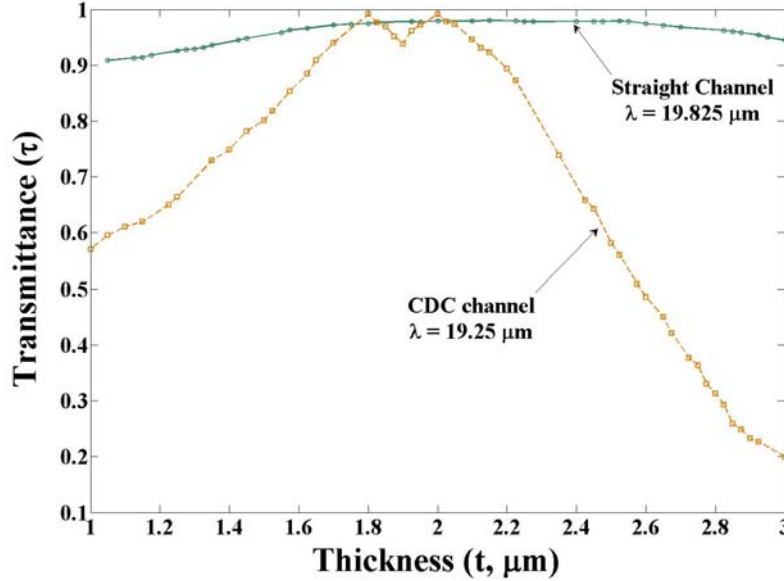
Figure 2.15: Transmittance variation with respect to the film thickness at different wavelengths (λ) for silver metallic hole array having period (d) = 19 μm, aperture size (A) = 10 μm for straight channel and converging-diverging channel with gap at the throat (g) = 7.61 μm.

Figure 2.16 shows the transmittance of different MHAs with respect to wavelength and aperture size 'A' or throat size 'g' (since, $g = A - \tan(\theta)*t$) where 'θ' (Fig. 2.14b) and the thickness is held fixed. Fig. 2.16a shows the transmittance for MHAs with straight channel or $\theta = 0^o$. It can be seen that at large aperture the transmittance is high at large wavelengths and decreases very slowly as the wavelength reduces. But, when the aperture is small the transmittance is high at lower wavelengths and it decrease very sharply as the wavelength increases. Also, it can be noted from Fig. 2.16a is that the location of the transmittance peak spectrum changes linearly as the 'A' or 'g' decreases. In addition, the full width at half maximum (FWHM) of the transmittance peaks is large when the aperture is big and it becomes very narrow as the aperture reduces. Similar kind of transmittance variation (Fig. 2.16b) is observed for the CDC MHA having $\theta = 50^o$. But, this time transmission suffers a cut-off aperture size where there is no transmittance below a particular aperture size. Furthermore the location of the transmittance peak spectrum with respect to the aperture or throat size is not exactly linear. When the 'θ' in CDC MHA increases to 65° (Fig. 2.16c) and 72° (Fig. 2.16d) the cut-off aperture for zero transmittance increases.
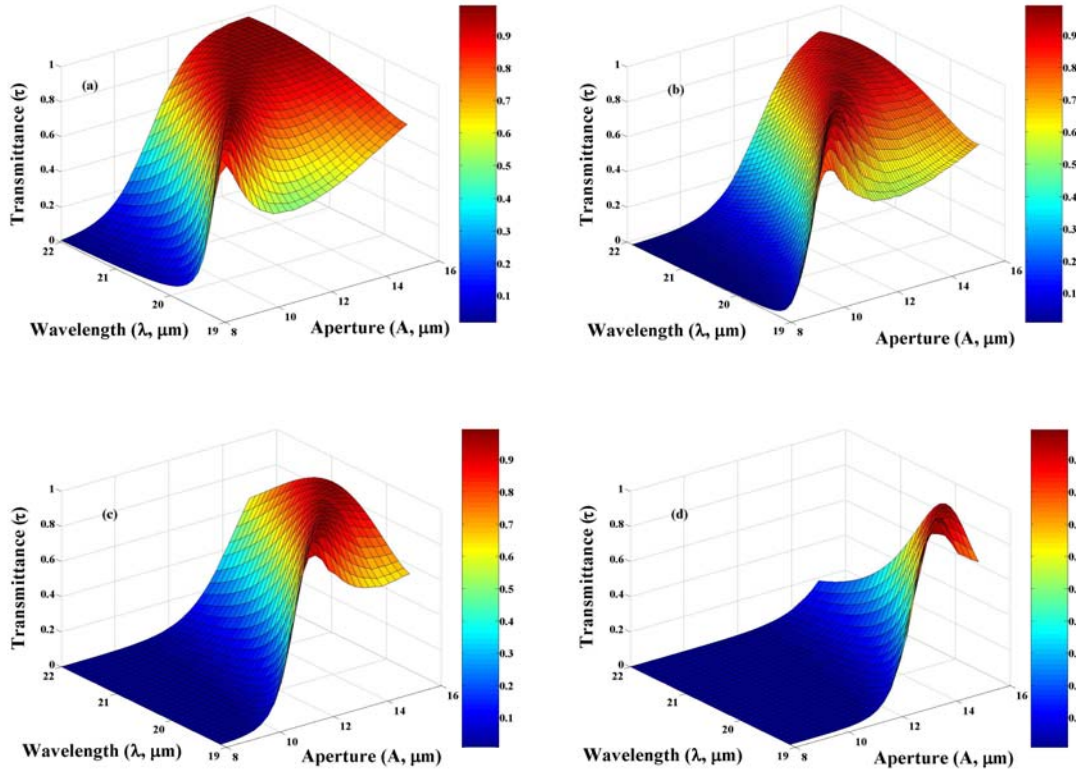
Figure 2.16. Transmittance spectrum of silver metallic hole array with period (d) = 19 μm, thickness (t) = 2 μm for varying aperture sizes (A) and hole channel shapes as (a) straight, (b) CDC shape with angle (θ) = 50°, (c) CDC shape with angle (θ) = 65°, and (d) CDC shape with angle (θ) = 72°.

2.4 TRANSMISSION THROUGH METALLIC SUBWAVELENGTH HOLES UNDER THE INFLUENCE OF EXTERNAL MAGNETIC FIELD

Figure 2.17 shows the transmission spectra in the visible and near IR region for various long and narrow rectangular hole arrays. The two high transmission peaks observed are due to the cavity resonance in the rectangular holes that can be regarded as a slit of definite length which can support standing waves [55]. At the first transmission peak (λ = 814 nm), the hole has a resonance that is very close to a complete standing

50

wave or a second harmonic and at the second transmission peak ($\lambda = 1118$ nm) the hole has a resonance that is almost like a half standing wave or a first harmonic. The number of transmission peaks can be determined by the cavity resonance or Fabry-Pérot resonance condition: $m\lambda/\text{real}(n_{eff}) = 2d$, where 'm' is an integer, n_{eff} is called effective index and 'd' is the thickness of the metal film [56]. The location of both transmission peaks have a blue-shift when the single hole array width is increased from w = 60 nm to w = 120 nm. This is due to the decrease in n_{eff} with the increase in width of the hole or slit [56] that would then shift the resonance condition to lower wavelengths. However, when a single hole (w = 120 nm) is split into two holes with smaller width (w = 60 nm) and has a space (s= 60 nm) between them, then the transmission peaks would have red-shift. This might again be explained by an increase in n_{eff} due to the decrease in hole width but not as much as of single hole array with the same width. Because the hole pair array would have a resonance mode with 'z' component wavevector (k_z) different from the single hole array, which then would lead to a different n_{eff} (= k_z/k_o; where k_o is the free space wavevector [56]). Also it is to be noted that the double hole array has transmission peak magnitudes bigger than the single hole array having the same width. In addition, the double hoe array has transmission peaks that are well separated in comparison to the single hole array having an equivalent width (w = 120 nm). It was also found out that there is no transmission when the incident light has transverse electric (TE) polarization, i.e., when the incident light polarization is parallel to the hole length. The rectangular holes can be considered as finite length lamellar gratings when the length of holes is much bigger than the width of the holes and it has been reported [48] that the transmission of metallic gratings for TE polarization suffers a cut-off wavelength.
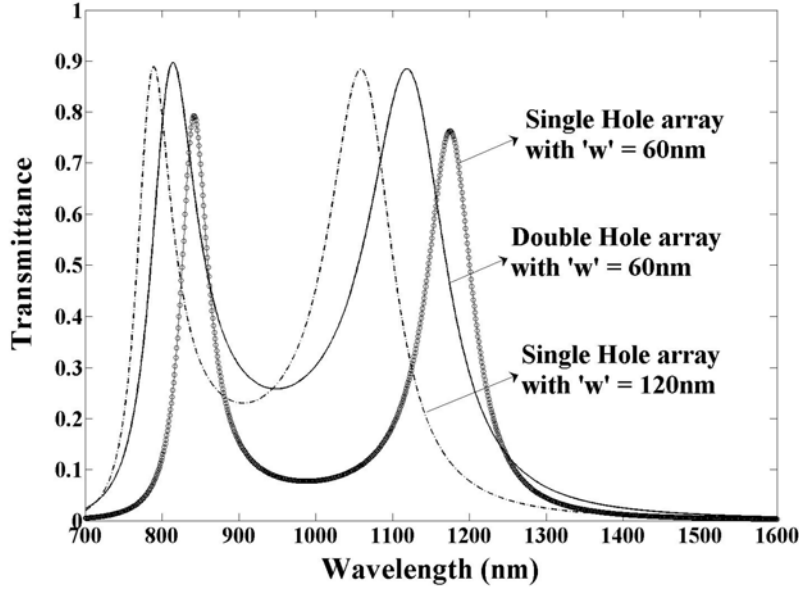
Figure 2.17: Transmission spectrum of a TM polarized light through a thin Ag film perforated with rectangular hole array having w = 60 nm (continuous line with open circle), rectangular hole pair array having w = 60 nm and s = 60 nm (continuous line) and rectangular hole array having w = 120 nm (dashed line).

The effect of applied **H** with different orientation and magnitude on the TM polarized light transmission spectra through the thin Ag film perforated with a rectangular hole pairs can be seen in Fig. 2.18. When the **H** direction is parallel to the incident polarization (**H**$_\parallel$) then as the magnitude is increasing the locations of both the transmission peaks have a blue-shift (Fig. 2.18a). This is in accordance to results obtained by [42, 52, 57] which reported that the transmission peaks which appear at SPs resonance locations would move to higher frequencies or lower wavelengths with increasing |**H**|. Whereas, in the current study the transmission peaks are mainly due to the cavity resonance. Hence, the increase in applied **H** would lower the 'ε' tensor components

except for the diagonal element that is in the direction of applied $\mathbf{H}$ and this might result in smaller n_{eff} which would shift the transmission peak resonances to lower wavelengths. The shift in the first transmission peaks is approximately 35 nm for the $\mathbf{H}$ range considered and the shift in second transmission peaks is much bigger, in the range of 110 nm for the $\mathbf{H}$ range considered. Similarly the applied $\mathbf{H}$ in the direction perpendicular to the incident polarization ($\mathbf{H_t}$) but still in-plane to the metal surface would result in a similar blue-shift for the second transmission peak (Fig. 2.18b). Whereas, the first transmission peak has very small shift and a new small transmission dip seems to evolve with the increase in $\mathbf{H_t}$, this can be seen clearly in Fig. 2.18c. The transmission peak on the lower wavelength side of the dip has a strong cavity resonance similar to the second harmonic. Whereas, the transmission peak on the higher wavelength side of the dip has an off cavity resonance and this suggests that the high transmission might be due to a resonance of in-plane SPs excited on the front and back surface of the metal film. Hence the dip near the first transmission peak is due to the off resonances of both the cavity and in-plane SPs. Fig. 2.18d shows that when the applied $\mathbf{H}$ is in the direction of the propagation of the incident light ($\mathbf{H_k}$) then the increase in its magnitude would result in a similar shift of the transmission peaks to lower wavelengths as observed in (Fig 2.18a). Except for now the range of shift for the first transmission peak is smaller for $\mathbf{H_k}$ when compared to the $\mathbf{H_\parallel}$. Also it is to be noted from the Fig. 2.18 that the transmission peaks are reducing in strength with the increase in $\mathbf{H}$ magnitude and the rate of decrease is more for the second transmission peak when compared to the first peak. But the strength of the transmission peaks is similar for different $\mathbf{H}$ orientation and the $\mathbf{H_\parallel}$ situation has a larger blue-shift for both the transmission peaks.

53
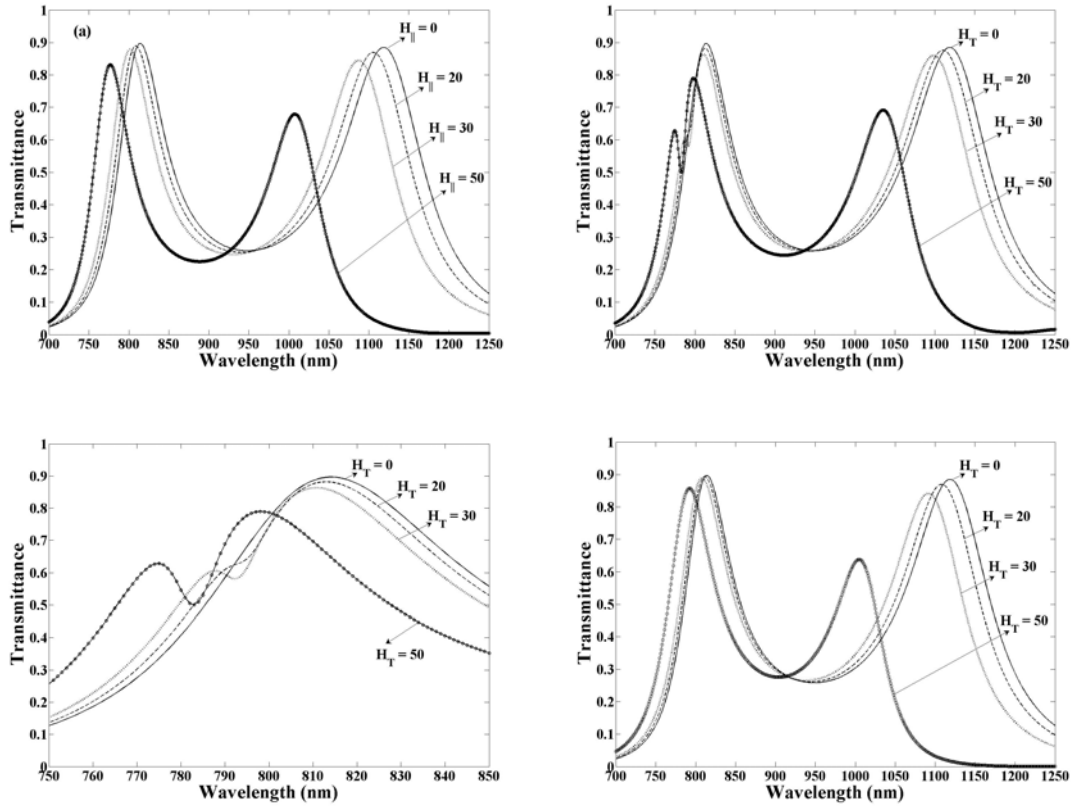
Figure 2.18: Transmission spectrum of a TM polarized light through a thin Ag film perforated with rectangular hole pair square array having w = 60 nm and s = 60 nm for magnetic field $|\mathbf{B_o}|$ (= H/μ, where μ is Hall mobility) applied in the direction (a) parallel to the incident polarization, (b) and (c) perpendicular to the incident polarization but in-plane to the metal film and (d) parallel to the propagation direction of the incident light.

2.5 CONCLUSION

In conclusion, it was shown that with CDC metallic gratings the transmission peaks can be selected by varying the width of gaps at the throat. Also, high transmission resonances in a very narrow band can be achieved. It has also been shown that the

transmission spectrum of metallic hole arrays (MHAs) with converging-diverging channel (CDC) changes with the gap at the throat. The transmission peaks have blue-shift when the throat size reduces. Whereas, MHAs with straight channel and large aperture have broad transmission peaks at bigger wavelength. But, when the aperture size decreases the transmission peaks shift to a lower wavelength and become narrower. It is also shown that the transmittance can be increased when the MHA channel changes from straight to CDC. But, the transmittance of MHAs with CDC shape suffers a cut-off aperture size below which there will be no transmission. The cut-off aperture size increases as the angle (θ) of the CDC shape (Fig. 2.4b) increases. Also, it has been shown that the transmittance of MHAs with straight channel does not change much with the thickness of the film. But, for the MHA with CDC shape the transmittance is very sensitive to the thickness of the film. The proposed CDC shape in MHAs could lead to extraordinary transmission at any wavelength that has a wide range of potential applications in integrated photonic circuits, tunable filters, near-field optics, imaging nanolithography and biological sensors.

In addition it was also shown that for a rectangular hole pair array Ag film the presence of externally applied magnetic field $\mathbf{H}$ would alter the transmission resonance peak locations. The shift is dependent on the magnitude and the direction of the $\mathbf{H}$. This is due to the shift of cavity resonance condition as a result of the magento-induced anisotropy in the optical properties of the metallic film. The transmission resonances have blue-shift in the locations with the increase in $\mathbf{H}$. The $\mathbf{H}_t$ case has resulted in a new smaller transmission dip which is due to the off resonances of both the cavity and in-plane SPs. The $\mathbf{H}_\parallel$ case has more blue-shift when compared to other directions of the $\mathbf{H}$

and so it could be the most favorable setting while building a tunable optical device with

an external electro-magnet that would not interfere with the path of incident light.

Reference

[1]. W. L. Barnes, T. W. Preist, S. C. Kitson, J. R. Sambles, "Physical origin of photonic energy gaps in the propagation of surface plasmons on gratings", *Physical Review B*, **54**, 6227-6244 (1996).
[2]. S. C. Kitson, W. L. Barnes, J. R. Sambles, "Full photonic band gap for surface modes in the visible", *Physical Review Letters*, **77**, 2670-2673 (1996).
[3]. H. A. Bethe, "Theory of Diffraction by Small Holes", *Physical Review*, **66**, 163-182 (1944).
[4]. T. W. Ebbesen, H. J. Lezec, H. F. Ghaemi, T. Thio, P. A. Wolff, "Extraordinary optical transmission through sub-wavelength hole arrays", *Nature*, **391**, 667-669 (1998).
[5]. C. Genet, T. W. Ebbesen, "Light in tiny holes", *Nature*, **445**, 39-46 (2007).
[6]. F. J. Garcia-Vidal, L. Martin-Moreno, "Transmission and focusing of light in one-dimensional periodically nanostructured metals", *Physical Review B*, **66**, - (2002).
[7]. J. A. Dionne, L. A. Sweatlock, H. A. Atwater, A. Polman, "Planar metal plasmon waveguides: frequency-dependent dispersion, propagation, localization, and loss beyond the free electron model", *Physical Review B*, **72**, - (2005).
[8]. H. J. Lezec, T. Thio, "Diffracted evanescent wave model for enhanced and suppressed optical transmission through subwavelength hole arrays", *Optics Express*, **12**, 3629-3651 (2004).
[9]. Q. Cao, P. Lalanne, "Negative role of surface plasmons in the transmission of metallic gratings with very narrow slits", *Physical Review Letters*, **88**, - (2002).
[10]. W. L. Barnes, W. A. Murray, J. Dintinger, E. Devaux, T. W. Ebbesen, "Surface plasmon polaritons and their role in the enhanced transmission of light through periodic arrays of subwavelength holes in a metal film", *Physical Review Letters*, **92**, - (2004).
[11]. R. Sambles, "Photonics - More than transparent", *Nature*, **391**, 641-642 (1998).
[12]. D. Maystre, M. Neviere, "Quantitative Theoretical-Study on Plasmon Anomalies of Diffraction Gratings", *Journal of Optics-Nouvelle Revue D Optique*, **8**, 165-174 (1977).
[13]. S. Collin, F. Pardo, R. Teissier, J. L. Pelouard, "Horizontal and vertical surface resonances in transmission metallic gratings", *Journal of Optics a-Pure and Applied Optics*, **4**, S154-S160 (2002).
[14]. E. Popov, M. Neviere, S. Enoch, R. Reinisch, "Theory of light transmission through subwavelength periodic hole arrays", *Physical Review B*, **62**, 16100-16108 (2000).
[15]. X. Jiao, P. Wang, L. Tang, Y. Lu, Q. Li, D. Zhang, P. Yao, H. Ming, J. Xie, "Fabry-Perot-like phenomenon in the surface plasmons resonant transmission of metallic gratings with very narrow slits", *Applied Physics B-Lasers and Optics*, **80**, 301-305 (2005).

[16]. J. A. Porto, F. J. Garcia-Vidal, J. B. Pendry, "Transmission resonances on metallic gratings with very narrow slits", *Physical Review Letters*, **83**, 2845-2848 (1999).

[17]. D. E. Grupp, H. J. Lezec, T. W. Ebbesen, K. M. Pellerin, T. Thio, "Crucial role of metal surface in enhanced transmission through subwavelength apertures", *Applied Physics Letters*, **77**, 1569-1571 (2000).

[18]. J. F. O'Hara, R. D. Averitt, A. J. Taylor, "Terahertz surface plasmon polariton coupling on metallic gratings", *Optics Express*, **12**, 6397-6402 (2004).

[19]. F. Miyamaru, M. Hangyo, "Finite size effect of transmission property for metal hole arrays in subterahertz region", *Applied Physics Letters*, **84**, 2742-2744 (2004).

[20]. H. Cao, A. Nahata, "Influence of aperture shape on the transmission properties of a periodic array of subwavelength apertures", *Optics Express*, **12**, 3664-3672 (2004).

[21]. D. X. Qu, D. Grischkowsky, W. L. Zhang, "Terahertz transmission properties of thin, subwavelength metallic hole arrays", *Optics Letters*, **29**, 896-898 (2004).

[22]. C. Janke, J. G. Rivas, C. Schotsch, L. Beckmann, P. H. Bolivar, H. Kurz, "Optimization of enhanced terahertz transmission through arrays of subwavelength apertures", *Physical Review B*, **69**, - (2004).

[23]. J. G. Rivas, C. Schotsch, P. H. Bolivar, H. Kurz, "Enhanced transmission of THz radiation through subwavelength holes", *Physical Review B*, **68**, - (2003).

[24]. A. K. Azad, Y. Zhao, W. Zhang, "Transmission properties of terahertz pulses through an ultrathin subwavelength silicon hole array", *Applied Physics Letters*, **86**, - (2005).

[25]. J. B. Pendry, L. Martin-Moreno, F. J. Garcia-Vidal, "Mimicking surface plasmons with structured surfaces", *Science*, **305**, 847-848 (2004).

[26]. M. Tanaka, F. Miyamaru, M. Hangyo, T. Tanaka, M. Akazawa, E. Sano, "Effect of a thin dielectric layer on terahertz transmission characteristics for metal hole arrays", *Optics Letters*, **30**, 1210-1212 (2005).

[27]. R. Gordon, A. G. Brolo, A. McKinnon, A. Rajora, B. Leathem, K. L. Kavanagh, "Strong polarization in the optical transmission through elliptical nanohole arrays", *Physical Review Letters*, **92**, - (2004).

[28]. K. J. K. Koerkamp, S. Enoch, F. B. Segerink, N. F. van Hulst, L. Kuipers, "Strong influence of hole shape on extraordinary transmission through periodic arrays of subwavelength holes", *Physical Review Letters*, **92**, - (2004).

[29]. X. L. Shi, L. Hesselink, R. L. Thornton, "Ultrahigh light transmission through a C-shaped nanoaperture", *Optics Letters*, **28**, 1320-1322 (2003).

[30]. J. A. Matteo, D. P. Fromm, Y. Yuen, P. J. Schuck, W. E. Moerner, L. Hesselink, "Spectral analysis of strongly enhanced visible light transmission through single C-shaped nanoapertures", *Applied Physics Letters*, **85**, 648-650 (2004).

[31]. Y. H. Ye, D. Y. Jeong, Q. M. Zhang, "Fabrication of strain tunable infrared frequency selective surfaces on electrostrictive poly(vinylidene fluoride-trifluoroethylene) copolymer films using a stencil mask method", *Applied Physics Letters*, **85**, 654-656 (2004).

[32]. W. J. Fan, S. Zhang, B. Minhas, K. J. Malloy, S. R. J. Brueck, "Enhanced infrared transmission through subwavelength coaxial metallic arrays", *Physical Review Letters*, **94**, - (2005).

[33]. Q. J. Wang, J. Q. Li, C. P. Huang, C. Zhang, Y. Y. Zhu, "Enhanced optical transmission through metal films with rotation-symmetrical hole arrays", *Applied Physics Letters*, **87**, - (2005).

[34]. C. L. Pan, C. F. Hsieh, R. P. Pan, M. Tanaka, F. Miyamaru, M. Tani, M. Hangyo, "Control of enhanced THz transmission through metallic hole arrays using nematic liquid crystal", *Optics Express*, **13**, 3921-3930 (2005).

[35]. K. Nishio, H. Masuda, "Dependence of optical properties of ordered metal hole array on refractive index of surrounding medium", *Electrochemical and Solid State Letters*, **7**, H27-H28 (2004).

[36]. A. Degiron, H. J. Lezec, W. L. Barnes, T. W. Ebbesen, "Effects of hole depth on enhanced light transmission through subwavelength hole arrays", *Applied Physics Letters*, **81**, 4327-4329 (2002).

[37]. A. K. Azad, W. L. Zhang, "Resonant terahertz transmission in subwavelength metallic hole arrays of sub-skin-depth thickness", *Optics Letters*, **30**, 2945-2947 (2005).

[38]. S. J. Oldenburg, R. D. Averitt, S. L. Westcott, N. J. Halas, "Nanoengineering of optical resonances", *Chemical Physics Letters*, **288**, 243-247 (1998).

[39]. A. K. Zvezdin, V. A. Kotov, *Modern magnetooptics and magnetooptical materials*, Studies in condensed matter physics (Institute of Physics Pub., Bristol ; Philadelphia, PA, 1997).

[40]. P. N. Prasad, *Nanophotonics* (Wiley-Interscience, Hoboken, N.J., 2004).

[41]. A. Garcia-Martin, G. Armelles, S. Pereira, "Light transport in photonic crystals composed of magneto-optically active materials", *Physical Review B*, **71**, - (2005).

[42]. Y. M. Strelniker, D. J. Bergman, "Optical transmission through metal films with a subwavelength hole array in the presence of a magnetic field", *Physical Review B*, **59**, 12763-12766 (1999).

[43]. M. Diwekar, V. Kamaev, J. Shi, Z. V. Vardeny, "Optical and magneto-optical studies of two-dimensional metallodielectric photonic crystals on cobalt films", *Applied Physics Letters*, **84**, 3112-3114 (2004).

[44]. V. I. Belotelov, L. L. Doskolovich, A. K. Zvezdin, "Extraordinary magneto-optical effects and transmission through metal-dielectric plasmonic systems", *Physical Review Letters*, **98**, - (2007).

[45]. J. D. Jackson, *Classical electrodynamics* (Wiley, New York, ed. 3rd, 1999).

[46]. S. A. Maier, H. A. Atwater, "Plasmonics: Localization and guiding of electromagnetic energy in metal/dielectric structures", *Journal of Applied Physics*, **98**, - (2005).

[47]. D. R. Lide, *handbook of chemistry and physics* (CRC Press, Cleveland, Ohio, 1992), vol. 58th ed. (1977-1978)-.

[48]. Y. Xie, A. R. Zakharian, J. V. Moloney, M. Mansuripur, "Transmission of light through slit apertures in metallic films", *Optics Express*, **12**, 6106-6121 (2004).

[49]. A. Lavrinenko, P. I. Borel, L. H. Frandsen, M. Thorhauge, A. Harpoth, M. Kristensen, T. Niemi, H. M. H. Chong, "Comprehensive FDTD modelling of photonic crystal waveguide components", *Optics Express*, **12**, 234-248 (2004).

[50]. P. W. Barber, S. C. Hill, *Light scattering by particles : computational methods*, Advanced series in applied physics v. 2 (World Scientific, Singapore ; Teaneck, N.J., 1990).

[51]. E. D. Palik, Ed., *Handbook of optical constants of solids* (Academic Press, Orlando, 1985).

[52]. D. J. Bergman, Y. M. Strelniker, "Anisotropic ac electrical permittivity of a periodic metal-dielectric composite film in a strong magnetic field", *Physical Review Letters*, **80**, 857-860 (1998).

[53]. L. Martin-Moreno, F. J. Garcia-Vidal, H. J. Lezec, K. M. Pellerin, T. Thio, J. B. Pendry, T. W. Ebbesen, "Theory of extraordinary optical transmission through subwavelength hole arrays", *Physical Review Letters*, **86**, 1114-1117 (2001).

[54]. K. L. van der Molen, F. B. Segerink, N. F. van Hulst, L. Kuipers, "Influence of hole size on the extraordinary transmission through subwavelength hole arrays", *Applied Physics Letters*, **85**, 4316-4318 (2004).

[55]. W. L. Jia, X. H. Liu, "Origin of superenhanced light transmission through two-dimensional subwavelength rectangular hole arrays", *European Physical Journal B*, **46**, 343-347 (2005).

[56]. S. Astilean, P. Lalanne, M. Palamaru, "Light transmission through metallic channels much smaller than the wavelength", *Optics Communications*, **175**, 265-273 (2000).

[57]. G. Dresselhaus, A. F. Kip, C. Kittel, "Cyclotron Resonance of Electrons and Holes in Silicon and Germanium Crystals", *Physical Review*, **98**, 368-384 (1955).

Chapter 3: Monochromatic polarized coherent emitter enhanced by surface   plasmons and a cavity resonance

3.1 INTRODUCTION

In a thermal source, the light generation at the microscopic level is a spontaneous emission of photon when a thermally excited emitter relaxes to a lower state. Unlike the laser which produces highly directional and monochromatic light, a thermal light source is isotropic with a broad spectrum. But the thermal source of light is coherent in the near field, i.e., within a distance from the surface that is much smaller than the emission peak wavelength of the spectrum [1-3]. The coherence is due to the role of surface waves. Hence a roughness or a grating on the surface can couple these waves to propagating waves, which will extend the coherence properties into the far field. Thus by modifying the characteristics of the surface profile, the near field coherence properties can be extended to the far field in a particular direction at a given wavelength. This was first observed on a doped silicon grating supporting a surface plasmon polariton (SPP) [4]. Similarly, a peak in the thermal emission by gratings on ZnSe [5], gold [6], and SiC [7] was also observed. For these grating structures, it was noted that the excited surface waves could couple to the emitted radiation for the *p*-polarization only. No lobe of emission has been observed for *s*-polarization; since in this case the SPPs or surface waves cannot be present [8].

Using the surface waves it was shown that a one-dimensional (1D) photonic crystal (PhC) coated with SiC can have coherent thermal emission lobes for both polarizations in the stop band of the PhC [9]. Furthermore, a 1D PhC having metallic

films with thickness of the order of skin depth exhibit photonic effects that can be used to engineer the spectral emissivity of the PhC structure [10]. But the emissivity of 1D metallodielectric PhC increases over a broad spectrum and this is not suitable for monochromatic emission applications. A tunable thermal source with narrow angular emission lobe in the near-infrared (NIR) region has been shown using a thin-film structure - based on a vertical cavity and 1D PhC [11]. Yet, this kind of thermal source is not suitable for highly monochromatic applications, because the spectral emission peak has a large full width at half maximum (FWHM). The two-dimensional (2D) periodic metallic structures microfabricated exhibit optical properties due to the SPPs that can be used as wavelength selective radiation emitters or filters [12, 13]. Similarly, it was shown that a 2D PhC made of germanium has coherent thermal emission for a wavelength in the band gap and is due to the leaky surface waves on the air-PhC interface [14]. It has also been shown that the three-dimensional (3D) tungsten PhC can have higher emissivity [15, 16]. But, the 2D periodic structures and 3D PhC are intricate to fabricate and scale up. In addition, there are very few reports on spectral emittance in the visible region from periodic nanostructured materials with large spatial and temporal coherence.

A unique thermal emitter with desired properties was realized by using the unique properties of the PhCs and plasmonics (SPPs) together. Here we make use of the surface waves that are present on both the metallic gratings (plasmonics) and in the PhC structure. For the wavelength range of interest the surface waves excited on the metallic grating are always evanescent, regardless of the angle of incidence, because the dielectric constant of the metal is negative and the grating period is much smaller than the incident wavelength.

3.2 SCHEMATIC VIEW OF THERMAL EMITTER AND COMPUTATIONAL SET-UP

In this study we propose a design of a potential thermal emitter in the visible range – that is tunable, polarized, highly monochromatic, extremely directional, and with far-field spatial coherence. The proposed thermal source is a multilayer structure with a cavity surrounded by silver (Ag) lamellar gratings having converging-diverging channel (CDC) on one side and 1D PhC on the other side. The geometry of the emitter is shown in Fig. 3.1. The characteristics of the CDC gratings are the period 'Λ', the aperture 'h', the depth 't' and the gap at the throat 'g'. The 1D PhC is made out of alternating layers of SiO_2 and InSb, with the layer thickness of each equal to 50 nm. For the study we used the following grating parameters: $\Lambda = 250$ nm, h = 100 nm and t = 100 nm. These grating parameters are used for the entire study and also the cavity is filled with air. In order to arrive at the final design of the potential thermal emitter different possible designs were investigated; namely thin Ag film, Ag straight channel gratings, Ag CDC gratings with different gap at the throat and 1D PhC with various cavity lengths.

According to Kirchhoff's law, the spectral directional emissivity $\varepsilon_{\lambda,\theta}$ can be determined by using [17] $1-\rho_{\lambda,\theta}-\tau_{\lambda,\theta}$, where the spectral-directional reflectance, $\rho_{\lambda,\theta}$ and the spectral-directional transmittance, $\tau_{\lambda,\theta}$ are evaluated by using a plane monochromatic wave incident from the air at an angle of incidence 'θ' as shown in Fig. 3.1. The choice of material on the bottom side of the PhC would not be significant since the wavelength range of interest is in the stop band of the PhC (Fig. 3.2) and also the number of unit cells considered for the PhC is large. Hence both the reflectance and the transmittance are calculated in air. In the present study both *p*-polarization (magnetic field vector parallel to the gratings) and *s*-polarization (electric field vector parallel to the gratings) were used

for the analysis. The electromagnetic fields were assumed to be time harmonic. Therefore the resulting governing equation for the steady-state distribution of the electromagnetic fields is a Helmholtz equation, with the dependent variable being the magnetic field in the z-direction (H_z) or electric field in the z-direction (E_z) for *p*-polarization and *s*-polarization respectively as shown in eq. (3.10). The dielectric response of the metal (silver) used for grating in this paper is taken from the tables reported in [18]. A commercially available Finite Element software (FEMLAB 3.1i) was used for solving the governing equation. A 2D computational domain surrounded by either phase-shifted boundary conditions or by perfectly matching layer (PML) [19] was used. The spectral directional reflectance and transmittance of the gratings were calculated from the obtained electromagnetic field distributions as discussed in section 3.2. For the wavelength range considered in the paper both SiO_2 and InSb are assumed to be lossless dielectrics with refractive indices given by [18] $n_{SiO_2} = 1.46$ and $n_{InSb} = 3.95$. A freely available MIT photonic band (MPB) package was used for calculating the photonic band structure (PBS) of the PhC (Fig. 3.2a). The first or lower band-gap in the PBS is between the normalized frequency range of 0.136 to 0.217. So, a PhC having a unit cell thickness 'a' of 100 nm has first band-gap wavelength range between 460 nm to 735 nm. This can be verified with the normal or zero angle of incidence reflectance spectrum of the PhC as shown in Fig. 3.2b. When the angle of incidence increases to 45° then the wavelength range for perfect reflectance would decrease (Fig. 3.2b).

63
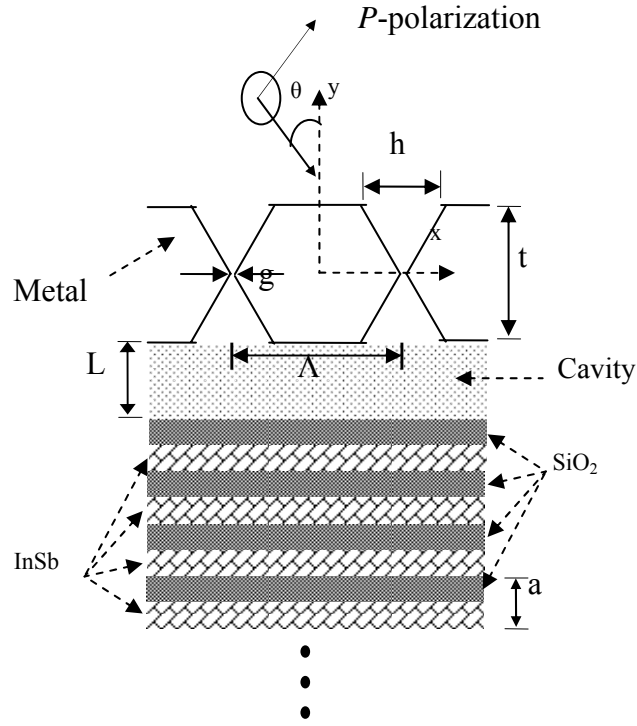
Figure 3.1: Schematic view of the thermal emitter geometry with silver (Ag) grating having converging-diverging channel (CDC) with period 'Λ' = 250 nm, aperture 'h' = 100 nm, thickness 't' = 100 nm and the photonic crystal with unit cell thickness 'a' = 100 nm; thickness of SiO_2 'd_1' = thickness of InSb 'd_2' = a/2 = 50nm along with a cavity filled with air.
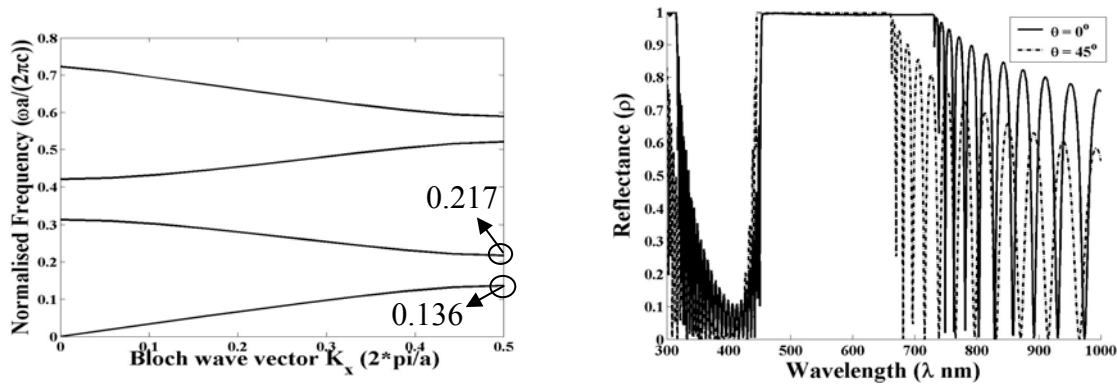
Figure 3.2: (a) Photonic band structure of the 1D PhC made of SiO_2 and InSb with equal thickness. (b) Reflectance spectrum of the 1D PhC for different angle of incidence and unit cell thickness 'a' of 100 nm.

3.3 EXTRAORDINARY NORMAL EMITTANCE IN NARROW BAND FROM SILVER GRATING AND ONE-DIMENSIONAL (1D) PHOTONIC CRYSTAL

We first investigate the emission spectrum of just a finite thin Ag film with different grating structures in it. Fig. 3.3 shows the *p*-polarized normal emittance for different thin film structures in the PhC stop band wavelength range. The normal emissivity of different structures is low and is monotonically decreasing with the wavelength. Fig. 3.3 also shows that at smaller wavelength the thin film with the straight channel gratings has higher emissive power than the remaining structures and at larger wavelength all the structures have the same emissive power. In addition it can said from Fig. 3.3 that the thin film slab emittance varies almost linearly with the wavelength, whereas the emittance of different grating structures changes inversely proportional to the wavelength.
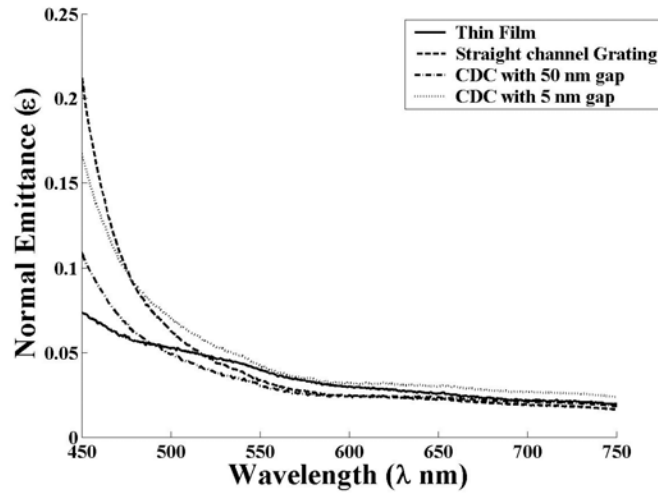
Figure 3.3: Normal emittance spectrum with *p*-polarization in vacuum for different thin Ag film structures having the grating parameters $\Lambda = 250$ nm, h = 100 nm, t = 100 nm.

65

The normal emittance spectrum of various thin film structures and 1D PhC with no cavity is shown in Fig. 3.4. Fig. 3.4a shows the normal emissivity of the thin film slab on 1D PhC with no cavity, which is similar to the normal emissivity of a thin film slab as shown in Fig. 3.3. This indicates that the thickness of the slab considered (t = 100 nm) is larger than the skin depth of the Ag for the wavelength range of interest. The straight channel grating on the 1D PhC with no cavity have multiple emission peaks in the spectrum at lower wavelength range of the spectrum, as can be seen in Fig. 3.4b. The presence of these narrow spectral emission peaks is an indication of large temporal coherence of the field at the interface and the coherence time is essentially the lifetime of the collective oscillation [20]. Each of these peaks has a very small full width at half maximum (FWHM) which is required for a good monochromatic emitter. The abrupt changes in the emission spectrum at lower wavelengths with multiple narrow emissive peaks transform gradually to a monotonic decreasing variation at higher wavelengths. At higher wavelengths there are no peaks in the emission spectrum except near the higher band-edge wavelength of 1D PhC where there are a couple of smaller peaks. Also the emissivity is very low at higher wavelength. The smaller emittance peaks are just outside the wavelength range of the PhC band-gap where there are abrupt sharp transmittance peaks. In addition, the small emittance peaks are also due to the sudden dips in the reflectance spectrum of the multi-structure. The excitation of surface plasmons (SPs) on the adjacent grating would couple and aid in the transmission of light. The coupling of the SPs would happen at only particular wavelengths. Since wavelength of transmitted light is outside PhC band-gap then there would be only a small part of the transmitted

66

light from the CDC grating that would be absorbed. Fig. 3.4c shows that when there is a CDC grating with 5 nm gap at the throat on 1D PhC with no cavity then some of the narrow emissive peaks at the lower wavelengths will reduce in the magnitude and result in having only a few bigger peaks. The FWHM for the peak at around 540 nm wavelength is about 8 nm. But the presence of few smaller peaks near the 540 nm wavelength might act like some kind of emissive noise and would make the design not a very good monochromatic thermal emitter. Also the smaller peaks that were present at the higher wavelengths for the straight channel grating case have been cancelled out with the smaller gap at the throat of the CDC grating. The multiple peaks appearing in Fig. 3.4b and Fig. 3.4c are mainly because of the coupling of SPs on the adjacent gratings which would allow most of the incoming energy or light to get transmitted through the gratings and also due to the strong resonances inside the PhC that would than capture or absorb all the energy resulting in high absorption or emission at different wavelengths. The resonance inside the PhC is all through its length. After a certain wavelength there is no coupling of SPs on adjacent gratings and also there is no resonance inside the PhC.
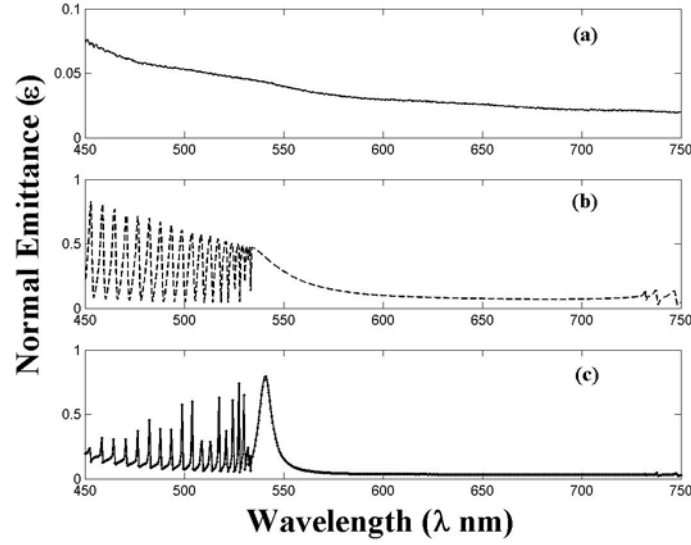
Figure 3.4: Normal emittance spectrum with *p*-polarization in vacuum for different thin Ag film structures having the same grating parameters Λ = 250 nm, h = 100 nm, t = 100 nm and a photonic crystal having the parameters a = 100 nm; d_1 = d_2 = 50 nm with no cavity (a) thin film slab, (b) grating with straight channel, and (c) grating with CDC and gap at throat 'g' = 5 nm.

Figure 3.5 shows the *p*-polarized normal emittance for various thin film structures and 1D PhC with 200 nm cavity length. This figure shows that the multiple emissive peaks that were present at the lower wavelengths for the various thin film structures and 1D PhC with no cavity would disappear when there is a cavity. It is also shown in Fig. 3.5 that the thin film slab and 1D PhC with a 200 nm cavity length has a very small peak at around 581 nm wavelength and this peak was not present when there was no cavity (as shown in Fig. 3.4a). The small emissive peak is not desirable for a good thermal emitter and it becomes bigger when the thin film slab structure is changed to a straight channel grating structure. But the new peak position shifts in spectral location to a lower wavelength of 562 nm and the FWHM of the new peak is around 32 nm. When the film

68

structure changes further to a CDC grating with 50 nm gap at the throat the new peak obtained will have an additional increase in magnitude and the spectral position of the peak shifts to 569 nm wavelength with FWHM of the peak decreasing from the previous case to around 17 nm. With an additional decrease in the gap at the throat of CDC grating to 5 nm the peak formed in the emissive spectrum has a very big increase in the magnitude and the spectral location of the peak moves to higher wavelength of around 584 nm. In addition, the FWHM of the new peak decreases further to around 4 nm, making it an excellent choice for a monochromatic thermal emitter.

The presence of a cavity between the CDC gratings and 1D PhC would change the dispersion characteristics of the SPs. The single large sharp emission peak in the case of CDC with 5 nm gap at the throat as shown in Fig. 3.5 is due to the coupling of the SPs on the adjacent CDC gratings and also due to the cavity resonance. This would then lead to peaks at only particular wavelengths where the cavity resonance like the harmonic resonances between two walls could happen. Also the presence of a narrow emission peak in the spectrum indicates the strong excitation or the resonance of the surface mode. According to the Wiener-Khinchin theorem the width of the spectrum of the field is inversely proportional to the coherence time and similarly a narrow peak in a well-defined direction would produce a large spatial coherence in the field [20]. Hence, the CDC grating with 5 nm gap and 1D PhC with a cavity length of 200 nm can be considered as a monochromatic thermal source with large temporal coherence at 584 nm wavelength.
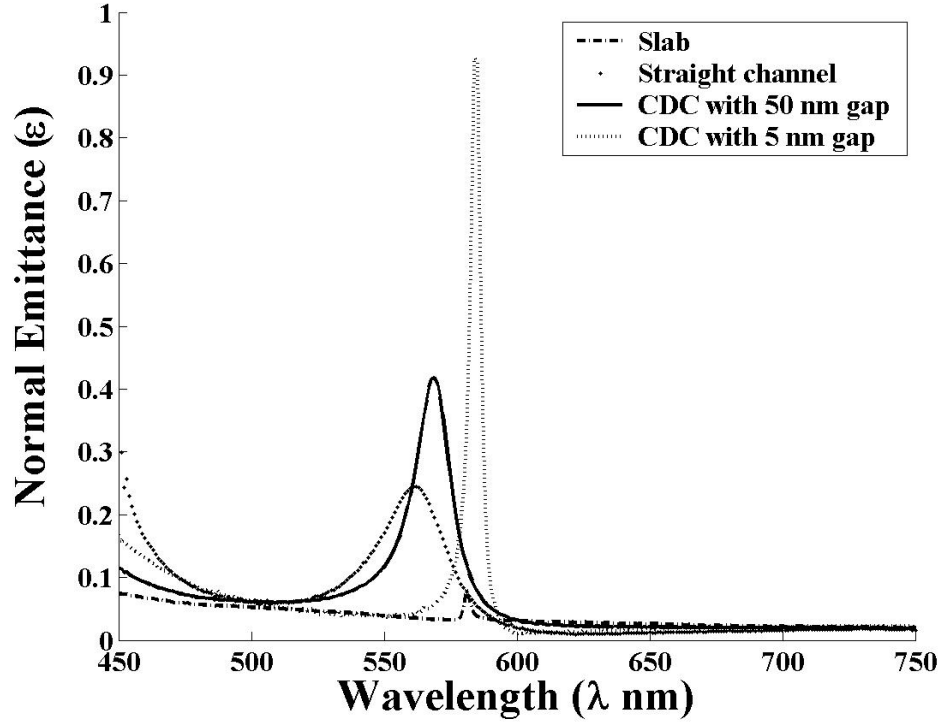
Figure 3.5: Normal emittance spectrum with *p*-polarization in vacuum for different thin Ag film structures having the same grating parameters Λ = 250 nm, h = 100 nm, t = 100 nm and a photonic crystal having the parameters a = 100 nm; $d_1 = d_2$ = 50 nm with cavity length 'L' = 200 nm.

3.4 MONOCHROMATIC POLARIZED EMISSION WITH HIGH TEMPORAL AND LARGE SPATIAL COHERENCE

Figure 3.6 show the *p*-polarized emittance spectrum of the CDC grating with 5 nm gap at the throat and 1D PhC with 500 nm cavity length for different angles of emission. As can be seen from the figures the emission spectrum is very dependent on the angle of observation- the so-called Wolf effect [21, 22]. At a normal angle from Fig. 3.6a, it can be seen that there is a big emission peak in the spectrum at around 591 nm with a

FWHM of about 3 nm. With the angle of emission changed to 34.5$^{\mathrm{o}}$ (Fig. 3.6b), the emittance spectrum has changed and the big emission peak has shifted to a lower wavelength of 525 nm with a FWHM of about 4 nm. Fig. 3.6c shows the emittance spectrum for the 68.5$^{\mathrm{o}}$ angle, with a big emission peak at 595 nm wavelength and a FWHM of about 9 nm. Also there are extremely small peaks in Fig. 3.6c that appear regular and only at wavelengths greater than 600 nm. The transmittance spectrum of the PhC crystal at 68.5$^{\mathrm{o}}$ angle of incidence has regular peaks for wavelengths greater than 600 nm and the spectral locations of the small peaks in the emittance spectrum of Fig. 3.6c are near the PhC transmittance peaks. Hence at the spectral locations where the PhC would have a high transmittance the multi-structure would absorb a very small part of the light that is transmitted by the CDC grating. Thus the emission peaks in Fig 3.6 have very high temporal coherence, which is inversely proportional to the width of the spectral emission peak [20] and is decreasing very little with the increase in angle of emission.

Polarization dependence of the directional emission for the CDC grating with 5 nm gap and 1D PhC with 500 nm cavity length can be seen in Fig 3.7 for different wavelengths. Fig. 3.7a and Fig. 3.7b show the *p*-polarized and *s*-polarized directional emission respectively at the 525 nm wavelength. Fig. 3.7b shows that there is no emission of *s*-polarization near the angles where the emission of *p*-polarization is high. The FWHM for the directional emission peak seen in Fig. 3.7a at around 34.5$^{\mathrm{o}}$ angle from the normal, is around 1.15$^{\mathrm{o}}$ and so, the length of spatial coherence that is given by [23] $L_{coh} = \lambda/(\pi\Delta\theta\cos\theta)$ is approximately 19.5λ, i.e., around 10.5 μm. The length of the multilayer structure (Le) could be around 2.5 μm (with 10 periods of the gratings). This would than have $L_{coh} \gg L_e > \lambda$, making the spatial coherence length of emission at 525

71

nm wavelength extend to a far-field and at the same time polarization dependent. Also from Fig. 3.6b it can be noted that the temporal coherence is very high at 525 nm wavelength and 34.5$^\text{o}$ angle. Therefore the multilayer structure has an almost monochromatic polarization dependent emission with very high temporal coherence and spatial coherence extending into far-field. This kind of emission properties make the proposed multilayer structure emit similarly like a laser, but without a stimulated emission and with a thermally excited emission. Fig. 3.7c-3.7d shows the directional emission of *p*-polarization and *s*-polarization respectively at the 591 nm wavelength. Fig. 3.7d shows that the *s*-polarized emission is again almost negligible near the directional locations where the *p*-polarized emission is high. But, at this wavelength the *p*-polarized directional emission has two peaks in the hemisphere (Fig. 3.7c) and the peak at the normal angle has a FWHM of around 8$^\text{o}$ with L_{coh} ~1.4 μm and this might lead to a local or near-field spatial coherence in normal direction. Whereas, the second peak (at $\theta =$ 68.5$^\text{o}$) has FWHM of around 2.2$^\text{o}$ which gives L_{coh} ~ 14 μm >> L_e > λ, and that would make it a far-field coherent emitter at $\theta = $ 68.5$^\text{o}$. Fig. 3.7e-3.7f shows the *p*-polarized and *s*-polarized directional emission respectively at the 595 nm wavelength. Fig. 3.7f shows that the *s*-polarized emission for the entire hemisphere range is very low at the 595 nm wavelength and *p*-polarized emission is very low in the normal direction (Fig. 3.7e). The directional emission peak for the *p*-polarized directional emission at 595 nm wavelength is at 68.5$^\text{o}$ which is almost at the same angular position of the second directional emission peak for the *p*-polarized emission at 591 nm wavelength. This is consistent with the Fig. 3.6c where the peak of spectral emission is at 595 nm with a FWHM of about 9 nm. The FWHM of the directional emittance peak at 595 nm (Fig. 3.7e) is around 2.1$^\text{o}$ with L_{coh} ~

14 μm >> Le > λ. Therefore from Fig. 3.6a and Fig. 3.7c-3.7d, it can be said that the normal emission of the multilayer structure at 591 nm wavelength is very monochromatic with polarization dependence, large temporal coherence and small spatial coherence length when compared to the length of the structure. However, Fig. 3.6b-3.6c, Fig. 3.7a-3.7b, and Fig. 3.7e - 3.7f shows that the multilayer structure at some specific angles from normal and at 525 nm and 595 nm wavelengths has emittance similar to a laser; very monochromatic with high temporal coherence, polarization dependence and spatial coherence length much larger than the wavelength of emission and the length of the structure.
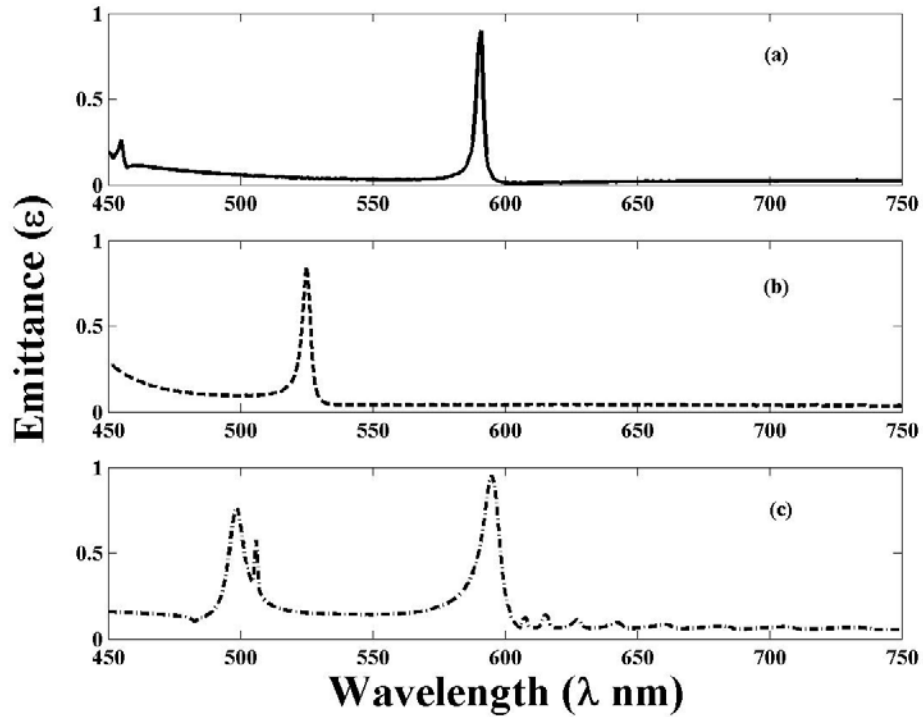
Figure 3.6: Spectral emittance in vacuum with *p*-polarization for Ag CDC grating having the parameters Λ = 250 nm, h = 100 nm, t = 100 nm, g = 5 nm and a photonic crystal having the parameters a = 100 nm; d_1 = d_2 = 50 nm with cavity length L = 500 nm (a) in normal direction θ = 0°, (b) at θ = 34.5° from normal, and (c) θ = 68.5° from normal.
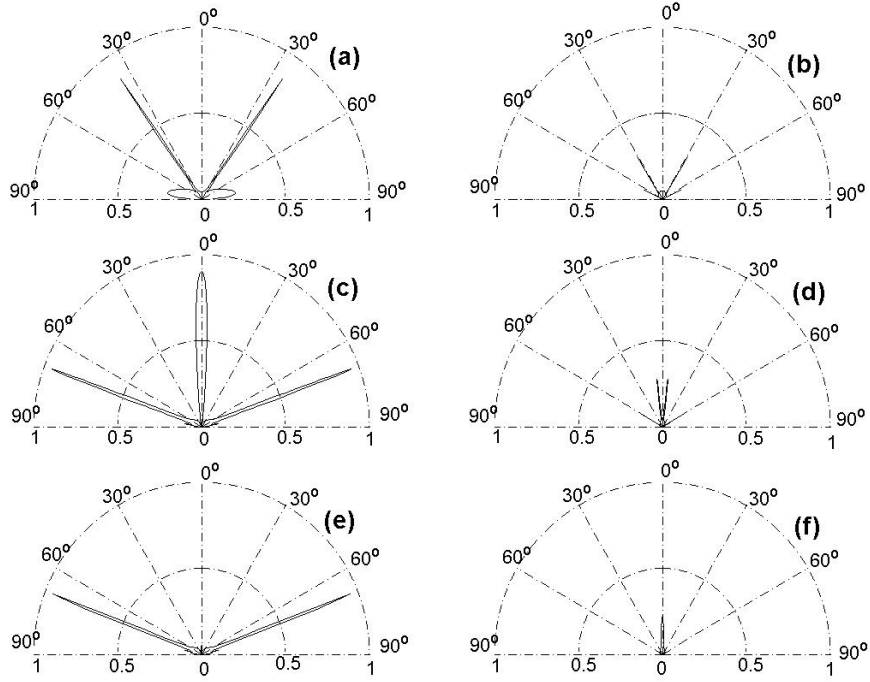
Figure 3.7: Directional emittance in vacuum for Ag CDC grating having the parameters Λ = 250 nm, h = 100 nm, t = 100 nm, g = 5 nm and a photonic crystal having the parameters a = 100 nm; d_1 = d_2 = 50 nm with cavity length L = 500 nm: (a) with *p*-polarization at wavelength 'λ' = 525 nm, (b) with *s*-polarization at wavelength 'λ' = 525 nm, (c) with *p*-polarization at wavelength 'λ' = 591 nm, (d) with *s*-polarization at wavelength 'λ' = 591 nm, (e) with *p*-polarization at wavelength 'λ' = 595 nm, and (f) with *s*-polarization at wavelength 'λ' = 595 nm.

3.5 DEPENDENCE OF EMITTANCE PEAK SPECTRAL POSITION WITH CAVITY LENGTH

Normal emittance spectrum with *p*-polarization for the CDC grating with 5 nm gap and 1D PhC with various cavity lengths can be seen in Fig. 3.8a. The 50 nm cavity length has one smaller emissive peaks at lower wavelength. But, when the cavity length is increased to 100 nm then the emissive peak present at lower wavelength would

74

increase in magnitude and the spectral position of the peak moves to a larger wavelength or has a red shift. When the cavity length further increases to 200 nm then the only emissivity peak in the entire wavelength range of interest will have magnitude almost close to unity and the spectral position of the peak would also have a further red shift. Fig. 3.8a also shows that the cavity length of 300 nm would have a high emissive peak with an additional red shift. The spectrum of normal emittance for the 320 nm cavity length has several narrow peaks towards higher-band wavelength. The FWHM of the emissive peaks for the cavity length of 100 nm and 200 nm are the same and is around 4 nm. For the 300 nm cavity length the FWHM is around 5 nm. Hence Fig. 3.8a shows that varying the cavity length would result in the red shift of the emissive peak and the FWHM of the peaks will be around 4 - 5 nm. This would then suggest that the cavity length is a good degree of freedom for achieving a tunable monochromatic thermal emitter for any desired wavelength. Fig. 3.8b shows the electric field intensity distribution normalized to the incident along a line passing through the center of the CDC grating throat and into the 1D PhC. The intensity variation in the cavity seems to be like a first harmonic standing wave between the Ag grating and 1D PhC. The magnitude of the electric field intensity variation in the cavity increases with the cavity length, suggesting that the increase in emissive peak magnitude is due to the increase in the cavity resonance strength. Also, in 1D PhC the electric field intensity decays within a smaller number of unit cells for larger cavity lengths. Hence Fig. 3.8a-3.8b shows that the high absorption or emission is mainly due to the strong resonance in the cavity and the condition for the resonant wavelength changes with the cavity length.
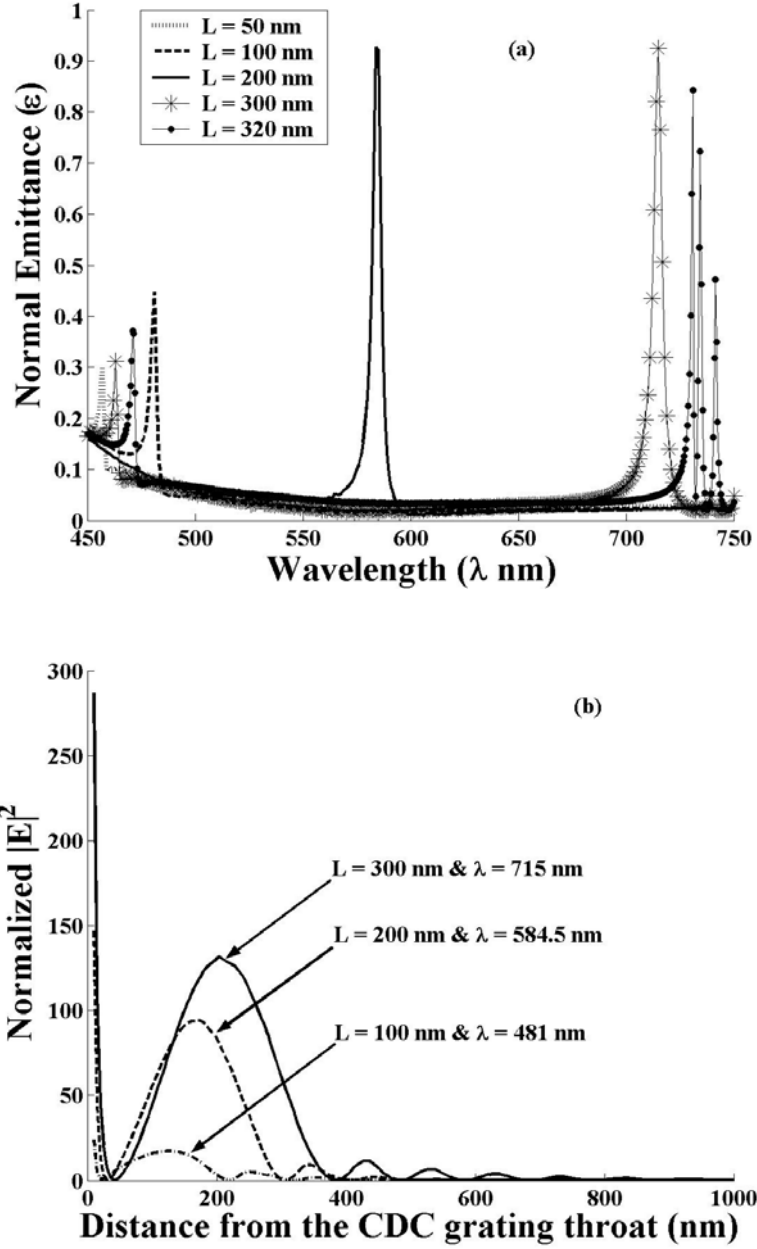
Figure 3.8: (a) Normal emittance spectrum with *p*-polarization in vacuum for Ag CDC grating having the parameters $\Lambda = 250$ nm, h = 100 nm, t = 100 nm, g = 5 nm and a photonic crystal having the parameters a = 100 nm; $d_1 = d_2 = 50$ nm with cavity length L = 50 nm, L = 100 nm, L = 200 nm, L = 300 nm, L = 320 nm, (b) electric field intensity distribution normalized to the incident along the line passing through the center of the CDC grating throat and into the photonic crystal with cavity lengths L = 100 nm, L = 200 nm, L = 300 nm and at respective normal emissive peak wavelengths.

76

For a CDC grating with 5 nm gap at the throat and 1D PhC with an increased cavity length from 320 nm to 350 nm has resulted in reducing the larger peaks present at higher wavelengths, as is evident in Fig. 3.8a and Fig. 3.9a. An additional increase in the cavity length to 400 nm has red shifted the spectral position of the emission peak present at lower wavelengths and also the magnitude of the emissivity peak has increased. In addition, at this cavity length there are no emission peaks near the larger wavelengths. When the cavity length is increased to 500 nm then the emittance peak in the spectrum as shown in Fig. 3.9a, has further red shifted and is almost in the middle of the wavelength range of interest. But, a closer look on the normal emission spectrum in the lower wavelength range shows that there is a very small peak in the emission indicating that there could be an onset of even higher resonance in the cavity, as shown later. With the cavity length increased to 600 nm the larger emission peak in the spectrum has further red shifted and the smaller emission peak has gained in strength with a similar red shift. But the normal emittance spectrum, for the cavity length of 690 nm has multiple emission peaks at higher wavelengths and the emission peak at the lower wavelength has gained further in the magnitude with all of the emission peaks having red shift. Fig. 3.9b shows the electric field intensity distribution normalized to the incident along the line passing through the center of the CDC throat and into the 1D PhC, at the spectral positions where the emission spectrum has large peaks for the cavity lengths of 350 nm, 400 nm, 500 nm and 600 nm. From the figure it can be seen that for all the cavity lengths considered the resonance in the cavity is similar to a second harmonic resonance of a standing wave. Therefore as the cavity length increases the spectral position of the emission peak due to the second harmonic resonance would have red shift, as observed similarly for the first

77

harmonic resonance in Fig. 3.8a-3.8b. When the cavity lengths increase beyond a certain range, then there would be an onset of higher order resonances at lower wavelengths and this is shown in Fig. 3.9c. In this figure the normalized electric field intensity distribution is shown along the same line as the previous cases but for wavelengths where the spectral emission has peaks in the lower wavelength. The intensity distribution shows that the cavity has a resonance that is similar to a third harmonic standing wave.

Figure 3.10 shows the variation of the normal emission peaks with respect to the change in cavity length for different resonances. The first resonance or the first harmonic is due to half standing wave in the cavity as shown in Fig. 3.8b. The second resonance or the second harmonic is due to a complete standing wave in the cavity as shown in Fig. 3.9b. The variation in the spectral position of the emission peaks with the change in cavity length seems to be almost linear for both the resonances except at the band-edge wavelengths of the 1D PhC. In addition the first resonance emission peaks needs a smaller cavity length range or a higher slope to span the entire wavelength range of interest when compared to the second resonance emission peaks that needs a larger cavity length range or lower slope for the same wavelength range.
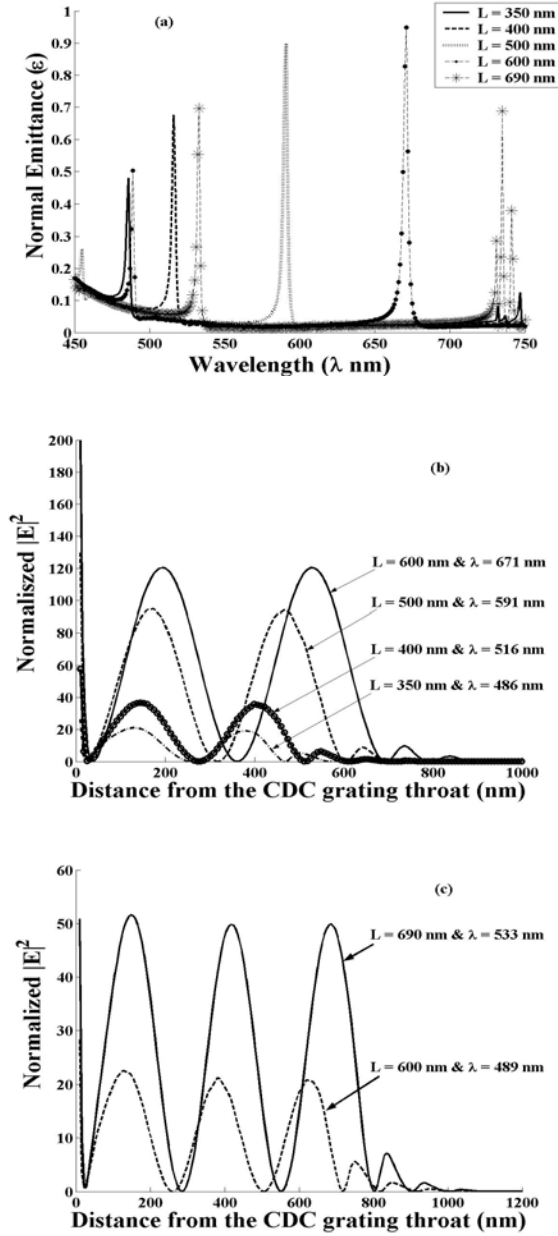
Figure 3.9: (a) Normal emittance spectrum with *p*-polarization in vacuum for Ag CDC grating having the parameters $\Lambda = 250$ nm, h = 100 nm, t = 100 nm, g = 5 nm and a photonic crystal having the parameters a = 100 nm; $d_1 = d_2 = 50$ nm with varying cavity. Electric field intensity distribution normalized to the incident along the line passing through the center of the CDC grating throat and into the photonic crystal with (b) L = 350 nm, L = 400 nm, L = 500 nm, L = 600 nm, and at respective higher normal emissive peak wavelengths (c) L = 600 nm, L = 690 nm and at respective lower normal emissive peak wavelengths.
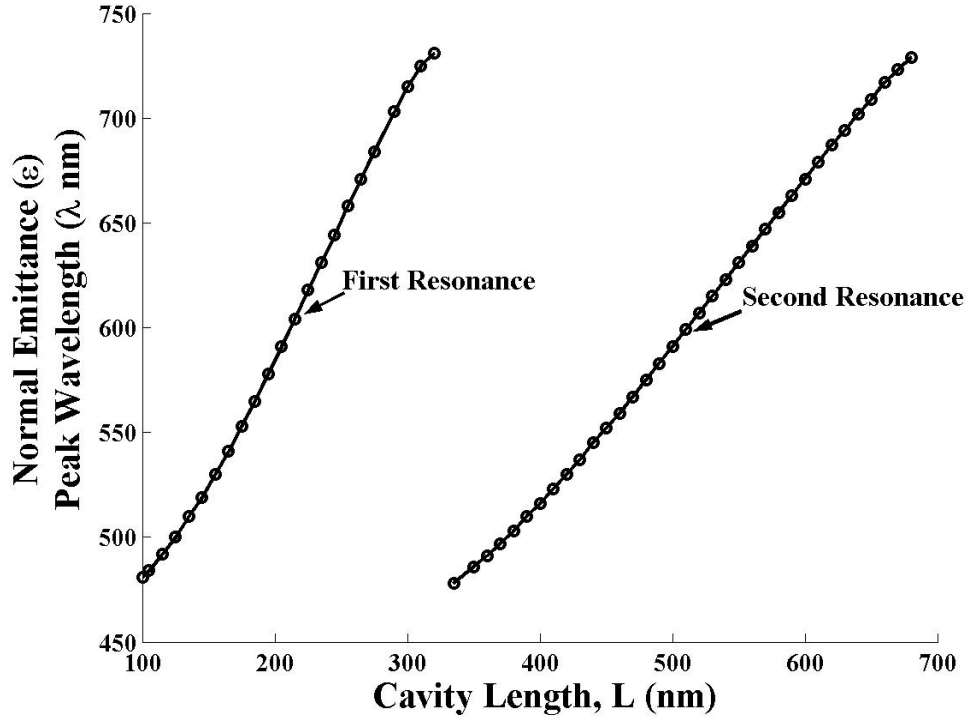
Figure 3.10: Variation of the normal emittance peak wavelength with respect to the cavity length for Ag CDC grating having the parameters $\Lambda = 250$ nm, h = 100 nm, t = 100 nm, g = 5 nm and a photonic crystal having the parameters a = 100 nm; $d_1 = d_2 = 50$ nm.

3.4 CONCLUSION

It has been shown that a unique thermal emitter in visible range could be constructed by having a cavity surrounded on one side by a thin CDC Ag grating and a 1D PhC on the other side. The design concept described can be extended to various wavelength ranges of interest. The emission properties of the proposed thermal emitter are highly monochromatic (FWHM ~ 4 nm) with large temporal coherence, extremely directional (FWHM ~ 1.15°) with far field spatial coherence and is *p*-polarized. The

narrow peaks in the spectral and directional emission are mainly due to the strong resonances in the cavity supported by the Ag CDC grating and 1D PhC. The thermal source is tunable to various wavelengths and directions of emission with the choice of right materials along with the parameters of the grating, cavity length and 1D PhC. Thus, the CDC grating and 1D PhC with a cavity offers a simple multilayer structure that could have great implications in a variety of applications with diverse wavelength range of interest. Also the present thermal emitter with varying cavity length can be used as a single light source for different colors which could make it an ideal fluorophores for sensitive, multicolor and multiplexing applications in molecular biology and bioengineering.

Reference

[1]. R. Carminati, J. J. Greffet, "Near-field effects in spatial coherence of thermal sources", *Physical Review Letters*, **82**, 1660-1663 (1999).
[2]. C. Henkel, K. Joulain, R. Carminati, J. J. Greffet, "Spatial coherence of thermal near fields", *Optics Communications*, **186**, 57-67 (2000).
[3]. A. V. Shchegrov, K. Joulain, R. Carminati, J. J. Greffet, "Near-field spectral effects due to electromagnetic surface excitations", *Physical Review Letters*, **85**, 1548-1551 (2000).
[4]. P. J. Hesketh, J. N. Zemel, B. Gebhart, "Organ Pipe Radiant Modes of Periodic Micromachined Silicon Surfaces", *Nature*, **324**, 549-551 (1986).
[5]. E. A. Vinogradov, G. N. Zhizhin, A. G. Malshukov, V. I. Yudson, "Thermostimulated Polariton Emission of Zinc Selenide Films on Metal-Substrate", *Solid State Communications*, **23**, 915-921 (1977).
[6]. M. Kreiter, J. Oster, R. Sambles, S. Herminghaus, S. Mittler-Neher, W. Knoll, "Thermally induced emission of light from a metallic diffraction grating, mediated by surface plasmons", *Optics Communications*, **168**, 117-122 (1999).
[7]. J. J. Greffet, R. Carminati, K. Joulain, J. P. Mulet, S. P. Mainguy, Y. Chen, "Coherent emission of light by thermal sources", *Nature*, **416**, 61-64 (2002).
[8]. P. Ben-Abdallah, "Thermal antenna behavior for thin-film structures", *Journal of the Optical Society of America a-Optics Image Science and Vision*, **21**, 1368-1371 (2004).
[9]. B. J. Lee, C. J. Fu, Z. M. Zhang, "Coherent thermal emission from one-dimensional photonic crystals", *Applied Physics Letters*, **87**, - (2005).

[10]. A. Narayanaswamy, G. Chen, "Thermal emission control with one-dimensional metallodielectric photonic crystals", *Physical Review B*, **70**, - (2004).

[11]. I. Celanovic, D. Perreault, J. Kassakian, "Resonant-cavity enhanced thermal emission", *Physical Review B*, **72**, - (2005).

[12]. H. Sai, H. Yugami, Y. Akiyama, Y. Kanamori, K. Hane, "Spectral control of thermal emission by periodic microstructured surfaces in the near-infrared region", *Journal of the Optical Society of America a-Optics Image Science and Vision*, **18**, 1471-1476 (2001).

[13]. A. Heinzel, V. Boerner, A. Gombert, B. Blasi, V. Wittwer, J. Luther, "Radiation filters and emitters for the NIR based on periodically structured metal surfaces", *Journal of Modern Optics*, **47**, 2399-2419 (2000).

[14]. M. Laroche, R. Carminati, J. J. Greffet, "Coherent thermal antenna using a photonic crystal slab", *Physical Review Letters*, **96**, - (2006).

[15]. S. Y. Lin, J. Moreno, J. G. Fleming, "Three-dimensional photonic-crystal emitter for thermal photovoltaic power generation", *Applied Physics Letters*, **83**, 380-382 (2003).

[16]. J. G. Fleming, S. Y. Lin, I. El-Kady, R. Biswas, K. M. Ho, "All-metallic three-dimensional photonic crystals with a large infrared bandgap", *Nature*, **417**, 52-55 (2002).

[17]. J. J. Greffet, M. Nieto-Vesperinas, "Field theory for generalized bidirectional reflectivity: derivation of Helmholtz's reciprocity principle and Kirchhoff's law", *Journal of the Optical Society of America a-Optics Image Science and Vision*, **15**, 2735-2744 (1998).

[18]. E. D. Palik, Ed., *Handbook of optical constants of solids* (Academic Press, Orlando, 1985).

[19]. A. Lavrinenko, P. I. Borel, L. H. Frandsen, M. Thorhauge, A. Harpoth, M. Kristensen, T. Niemi, H. M. H. Chong, "Comprehensive FDTD modelling of photonic crystal waveguide components", *Optics Express*, **12**, 234-248 (2004).

[20]. J. LeGall, M. Olivier, J. J. Greffet, "Experimental and theoretical study of reflection and coherent thermal emission by a SiC grating supporting a surface-phonon polariton", *Physical Review B*, **55**, 10105-10114 (1997).

[21]. E. Wolf, "Non-Cosmological Redshifts of Spectral-Lines", *Nature*, **326**, 363-365 (1987).

[22]. E. Wolf, D. F. V. James, "Correlation-induced spectral changes", *Reports on Progress in Physics*, **59**, 771-818 (1996).

[23]. F. Marquier, K. Joulain, J. P. Mulet, R. Carminati, J. J. Greffet, Y. Chen, "Coherent spontaneous emission of light by thermal sources", *Physical Review B*, **69**, - (2004).

Chapter 4: Tunable plasmonic-crystal superlens for subwavelength imaging

4.1 INTRODUCTION

Traditional optical lenses have curved surfaces that focus light by virtue of the refractive index contrast, but cannot focus light onto an area smaller than a wavelength square. But, few decades ago it was predicted that an isotropic medium with simultaneously negative electrical permittivity (ε) and magnetic permeability (μ) could display unique electromagnetic (EM) properties with "negative" index of refraction which can be utilized for producing an image smaller than the wavelength. However, naturally occurring materials are not negative index materials (NIM) and so specially engineered NIM called metamaterials have been proposed [1-4]. These metamaterials nonetheless have a high probability where an unwanted resonance could hinder 'ε' and 'μ' to be simultaneously negative in a frequency range [5]. An interesting alternative to the metamaterials could be the photonic crystal (PhC), which under proper conditions can act as a homogeneous medium with a negative index. The physical principle that allows negative refraction (NR) in PhC is dependent on the dispersion characteristics of the wave propagation in the PhC. Here we report a hybrid photonic crystal (HPhC), where the polaritonic mode of a metallic array can be combined with the photonic mode of a hole array in a dielectric slab for achieving NR and still posses an extra degree of freedom for tuning the HPhC as a superlens to operate at different frequencies. We numerically demonstrate that a single planar HPhC structure can indeed be used for subwavelength imaging at different frequencies by just varying the optical properties in

83

the hole array, thereby enabling the realization of ultracompact tunable superlens and paving the way for a new class of optical lens.

Recently a "planar superlens" was proposed with a thin negative index film that can provide image details with a resolution beyond the diffraction limit [6]. The planar superlens would aid the evanescent wave, which carries the finest details, from the object to grow inside the slab and when exited the lens slab would have the same amplitude at the image plane with which it started. Hence, the resolution limit of the planar superlens is determined by the number of evanescent waves from the object that have been recovered and not by the diffraction limit [5]. Similarly, metamaterials can restore not only the phase of the propagation waves but also the evanescent waves of the object. Metamaterials are achieved by having a medium made of conducting wires that would give negative 'ε' and various current loops that would give negative 'μ' in the same frequency band. The negative index of refraction is then determined by using an effective medium theory. But, this would require the operating wavelength to be much larger than the size of the unit cell. Hence, it would be difficult to build a metamaterial device that can operate at very small wavelength. One of the first NIM was constructed using copper split-ring resonators (SRR) and copper wire strips [1-4]. These SRR structures have been recently scaled down to produce metamaterials active in terahertz frequency [5].

An interesting alternative to the metamaterials could be the photonic crystal (PhC), which under proper conditions can act as a homogeneous medium with a negative index. The dispersion in a PhC can be described by the equifreqeucny surface (EFS) of the band structures of the PhC [7]. A two-dimensional (2D) polaritonic crystal (PLC) made of metallic units was proposed to achieve the superlensing effect at visible

frequencies. The metallic units support plasma mode which would interfere with photon and lead to plasmon polariton that would then modify the photon dispersion to highly symmetric concave and convex polaritonic bands ideal for superlensing [8]. All-angle NR (AANR) was achieved at the lowest band of 2D PhC, consisting of a square lattice of air holes in Si and the subwavelength image formed is in the near-field of PhC [9]. It was observed by [10] that the near-field subwavelength imaging is mainly due to the self-collimation effect and near-field scattering, apart from the NR effect that might also take place. Nevertheless, far-field imaging and focusing has been achieved in the lowest (or valence) band for a 2D square lattice of dielectric coated metallic core cylinders immersed in air background [7]. Also, surface termination within a specific cut of the triangular array of dielectric bars would excite surface waves at the interference between air and a triangular array of dielectric bar PhC which would allow the reconstruction of evanescent waves for a better focus and transmission [11]. Therefore a 2D PhC slab, which is made from the periodic arrays of either dielectric or metallic building blocks, with a lattice constant comparable with the wavelength, can be used as a superlens slab for an image construction.

Optical systems that are synthesized by using fluids are called optofluidics. The key advantage of fluid over a solid is the ability to change the optical property of the fluid medium within an optical device by simply replacing one fluid with another. A number of microfluidic devices based on PhC have been reported. One such PhC sensing device is based on a high-Q cavity resonance shift due the various analytes in the cavity [12]. Recently it was also reported that by introducing coupled defects into the PhC waveguide, the sensing of biomaterials like DNA which fills the defects, was made

possible by measuring the associated changes in the transmission of the PhC [13, 14]. Thus micro/nano-fluidics provide a solution that enables both localized or global control of high refractive index modulation for tuning the optical systems.

4.2 SCHEMATIC VIEW OF THE PLASMONIC CRYSTAL AND COMPUTATIONAL SET-UP

In the current study a 2D tunable plasmonic crystal (2D tPLC) is proposed and it has a triangular array of metallic cylinders in a Si ($\varepsilon = 12$) substrate with graphene array of holes as shown in the inset of Fig. 4.1(a). The lattice constant of the metallic cylinders is 'a', whereas the lattice constant of the holes is '$a/\sqrt{3}$'. The NR and superlensing effect of the 2D tPLC is demonstrated in the infrared (IR) range (1.4 ~ 1.65 μm). In addition it will also be shown that the present tPLC would behave like a homogeneous medium with an effective refractive index (n_{eff}) approximately '-1' for different frequencies and the imaging mechanism would follow the well-known wave-beam geometric optics. The holes in 2D tPLC can be filled with different organic liquids to have various dielectric constants that would subsequently shift the frequency range for NR. The present study has considered the holes to be filled with either air ($\varepsilon = 1$) or tetrachloromethane (CCl$_4$; $\varepsilon = 2.2379$) or dichloroethane (C$_2$H$_4$Cl$_2$; $\varepsilon = 10.10$). Electromagnetic response (ε) of the metallic cylinder is assumed to be dispersive in IR and is described by a free-electron model given by

$$\varepsilon(\omega) = 1 - \left(\frac{\omega_p}{\omega}\right)^2, \quad \omega_p = N\frac{2\pi c}{a} \tag{4.1}$$

where, 'ω' is the frequency and 'ω_p' is the plasma frequency as defined above; with N = 2.5, 'c' is the speed of light and 'a' is the lattice constant. The metallic

86

cylinders considered have a radius (r_a) of 0.3a and the holes have a radius (r_b) of 0.2a. By choosing the lattice constant a to be 375 nm, then the ω_p would be 1.25 x 10^{16}, close to the plasma frequency of gold in IR. The dielectric response of gold in IR would have an imaginary part that is two orders of magnitude lower then the real part and so the free-electron model can be used for predicting the imaging mechanism. The imaging characteristics with low absorption would not change except for the full-width at half maximum (FWHM) of the intensity near the image plane which might increase by a small extent [7, 8] and this will also be explored for comparison.

In the present study we consider only transverse electric (TE) mode (in-plane electric field; x-y) propagation bands in the 2D tPLC, since for the transverse magnetic (TM) mode we found no superlensing effect. The metallic cylinders and the holes in 2D tPLC are considered to be infinitely extended in the z-direction. The non-vanishing EM field components are H_z, E_x, and E_y. TE mode propagation bands can be obtained by solving the following nonlinear eigenvalue equation for H_z.

$$-\vec{\nabla} \cdot \left(\frac{1}{\varepsilon(\omega,\vec{r})} \vec{\nabla} H_z \right) = \left(\frac{\omega}{c} \right)^2 H_z \tag{4.2}$$

where, H_z satisfies the phase-shifted periodic boundary condition as given by $H_z(\vec{r}+\vec{a}) = H_z(\vec{r})e^{ik\vec{r}}$ (as described in the following equations), with $\vec{a}$ as a vector connecting the opposite edges of the unit cell (Fig. 4.1b), and $\vec{k}$ as a Bloch wave number that belongs to the irreducible Brillouin zone [15]. Solving the eq. (4.2) by an iterative process gives the dispersion relation 'ω' versus '$\vec{k}$' or the photonic band structure. For

numerical calculations we used commercially available finite element software (COMSOL 3.2a).

$$k_x = l_x \frac{2\pi}{3}$$

$$k_y = l_y \frac{2\pi}{\sqrt{3}}$$

$$C_x = k_x \qquad\qquad\qquad (4.3)$$

$$C_y = k_x \sin\left(\frac{\pi}{6}\right) + k_y \cos\left(\frac{\pi}{6}\right)$$

$$H_{z,3} = H_{z,1} e^{iC_x}$$

$$H_{z,4} = H_{z,2} e^{iC_y}$$
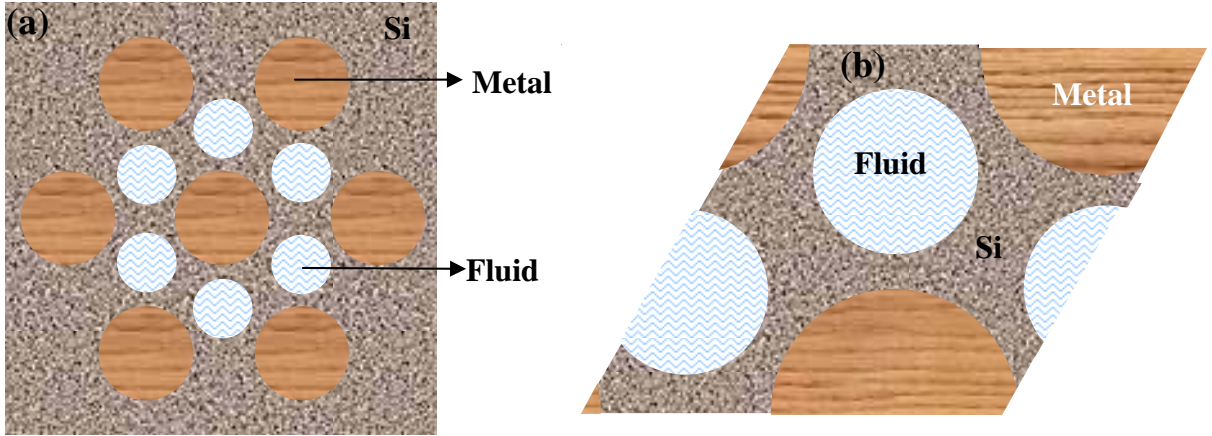
Figure 4.1: (a) Schematic figure of 2D triangular array of infinitely long metallic cylinder and holes imbedded in a host material Si. (b) Unit cell of the hybrid photonic crystal.

Figure 4.2 shows the dispersion characteristics of a 2D PhC consisting of air holes with diameter '0.8*a*' in silicon ($\varepsilon = 12.0$) arranged in hexagonal or triangular lattice. Fig 4.2a and Fig. 4.2c are the results obtained by [16]. Whereas, the results for the same 2D PhC using the present study numerical model is obtained and is shown in Fig. 4.2b and Fig. 4.2d respectively. From Fig. 4.2 it can be clearly observed that the numerical model used is valid and predicts the correct results that can be obtained by other techniques.
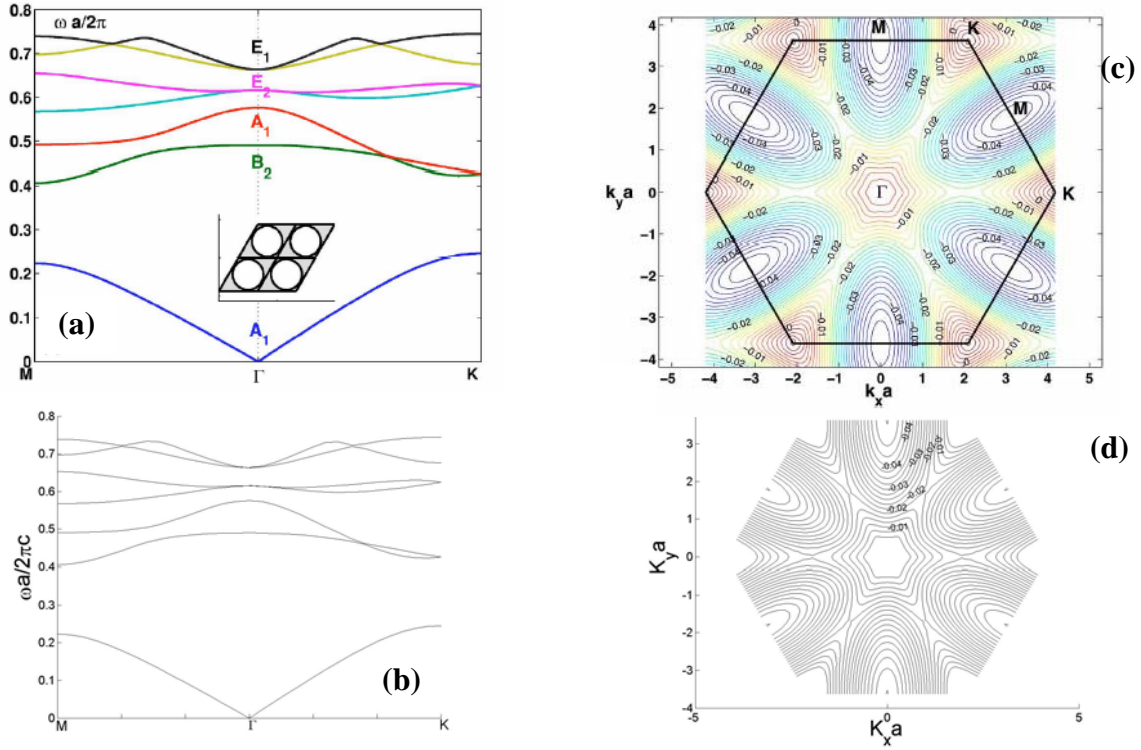
Figure 4.2: (a) TE mode propagation modes $\omega(\vec{k})$ for the PhC consisting of air holes in silicon [16], and (b) Band structure for the same PhC obtained by the present study numerical model. (c) Equifrequency surface (EFS) for the lower frequency band of the PhC [16], and (d) EFS for the same PhC obtained by using the present study numerical model.

4.3 BANDSTRUCTURE AND NORMALIZED EQUIFREQUENCY SURFACES

Figure 4.3a. shows the TE mode propagation band structure for the 2D tPLC with holes filled by different fluids. The quantity 'ωa/2πc' is a normalized or dimensionless frequency (Ω). For when the holes are filled with air, there is complete photonic bandgap between the second and third bands, i.e., between the normalized frequency range of 0.31 ~ 0.41. The second band has a convex shape around Γ point which would give a homogeneous NR in the PhC [7, 8]. Even with the holes filled by CCl_4 the band structure would be similar to the previous except that complete bandgap is now between Ω range of 0.305 ~ 0.37 and the second band would still have a convex shape around Γ point. By changing the fluid in the hole to an even higher dielectric constant, like with $C_2H_4Cl_2$, the band structure would then have a change in the band structure with the complete bandgap now between the third and fourth band within the Ω range of 0.275 ~ 0.285. But the second band is still convex around the Γ point. Hence by changing the fluids in the hole of 2D tPLC we can tune the band structure and subsequently the structure could be used at different desired frequency ranges. Fig. 4.3b shows the EFS for the second band of the 2D tPLC with the holes filled by air. EFS, basically consists of allowed propagation modes within the Brillouin zone (BZ) of PhC at a specific frequency. Most of the frequency contours in Fig. 4.3b are isotropic with circles having a center around the Γ point. Thus when a plane wave is incident from vacuum onto the present PhC, the refracted angle would be linearly proportional to the incident angle. This would then help to have far-field images when the PhC medium also has negative index. For every chosen wavevector ($\vec{k}$), the corresponding group velocity ($\vec{v}_g$) will be normal to the EFS at that

point and is directed towards the increasing frequency. Hence $\vec{v}_g$ at any point on circular

EFS contour is collimated with $\vec{k}$, indicating that the PhC slab medium behaves like an

effective homogeneous medium. Fig. 4.3b shows that a Ω region of the second band

extending from 0.225 to 0.305 has EFS contours that are moving inward with increasing

frequency. This would then result in $\vec{v}_g \cdot \vec{k} < 0$. It has been shown analytically that for an

infinite PhC system $\vec{v}_g$ coincides with the energy velocity $\left(\vec{S} \right)$ [17]. Hence the sign of

$\vec{v}_g \cdot \vec{k} < 0$ is equivalent to the sign of $\vec{S} \cdot \vec{k} < 0$, which is of particular necessity for a left-

handed material (LHM) [18]. In a LHM the $\vec{k}$, $\vec{E}$ and $\vec{H}$ form a left-handed set of

vectors which would then can give NR. Therefore the 2D tPLC with the holes filled by

air can be considered as a homogeneous medium with effective negative index of

refraction in the Ω range from 0.225 to 0.305. Similarly, Fig. 4.3c shows that the EFS

contours of the second band for 2D tPLC with holes filled by CCl$_4$ is the same as the

previous case except that $\vec{S} \cdot \vec{k} < 0$ is happening in a different Ω region (0.215 - 0.30).

When the holes are filled by an even higher dielectric constant of C$_2$H$_4$Cl$_2$ the EFS

contours of the second band are still circular shapes (Fig. 4.3d). This time $\vec{S} \cdot \vec{k} < 0$

happens in a lower Ω ranging from 0.175 to 0.27. The Ω range in which $\vec{S} \cdot \vec{k} < 0$ will be

where the superlensing effect can be achieved. In addition, the refracted propagating

modes are determined by the conservation of frequency and parallel wave-vector near the

air and PhC interface. Therefore for a 2D tPLC planar slab with the surface normal along

the ΓM direction of the BZ and with the convex EFS contours everywhere, the incoming

wave from the air would couple to a single propagating mode of the PhC and onto the

negative side of the normal. This could than can be realized as NR for superlensing effect with a far-field imaging.

The main challenge for perfect superlensing is to find a structure with a matching condition that could have $n_{eff} \sim -1$, which will then have no reflections during the imaging process [11]. Fig. 4.4 shows the n_{eff} variation with respect to Ω along two different propagation directions of ΓM and ΓK in the BZ of the 2D tPLC for various fluids filling the holes. The n_{eff} for each fluid in the hole is same in both ΓM and ΓK directions for most of their respective second band frequency range. This would further justify that the 2D tPLC under study is an isotropic medium with $n_{eff} < 0$ for a wide frequency range. Also it can be noted from Fig. 4.4 is that at a particular Ω the n_{eff} can be tuned to different negative values by just varying the dielectric constant in the holes, i.e., by varying the fluids in the holes. Moreover for tuning the PhC to different Ω at a particular n_{eff}, we could achieve it again by simply changing the optical property in the holes. The n_{eff} is approximately '-1' for the present 2D tPLC with holes filled by air at $\Omega = 0.275$. Whereas, for CCl_4 it is at $\Omega = 0.2675$ and for $C_2H_4Cl_2$ it is at $\Omega = 0.23$.
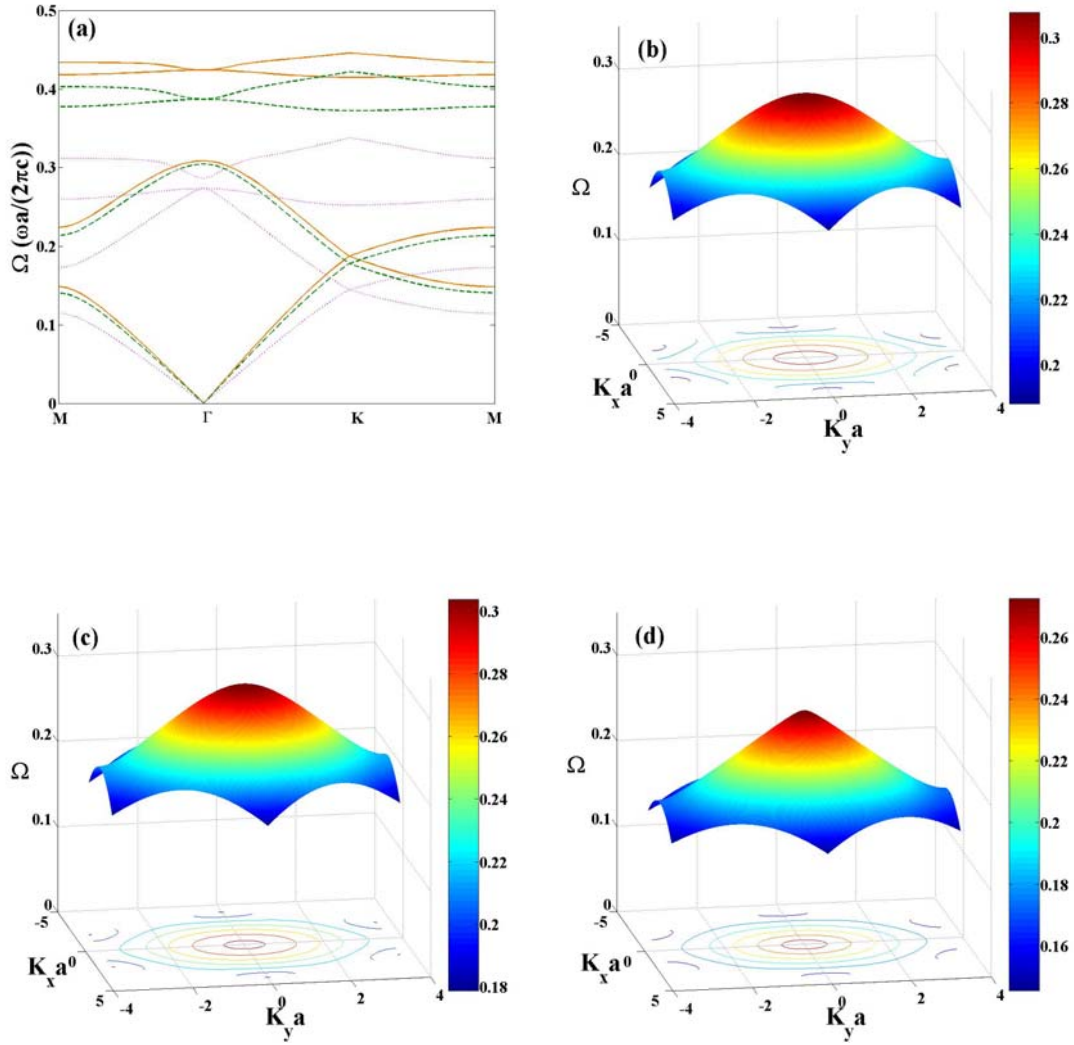
Figure 4.3: (a) TE mode propagation bands for a 2D plasmonic crystal consisting of triangular array of metallic cylinders ($r_a = 0.3a$) having a lattice constant 'a' imbedded in Si ($\varepsilon = 12$) substrate having triangular array of holes ($r_b = 0.2a$) having a lattice constant '$a/\sqrt{3}$' filled by air (solid lines), tetrachloromethane (dashed line) and dichloroethane (dashed dot line). Normalized equifrequecny surfaces (EFS) in the irreducible Brillouin zone for the second band with TE mode of the 2D plasmonic crystal with the holes filled by (b) air, (c) tetrachloromethane and (d) dichloroethane.
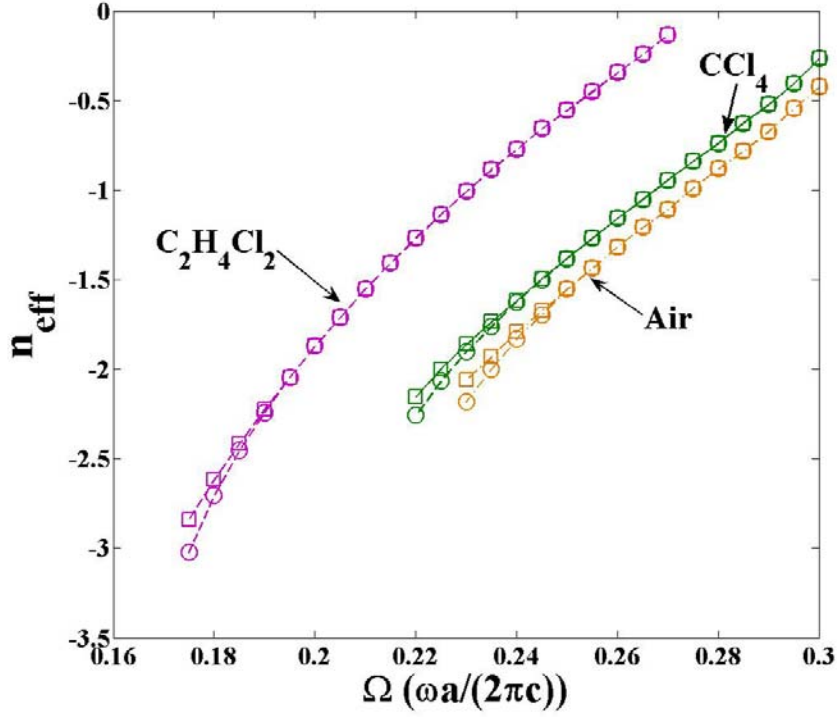
Figure 4.4: Effective refractive index (n_{eff}) of a 2D plasmonic crystal, consisting of triangular array of metallic cylinders (r_a = 0.3a) having a lattice constant '*a*' imbedded in Si (ε = 12) substrate having triangular array of holes (r_b = 0.2a) having a lattice constant '$a/\sqrt{3}$', for the second band in ΓM (circles) and ΓK (square) directions of propagation with the holes of the plasmonic crystal filled by air (dashed dot line), tetrachloromethane (solid line) and dichloroethane (dashed line).

4.4 MAGNETIC FIELD INTENSITY PLOTS OF SOURCE AND IMAGE

A typical H_z field distribution across the planar 2D tPLC with two different optical properties in the holes is plotted in Fig. 4.5 for a source having diameter '*a*' and is at two different distances 'd'. The H_z field pattern shown is over a 40*a* x 29*a* region around the center of the planar PhC slab. The geometry of 2D tPLC is also displayed for

94

clarity of the PhC view. Fig. 4.5a shows the H_z pattern across the planar PhC slab with holes filled by air for a source placed on top of the slab at d = $2a$ and is at $\Omega = 0.27$, for which the PhC has $n_{eff} \approx -1$ (Fig. 4.4). A high quality image on the opposite side of the PhC slab is observed (Fig. 4.5a) along with the focusing region in the middle of the slab which is in accordance to the wave-beam geometric optics. The rays diverging from the source would negatively refract at the first surface of the slab and converge at a point within the slab. The rays would then diverge from the focus region in the slab and then negatively refract again at the second surface of the slab to converge and form a second image outside the slab. The planar superlens slab does not have an optical axis and so posses a key advantage over the conventional lenses by not requiring strict alignment and also can be operated over distances on the order of wavelength. In order to further clarify whether the superlensing effect of the present 2D tPLC slab is in accordance to the geometric optics, the dependence of image and focusing distance inside the PhC slab on source distance is also explored. Fig. 4.5b shows the H_z field pattern for the same conditions as in Fig. 4.5a except that now the source is very close to the PhC slab (d = $0.55a$) and it can be observed that the image has shifted further away from the PhC slab which is in accordance to the geometric optics. Also, the focusing region inside the PhC slab moves to the top surface of the slab as the source moves close to the PhC slab surface, which is also in agreement with the geometric optics. The FWHM of magnetic field intensity at the image plane in Fig. 4.5a is 0.38λ and in Fig. 4.5b is 0.37λ. Therefore, at $\Omega = 0.27$, the 2D tPLC with air in the holes can be considered as a homogeneous LHM for superlensing effect with sub-wavelength imaging (Fig. 4.3b, Fig. 4.4 and Fig. 4.5a-

95

4.5b). Fig. 4.5c and Fig. 4.5d shows the H_z field pattern for a 2D tPLC with holes filled by CCl_4 for a source with $\Omega = 0.26$ ($n_{eff} \approx -1$, Fig. 4.4), but placed at d = 2a and d = 0.55a respectively. Even with higher dielectric constant fluid, like CCl_4, in the holes of PhC slab the superlensing effect follows the geometric optics, but it happens at a frequency different from the PhC with holes filled by air. The FWHM of the image in Fig. 4.5c is 0.42λ and in Fig. 4.5d is 0.41λ.

Figure 4.6a-4.6b shows the snapshots of H_z field pattern across a planar 2D tPLC slab with the holes filled by $C_2H_4Cl_2$ along with a source having $\Omega = 0.23$ ($n_{eff} \approx -1$, Fig. 4.4) and at various distances. Fig. 4.6a, Fig. 4.6b and Fig. 4.6c are for sources placed at distances 4a, 2a and 0.55a from the top of the slab respectively. Just as expected it can be observed from the figures that with a change in the source distance from the slab, the image distance changes too, which is in accordance with the geometric optics. The FWHM of the images in Fig. 4.6a is 0.41λ, in Fig. 4.6b is 0.40λ and in Fig. 4.6c is 0.39λ. In addition Fig. 4.6b and Fig. 4.6c show the existence of surface waves (alternate blue and yellow spikes) or surface plasmons (SPs) on the top surface of the slab. Hence for the proposed 2D tPLC apart from the NR dispersion characteristics, the SPs also play a role for superlensing effect. However it is to be noted that the existence of the SPs on the top surface is evident only when the holes of the PhC slab are filled with a higher dielectric constant fluid like $C_2H_4Cl_2$.
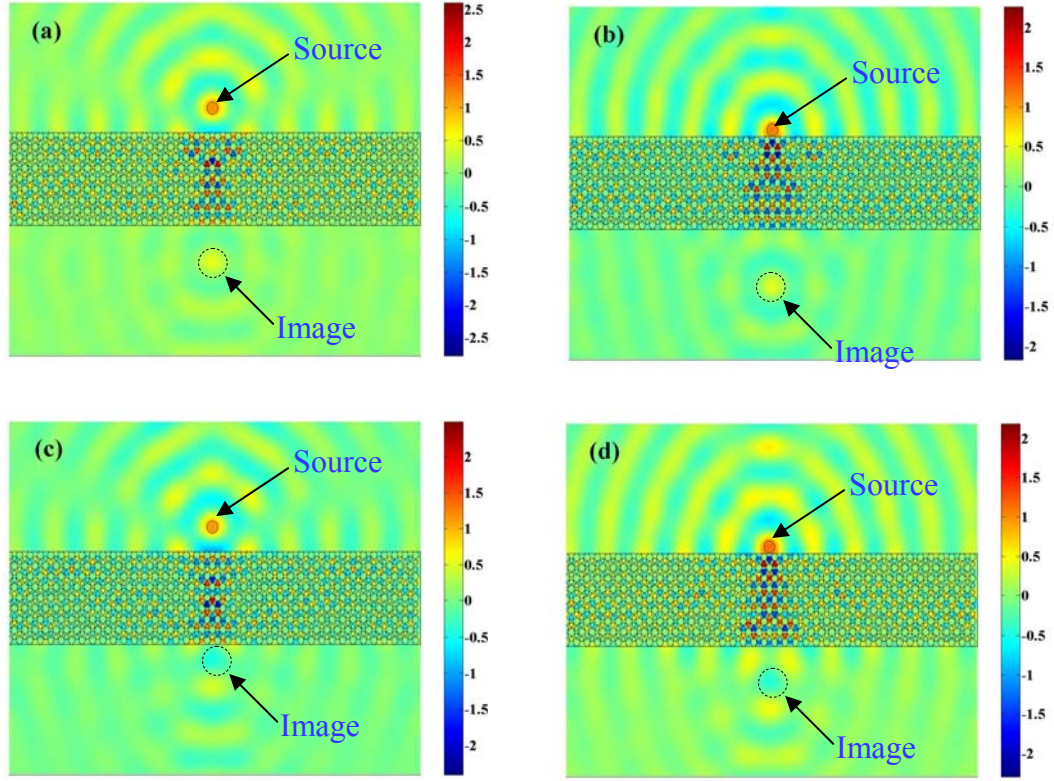
Figure 4.5: Snapshot of the H_z field produced by a point source and its image across a 2D plasmonic crystal slab with normal of the slab surface in ΓM direction of the Brillouin zone. The plasmonic crystal consists of a triangular array of metallic cylinders ($r_a = 0.3a$) having a lattice constant 'a' imbedded in Si ($\varepsilon = 12$) substrate having triangular array of holes ($r_b = 0.2a$) having a lattice constant '$a/\sqrt{3}$'. The source is placed on top of the slab at a distance (a) d = 2a, (b) d = 0.55a with the holes filled by air and at normalized frequency Ω = 0.27; (c) d = 2a, (d) d = 0.55a with the holes filled by tetrachloromethane and at Ω = 0.26.

In order to clarify the good quality of the image it is better to plot the intensity profile at the image plane and compare the FWHM of intensity plot with the object diameter. Fig. 4.7 shows the normalized intensity versus the lateral direction at the image plane with the holes filled by air (a), CCl_4 (b) and $C_2H_4Cl_2$ (c). Fig. 4.7a shows the image intensity plots for a source with $\Omega = 0.27$ (or wavelength, $\lambda = a/\Omega \approx 1.4$ μm) and placed at $d = 2a$ from the top surface of planar PhC slab for when the cylinder in the PhC is either a free electron model metal or gold having an absorption with a real dielectric constant [19]. The object diameter is 'a' which in terms of the source wavelength is 0.27λ. The FWHM in Fig. 4.7a for both free electron model metal and gold is 0.38λ. Whereas, for a PhC with holes filled by CCl_4, Fig. 4.7b shows that for a source with $\Omega = 0.26$ (or $\lambda \approx 1.44$ μm) and 0.26λ diameter placed at $d = 2a$, will have a FWHM of 0.42λ for when the cylinder in PhC is a free electron model metal and a FWHM of 0.38λ for when it is gold. Similarly, for a PhC with holes filled by $C_2H_4Cl_2$, Fig. 4.7c shows that for a source with $\Omega = 0.23$ (or $\lambda \approx 1.63$ μm) and 0.23λ diameter placed at $d = 2a$ the image intensity has a FWHM of 0.4λ for both the free electron model metal and gold cylinders in PhC.
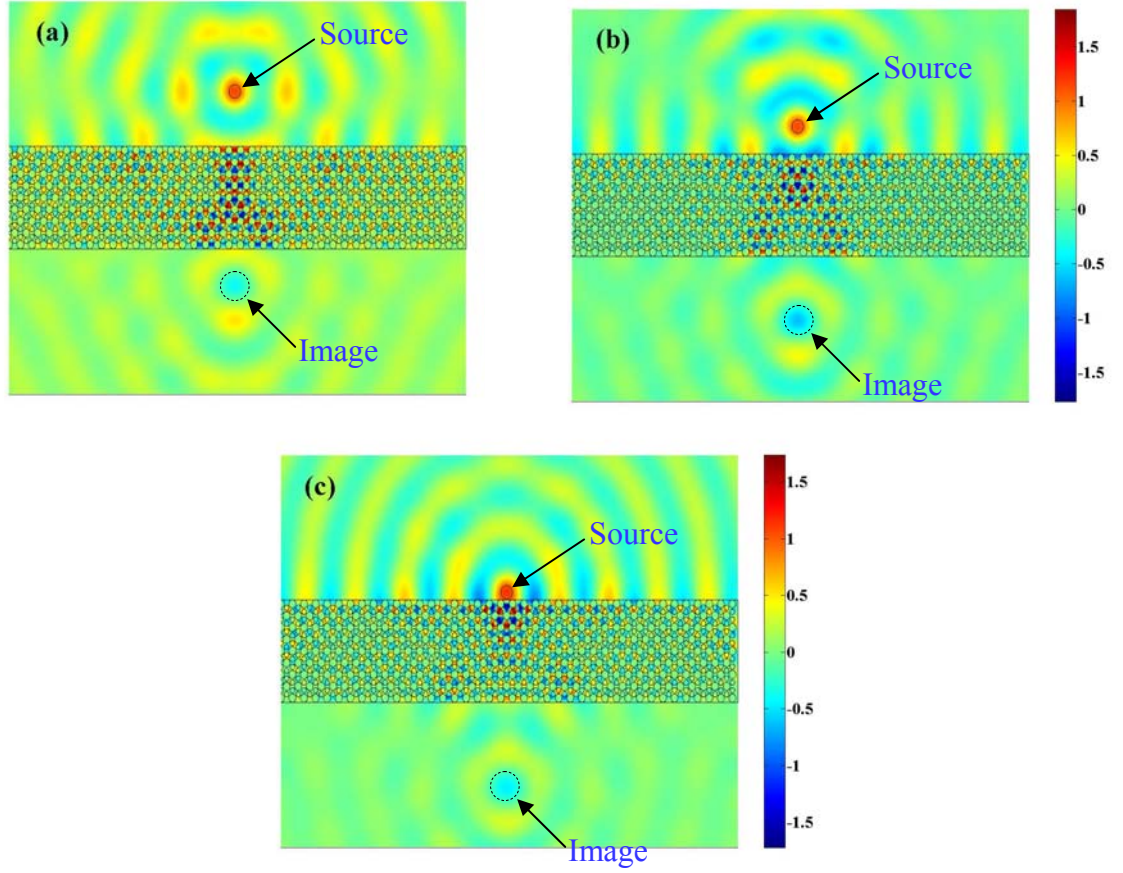
Figure 4.6: Snapshot of the H_z field produced by a point source and its image across a 2D plasmonic crystal slab with normal of the slab surface in ΓM direction of the Brillouin zone. The plasmonic crystal consists of a triangular array of metallic cylinders ($r_a = 0.3a$) having a lattice constant 'a' imbedded in Si ($\varepsilon = 12$) substrate having triangular array of holes ($r_b = 0.2a$) having a lattice constant '$a/\sqrt{3}$'. The holes in the PhC are filled with dichloroethane. The source has a normalized frequency $\Omega = 0.23$ and is place on top of the slab at a distance (a) d = 4a, (b) d = 2a and (c) d = 0.55a.
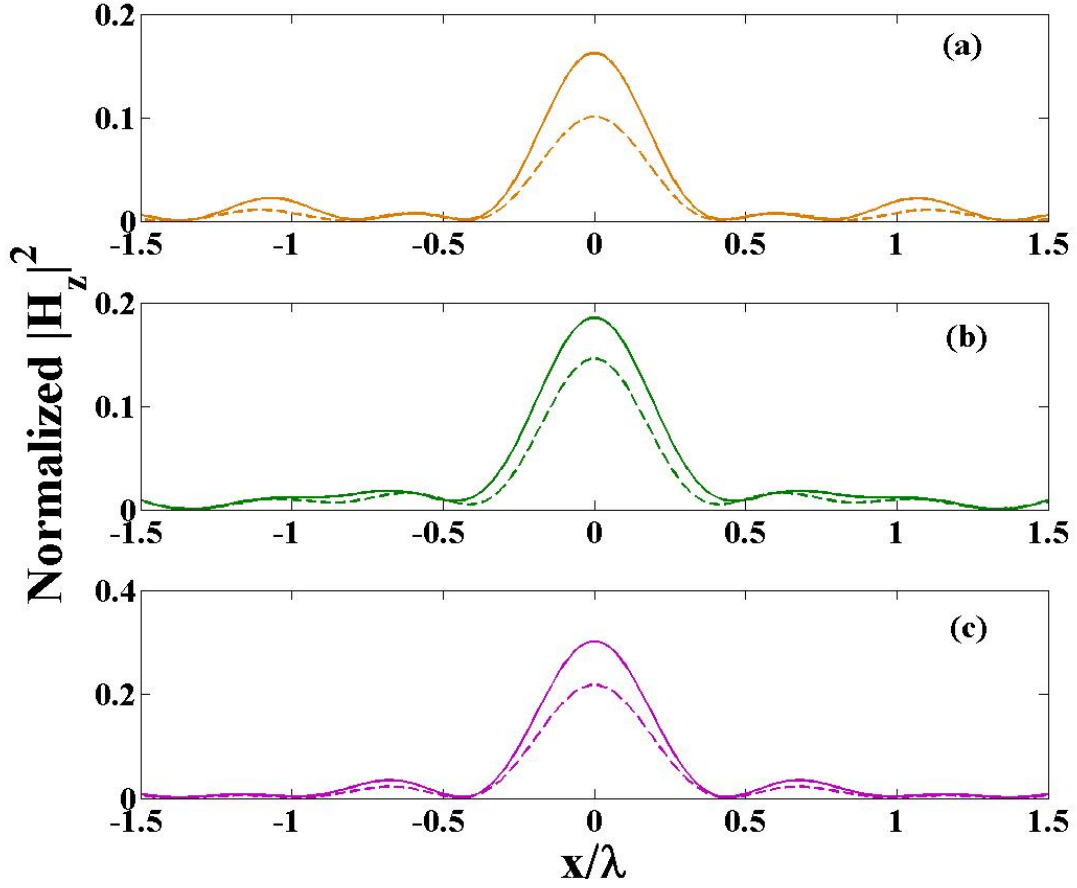
Figure 4.7: The normalized magnetic field intensity vs. the lateral direction at the image plane given in terms of the wavelength (λ), when the source is placed at d = 2*a* from the top of planar 2D plasmonic crystal slab with normal of the slab surface in ΓM direction of the Brillouin zone. The plasmonic crystal consists of a triangular array of metallic cylinders (r_a = 0.3a) having a lattice constant '*a*' imbedded in Si (ε = 12) substrate having triangular array of holes (r_b = 0.2a) having a lattice constant '$a/\sqrt{3}$'. The holes are filled with air (a), tetrachloromethane (b) and dichloroethane (c). Solid line is for when the cylinder in plasmonic crystal is a free electron model metal and the dashed line is for when the cylinder is taken to be as gold.

4.5 CONCLUSION

In conclusion it is shown that the present 2D tPLC has an extra degree of freedom that can be used for tuning the PhC to different n_{eff} at a particular Ω and to different Ω at a particular n_{eff}. In addition the superlensing by the tPLC has been realized with $n_{eff} \sim -1$ at different frequencies, which could then be used for imaging objects of different sizes. Tuning to different frequencies can be realized by varying the fluids in the holes of tPLC. Also it is shown that an object with a smaller size in comparison to the wavelength and when placed far from the lens, a subwavelength image can still be achieved by using the present 2D tPLC model but with the holes filled by a higher dielectric constant fluid. Furthermore, a higher resolution image of an object that is placed closer to the lens can be achieved by using the present 2D tPLC model but with a lower dielectric constant fluid in the holes of PhC. Moreover the present 2D tPLC can be made from materials like gold and Si to achieve subwavelength resolution for applications with novel imaging and coupling functionality in integrated optics components.

Reference:

[1]. A. A. Houck, J. B. Brock, I. L. Chuang, "Experimental observations of a left-handed material that obeys Snell's law", *Physical Review Letters*, **90**, - (2003).
[2]. J. B. Pendry, A. J. Holden, D. J. Robbins, W. J. Stewart, "Low frequency plasmons in thin-wire structures", *Journal of Physics-Condensed Matter*, **10**, 4785-4809 (1998).
[3]. R. A. Shelby, D. R. Smith, S. Schultz, "Experimental verification of a negative index of refraction", *Science*, **292**, 77-79 (2001).
[4]. D. R. Smith, W. J. Padilla, D. C. Vier, S. C. Nemat-Nasser, S. Schultz, "Composite medium with simultaneously negative permeability and permittivity", *Physical Review Letters*, **84**, 4184-4187 (2000).
[5]. C. M. Soukoulis, M. Kafesaki, E. N. Economou, "Negative-index materials: New frontiers in optics", *Advanced Materials*, **18**, 1941-1952 (2006).
[6]. J. B. Pendry, "Negative refraction makes a perfect lens", *Physical Review Letters*, **85**, 3966-3969 (2000).

[7]. X. D. Zhang, "Subwavelength far-field resolution in a square two-dimensional photonic crystal", *Physical Review E*, **71**, - (2005).

[8]. X. Wang, K. Kempa, "Negative refraction and subwavelength lensing in a polaritonic crystal", *Physical Review B*, **71**, - (2005).

[9]. C. Luo, S. G. Johnson, J. D. Joannopoulos, J. B. Pendry, "All-angle negative refraction without negative effective index", *Physical Review B*, **65**, - (2002).

[10]. Z. Y. Li, L. L. Lin, "Evaluation of lensing in photonic crystal slabs exhibiting negative refraction", *Physical Review B*, **68**, - (2003).

[11]. R. Moussa, S. Foteinopoulou, L. Zhang, G. Tuttle, G. T. K. Guven, E. Ozbay, C. M. Soukoulis, "Negative refraction and superlens behavior in a two-dimensional photonic crystal", *Physical Review B*, **71**, - (2005).

[12]. M. Loncar, A. Scherer, Y. M. Qiu, "Photonic crystal laser sources for chemical detection", *Applied Physics Letters*, **82**, 4648-4650 (2003).

[13]. H. Kurt, D. S. Citrin, "Photonic crystals for biochemical sensing in the terahertz region", *Applied Physics Letters*, **87**, - (2005).

[14]. T. Hasek, H. Kurt, D. S. Citrin, M. Koch, "Photonic crystals for fluid sensing in the subterahertz range", *Applied Physics Letters*, **89**, - (2006).

[15]. J. D. Joannopoulos, R. D. Meade, J. N. Winn, *Photonic crystals : molding the flow of light* (Princeton University Press, Princeton, N.J., 1995).

[16]. Y. A. Urzhumov, G. Shvets, "Extreme anisotropy of wave propagation in two-dimensional photonic crystals", *Physical Review E*, **72**, - (2005).

[17]. K. Sakoda, *Optical Properties of Photonic Crystals* (Springer, Berlin, 2001).

[18]. S. Foteinopoulou, C. M. Soukoulis, "Negative refraction and left-handed behavior in two-dimensional photonic crystals", *Physical Review B*, **67**, - (2003).

[19]. E. D. Palik, Ed., *Handbook of optical constants of solids* (Academic Press, Orlando, 1985).

Chapter 5: Optical–near effects for patterning high bandgap materials in a sub-micron scale

5.1 MOTIVATION

In the field of optoelectronics and micro-electronics Silicon carbide (SiC), fused quartz and related silicate glasses are very important materials due to their high bandgap energy, good transmission properties in the UV to IR range, excellent thermal properties, good electrical insulation and high chemical stability [1]. Borosilicate glass has an excellent anodic bonding property and surface integrity which makes it the usual substrate for micro-electro mechanical systems (MEMS). Therefore in order to build a communication interface, micro/nano-holes free of micro-cracks, with good edge and surface quality as well as high aspect ratios need to be formed on the glass substrate.

SiC has great importance in electronic applications due its very high thermal conductivity, high melting point, low thermal expansion coefficient, high breakdown electric field, and high electron saturation. SiC based devices are attractive for blue light-emitting diodes (LEDs), thyristors, U-shaped grooved MOS (UMOS) devices, and UV photodiodes [2]. SiC is used in devices that operate in harsh environments like the combustion chamber of an automobile engine where it is incorporated into the membrane of the pressure sensor. Schottky based diodes (SBDs) fabricated on the 6H-SiC substrates showed high blockage voltages. SiC junction field effect transistors (JFETS) are used in developing a hybrid switch by combining it with a low-voltage Silicon MOSFET, for use in resonant converters and auxillary power supplies. In order to fabricate any SiC based devices with micro patterns, a dry etching technique was used and the etching rate is low

due to the strong binding energy of SiC [3]. Also there are no wet etchants that can bulk micromachine SiC as it is chemically very stable and is actually nature's best etch stopping material. SiC surface micromachining is also a very difficult task like SiC bulk micromachining. Therefore, a novel technique for micro even nano- scale patterning of SiC is in urgent need.

Using traditional micro-machining process for a micro-hole with a diameter below 200 μm is difficult because of the extreme hardness, brittleness, corrosion resistance and melting temperature of materials like borosilicate glass and SiC. Also the conventional thermal and/or chemical machining methods create an excessive heat affected zone. Mechanical machining methods also have limitations in productivity and accuracy [4]. Hence, to solve this problem various machining methods have been proposed like the combination of micro electrical-discharge machining (MEDM) and micro ultrasonic vibration machining (MUSM) [5], micro-abrasive jet machining (AJM) [4], and combination of nanoindenter and HF wet etching [6]. Due to the various working mechanisms of these methods, the results produced are distinct. However high-quality holes in nanoscale were not obtained using these techniques.

Recently, laser micromachining technique emerged as a simple, direct-write process for engineering materials [7]. Since laser induced ablation has several advantages over the conventional mechanical and/or chemical machining; it is a single-step process with very high flexibility, non-contact process, direct patterning without the resist process, good etch-rate and does not require any etchants. Femtosecond (fs) regime offers advantages over the nanosecond (ns) regime, by depositing energy into a material in a very short time period, before any thermal diffusion can occur. Also laser

micormachining is a simple and clean method. Lasers can be used in fabricating high aspect ratio holes with small diameters at designed locations, for cutting and scribing applications. However, for breaking a bond in SiC either high energy density ns laser or fs laser is needed. Femtosecond lasers have been used for ablating 1-µm thick SiC (3C-SiC) films on silicon. At high laser fluence the process is thermally dominated by melting, boiling and vaporizing of the single crystal SiC, and at lower laser fluences the ablation is a defect activated process [8]. Femtosecond laser micromachining of SiC relies on multiphoton absorption [9]. A ns copper-vapor-laser (510 nm and 572 nm wavelength) with energy density as high as 16 J/cm^2 have been used for etching polycrystalline SiC, and despite the high energy density employed the etching rate was very low both in air and water [10].

Hybrid laser processing is also used for the microfabrication of hard and transparent materials like SiC, where the ns pulsed laser beam is used with a medium on the transparent material surface. The medium is used for absorbing the laser beam and generating plasma that would assist in the high-quality ablation of transparent materials. This kind of process is called laser-induced plasma-assisted ablation (LIPAA) [11]. By the nonlinear interaction of fs laser with transparent materials microplasma could be generated within the material which on subsequent expansion results in the fabrication of a small structure. Also by initiating micro-explosion inside the material, a small cavity can be formed with the material ejected from the center [12].

As seen from the above mentioned studies, the processes used for the microfabrication of SiC and glass require very high energies with a complicated optical setup. Also, due to the diffraction limit of light, it is difficult to obtain nanometer sized

105

features. In order to overcome the above mentioned difficulties, the enhancement of the optical near-field obtained by irradiating microspheres by a laser radiation can be used. This enhanced intensity distribution is very sensitive to the diameter of the spheres and to the distance between the sphere and the substrate [13]. Mie-theory calculations have shown that the enhancement is mainly due to the near-field and scattering effects [14]. Using this enhanced near field, silicon and borosilicate glass were massively patterned with a ns pulsed laser [15, 16]. In the present study the parallel submicron patterning of bulk SiC and borosilicate glass is attempted by using a ns-pulsed laser and fs-pulse laser respectively. This can be achieved by irradiating through a monolayer of silica microspheres on SiC or glass substrate. A Nd:yttritium-aluminium-garnet laser (10 ns pulse duration) is used with two different wavelengths, 355 nm and 532 nm, to study the effect of different photon energies in creating submicron features. Also a titanium-doped sapphire (Ti:Sapphire), solid state laser with pulse at full width half maximum (FWHM) around 100 fs and wavelength around 800 nm is used. Different sphere diameters (1.76 μm and 640 nm) are also used in order to understand its effect on the features obtained on the substrates. In the first part of the present chapter the experimental results obtained for the SiC material is discussed and the following part will be the results of experimental study on the borosilicate glass.

5.2 EXPERIMENTAL SET-UP

Both 6H-SiC polytype and borosilicate glass wafer samples are used as the substrate. Monodisperse silica (SiO_2) spherical particles with a diameters of 1.76 μm and 640 nm were utilized. These silica particles are transparent to the near infrared light (800

nm wavelength of the fs laser used). The substrates are first cleaned in an ultrasonic bath with acetone and isopropanol. After drying the substrates with nitrogen, the particle suspension was diluted with de-ionized water (DI) water and deposited on the substrates using a dispenser. The samples were then stored at room temperature over a period of few hours for all the water solvent to evaporate. These spheres self-arranged themselves forming a monolayer, confirmed by using a scanning electron microscope (SEM) in Fig. 5.1.
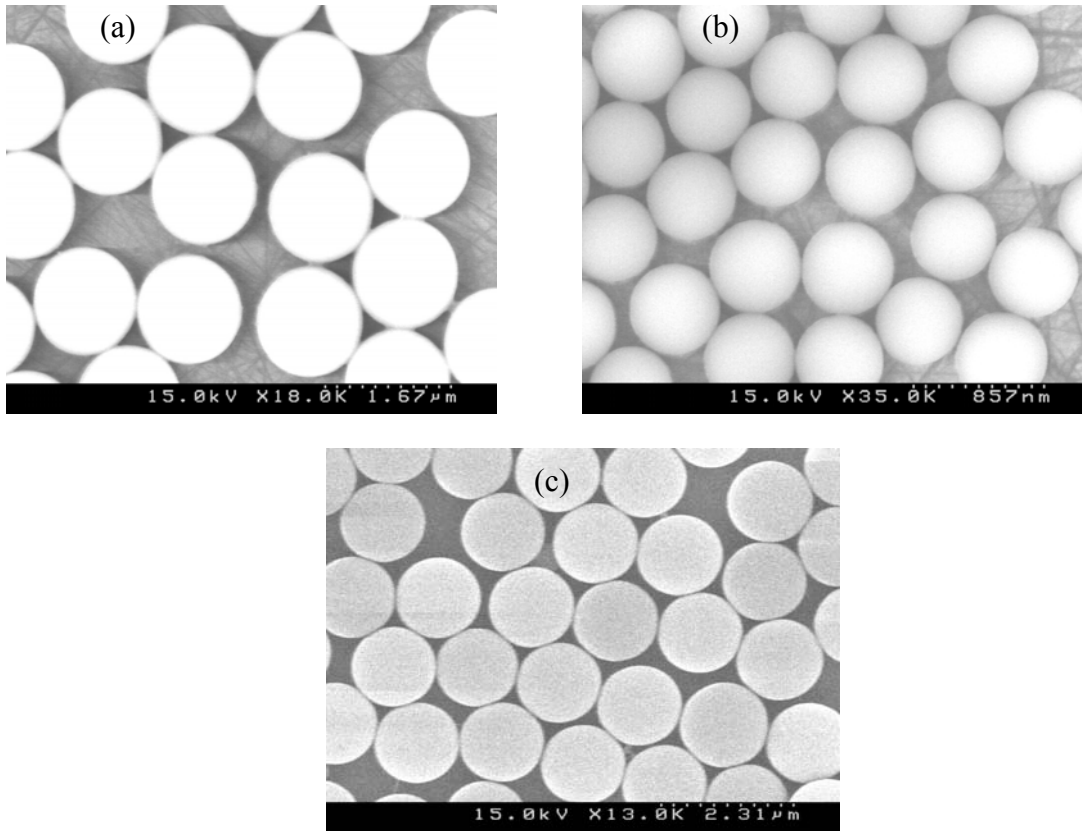

Figure 5.1: SEM micrograph of the monolayer of silica spheres with a diameter of (a) 1.76 µm on SiC, (b) 640 nm on SiC and (c) 1.76 µm on glass.

The schematic of the experimental setup is shown in Fig. 5.2a. The output laser beam is redirected by the harmonic separators and made smaller by using an aperture. By means of a plano-convex lens, the beam is then focused onto the sample which is at the focal distance. The substrate is placed on an XYZ-stage and the polarization of the laser pulse is linear and horizontal to the surface of the substrate. The laser energies used in the experiment were measured using an energy meter. As shown in Fig. 5.2b, a laser is irradiated at a zero angle of incidence onto the monolayer of silica spheres deposited on the substrates. Different laser fluences were used to study the laser energy dependence of the nanostructures formed on the substrate. The laser energies used in the fs laser experiment varied approximately from 200 mJ/cm^2 to 1 J/cm^2. However Zhou et al. [17] have recently used fs pulses at much higher laser energies to create sub-diffraction limit modifications on glass substrate. The energy of the incident fs laser is varied by changing the delay time between the two pockel cells during the amplification using a synchronization and delay generator (SDG). Due to different delay times, the laser beam has to be compressed accordingly to maintain a constant pulse width and this is done by moving the compressor optics while monitoring the output laser beam pulse width with a single shot auto-correlator (SSA) and an oscilloscope. The laser energies used in the ns laser experiment varied approximately from 600 mJ/cm^2 to 6 J/cm^2 depending on the wavelength used. The ns laser pulse can be altered by changing the voltage of the source. The substrates after laser submicron patterning was characterized by using scanning electron microscope (SEM: Hitachi S4500) and the depths were measured by using an atomic force microscope (AFM: Nanoscope D3100). To obtain good SEM images for

108

glass substrate and in order to reduce the charging effects a very thin layer of gold is

deposited on the substrate.


(a)

(b)
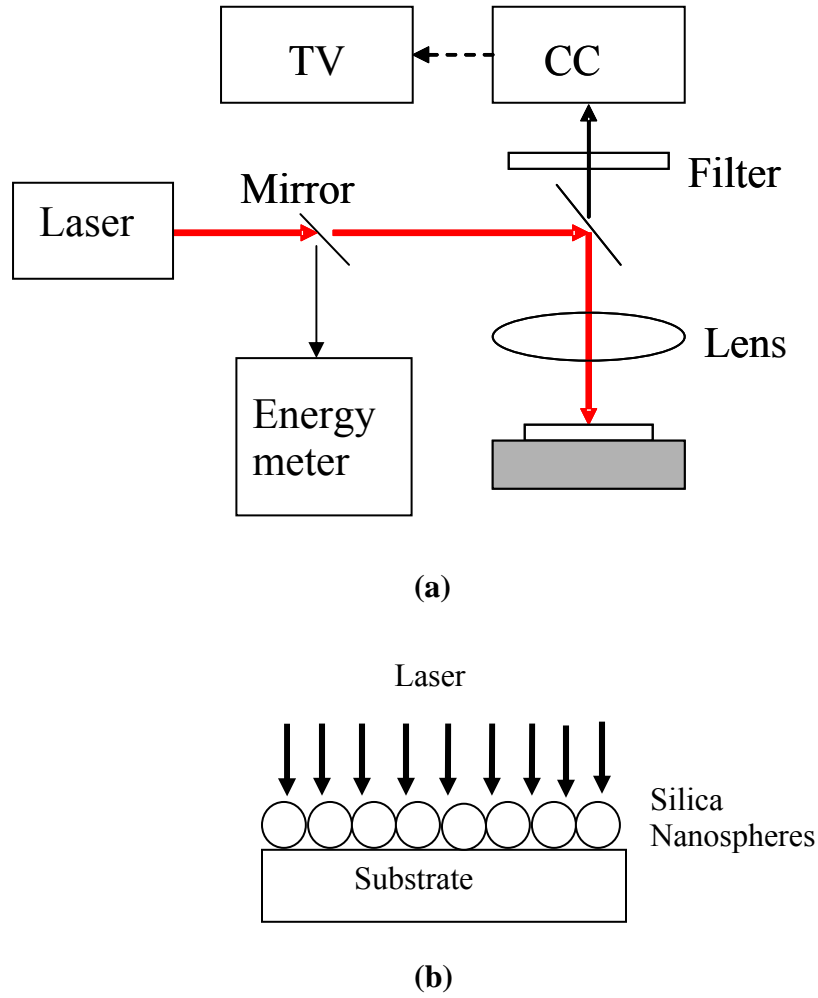
Figure 5.2: Schematic of (a) experimental setup, (b) irradiation of the spheres on substrate.

5.3 DIRECT PATTERNING ON SILICON CARBIDE (SIC) USING NANOSECOND LASER

The experiments were conducted at different energies and as predicted by Mie theory, it was found that the minimum energy required for creating features on SiC is smaller for bigger spheres irrespective of the laser wavelength. This is because of the higher optical field enhancement for bigger spheres. At a laser wavelength of 355 nm, the features started appearing at an incident energy density of 650 mJ/cm^2 for 1.76 μm spheres, whereas for 640 nm spheres at least 850 mJ/cm^2 energy density is needed. However, in the absence of spheres the actual threshold energy for substrate damage is found to be around 4 J/cm^2.

Figure 5.3 shows a SEM picture of the features obtained for 355 nm wavelength ns laser with both 1.76 μm and 640 nm spheres at 950 mJ/cm^2 and 850 mJ/cm^2 respectively. The features are well defined for the 1.76 μm spheres compared to the smaller sphere case. The possible ablation mechanism for the formation of holes is discussed later. Figure 5.4 shows the variation in feature depth with respect to the laser intensity for a 355 nm laser wavelength and 1.76 μm silica spheres. For the laser intensities used in this study, the depth increases from 90 nm to 210 nm with laser intensity. For the same conditions, Fig. 5.5 shows an increase in feature diameter from 300 nm to 450 nm depending on the laser intensity. The different rate of increase in both the feature depth and diameter with laser intensity suggests that the interaction of the laser beam with the SiC substrate might be non-linear.
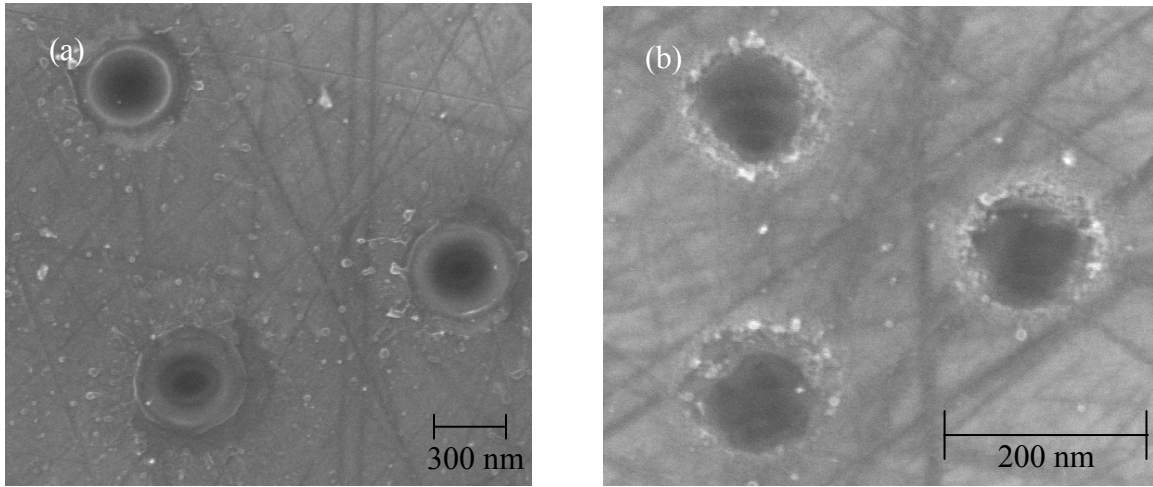
Figure 5.3: Features formed on the SiC substrate with a 355 nm laser (a) 1.76 µm diameter spheres and 950 mJ/cm^2 and (b) 640 nm diameter spheres and 850 mJ/cm^2.
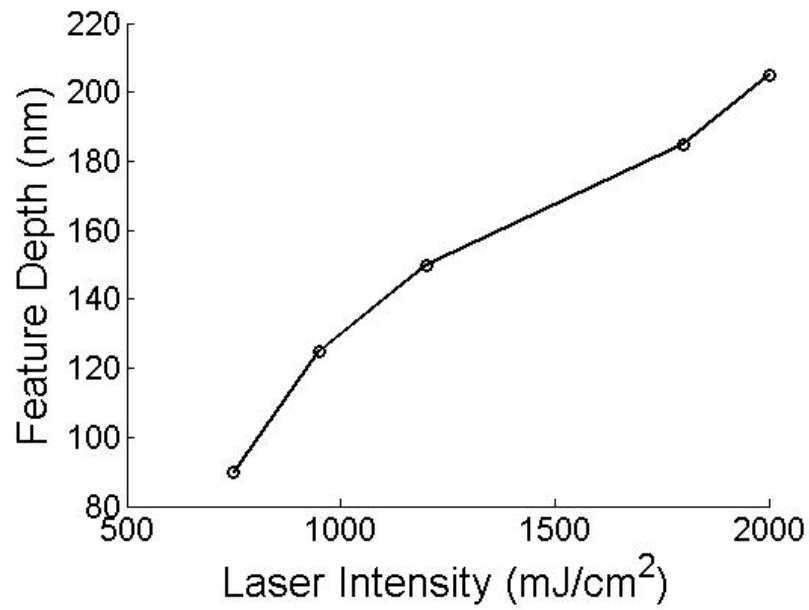

Figure 5.4: Variation in the feature depth with respect to the laser intensity for 355 nm laser and 1.76 µm spheres.
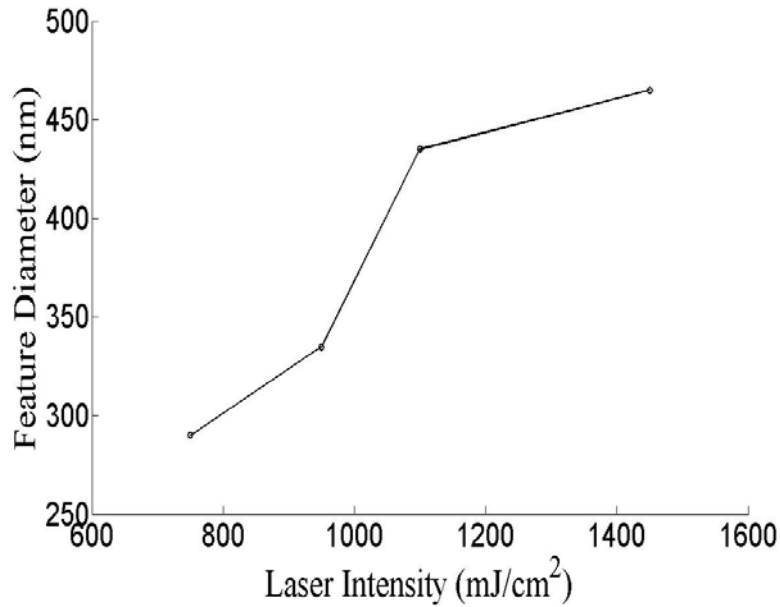
Figure 5.5: Variation in the feature diameter with respect to the laser intensity for 355 nm laser and 1.76 μm spheres.

Figure 5.6 is a scanning electron micrograph of the features obtained for a ns laser wavelength of 532 nm with 1.76 μm and 640 nm spheres at 2 J/cm^2 and 6 J/cm^2 respectively. It is evident that SiC can be submicron patterned at 532 nm despite the material being completely transparent to this wavelength. The threshold energy needed for the formation of holes is around 2 J/cm^2 for 1.76 μm spheres and 5 J/cm^2 for the 640 nm spheres. Figure 5.7 shows the atomic force microscope data plot for the features obtained with 1.76 μm silica spheres. The feature diameters varied from 320 nm to 450 nm and the depths varied between 100 nm to 175 nm, depending on the laser intensity.

112
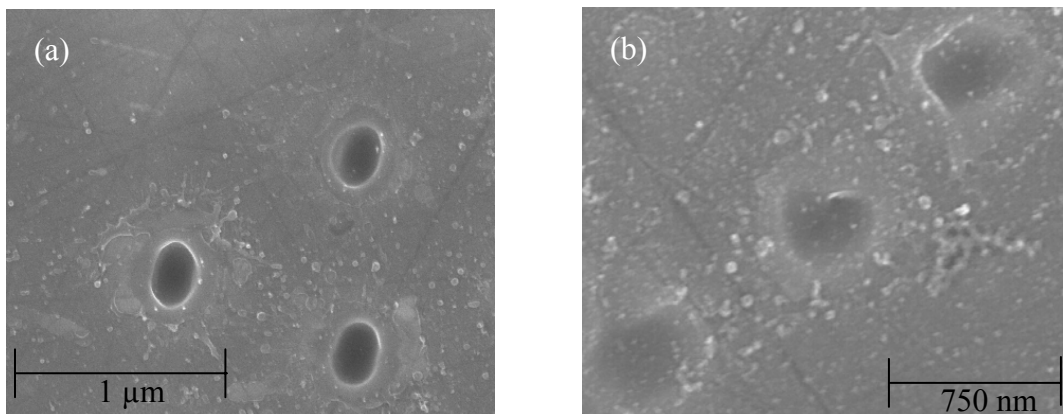
Figure 5.6: Features formed on the SiC substrate with a 532 nm laser (a) 1.76 μm diameter spheres and 2 J/cm^2 and (b) 640 nm diameter spheres and 6 J/cm^2.
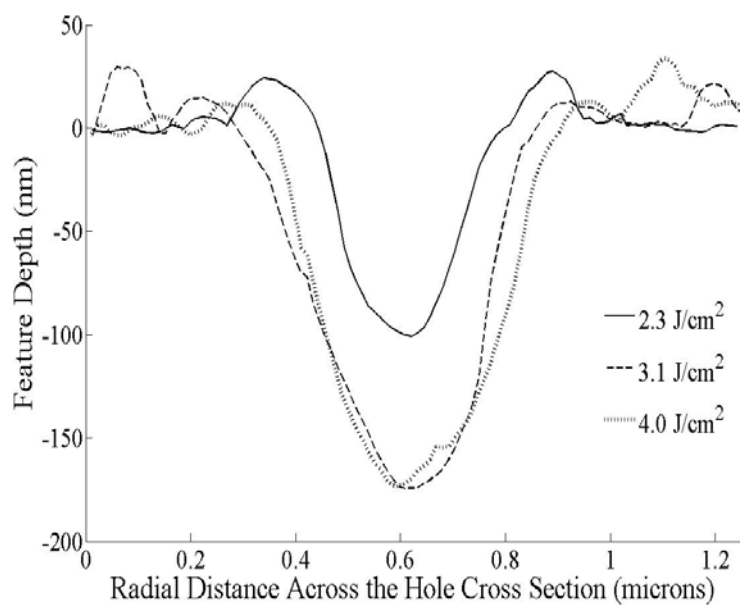

Figure 5.7: AFM cross section view of the features obtained with 532 nm laser and 1.76 μm spheres.

113

The minimum feature diameter observed for both wavelengths is approximately the same, indicating a strong dependence on the band-gap energy of the material [18]. Also the depth of the features obtained with 355 nm wavelength is larger because of the higher absorption coefficient of SiC in the ultraviolet spectrum. From the above results, it can be concluded that, for the ablation of SiC with 532 nm laser, higher intensity is required compared to the 355 nm laser. This is because the band-gap energy of SiC (6H-SiC polytype) is around 3.0 eV and the electron affinity is around 4.0 eV, which makes the minimum energy required for bond breakage to be near 7.0 eV. The photon energy of the 355 nm and 532 nm wavelength are approximately 3.49 eV and 2.32 eV respectively. Therefore, in order to break the bonds using these wavelengths, the interaction of the laser with the SiC under optical near-field effect has to be a multiphoton process. Also, since SiC is transparent at 532 nm wavelength, the submicron features formed could be due to the non-linear interaction of the visible wavelength laser with SiC.

SiC is an indirect wide band gap semiconductor material and hence due to multiphoton absorption, the electrons jump from the valence band to the higher energy levels of the conduction band. The possibility of electron absorbing another photon in the conduction band is more before getting scattered with a phonon. Once the electron absorption of a photon takes place, the momentum is conserved by either plasmons or impurities or phonons. Therefore the phonon energy increases with the number of electrons in the conduction band. This increase in phonon energy would lead to a lattice disorder that eventually makes bond breaking for ablation possible. The relation between the number of bond scission and the excitation is linear when the band-gap energy is

larger than the bond energy otherwise the relation is nonlinear due to the requirement of higher order excitation energy [19].

5.4 PATTERNING ON BOROSILICATE GLASS USING FEMTOSECOND LASER

Figure 5.8 shows a SEM image of the nanostructures formed on the borosilicate glass by using the optical near-field enhancement for different laser fluences and one pulse irradiation. The nanostructures formed seem to be elliptical in shape as predicted in [20]. This is due to the laser polarization, which plays an important role in optical enhancement. Also it was found that most of the silica particles are removed from the substrate surface. These particles are removed from the surface mainly due to the deformation force and/or the high ablative force exceeding the particle-surface adhesion force [21]. Figure 5.8 shows that as the laser fluence decreases the nanostructures formed did not change in shape, unlike in some studies where sombrero-shape nanodents are formed at high laser fluences and bowl-shape nanodents are formed at low laser fluences [13, 22]. Also, from Figure 5.8 it can be seen that for the incident laser fluences of 330 mJ/cm^2, 550 mJ/cm^2 and 765 mJ/cm^2 the diameter of the holes along the major axis are approximately 250 nm, 300 nm and 350 nm respectively. Hence, the diameter of the nanostructures formed on the borosilicate glass increases with the laser fluence. Figure 5.9 shows the three-dimensional AFM scanning profile of the submicron structure formed on the borosilicate glass and it can be seen that the structures formed are elliptical in shape for different laser fluences which is in agreement with the SEM images (Fig. 5.8).

Figure 5.10 shows the cross-sectional or two-dimensional (2D) AFM profile of the submicron structures along their major axis and it can be seen clearly that for laser

fluences of 230 mJ/cm^2, 550 mJ/cm^2 and 950 mJ/cm^2 the depth of the structures formed are approximately 180 nm, 250 nm and 290 nm respectively. These measured AFM cross-sectional profiles are in good agreement with the predicted profiles for similar incident laser energies [20]. From 2D AFM profiles we can observe that the bottom of the features along the major axis is flattened. The features obtained can be explained by the theoretical model prediction using Fokker-Planck equation to describe the ablation mechanism of the glass substrate during fs laser pulses [20] and also within the context of Mie theory, which dictates strong forward scattering [23]. In general, the substrate modifications would be expected at the contact point due to the normal incidence of the laser pulse [24]. These submicron structures would then be driven by the intensity distribution in the surface plane.
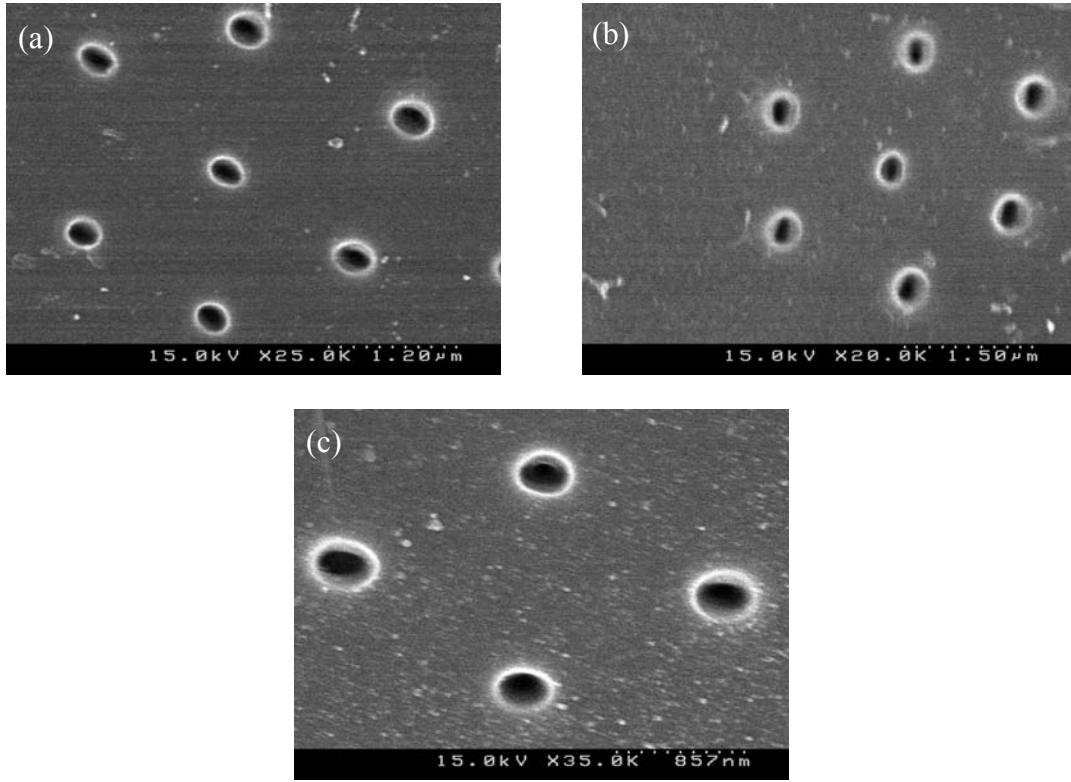
Figure 5.8: SEM micrograph of the features formed on the glass substrate using microspheres with a single laser pulse irradiation (λ = 800 nm and FWHM = 100 fs) having laser fluence of (a) 330 mJ/cm^2, (b) 550 mJ/cm^2 and (c) 765 mJ/cm^2.
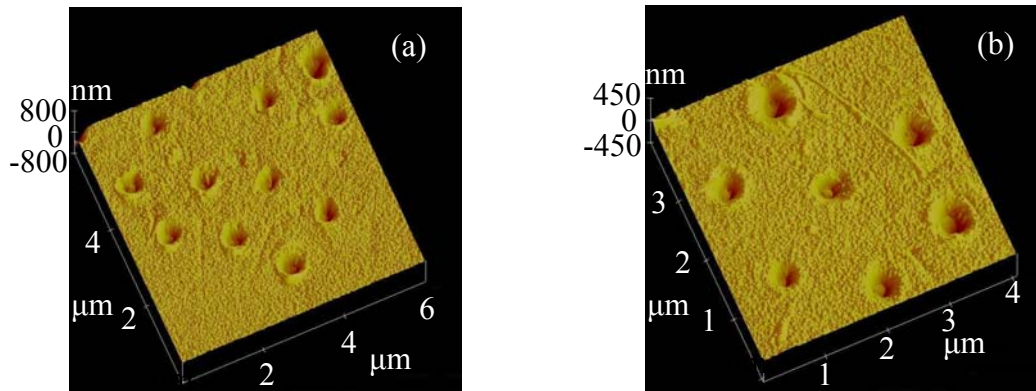
Figure 5.9: AFM profiles of the features formed on the glass substrate using microspheres with a single laser pulse irradiation (λ=800 nm and FWHM= 100 fs) having laser fluence of (a) 230 mJ/cm^2 and (b) 405 mJ/cm^2.

117
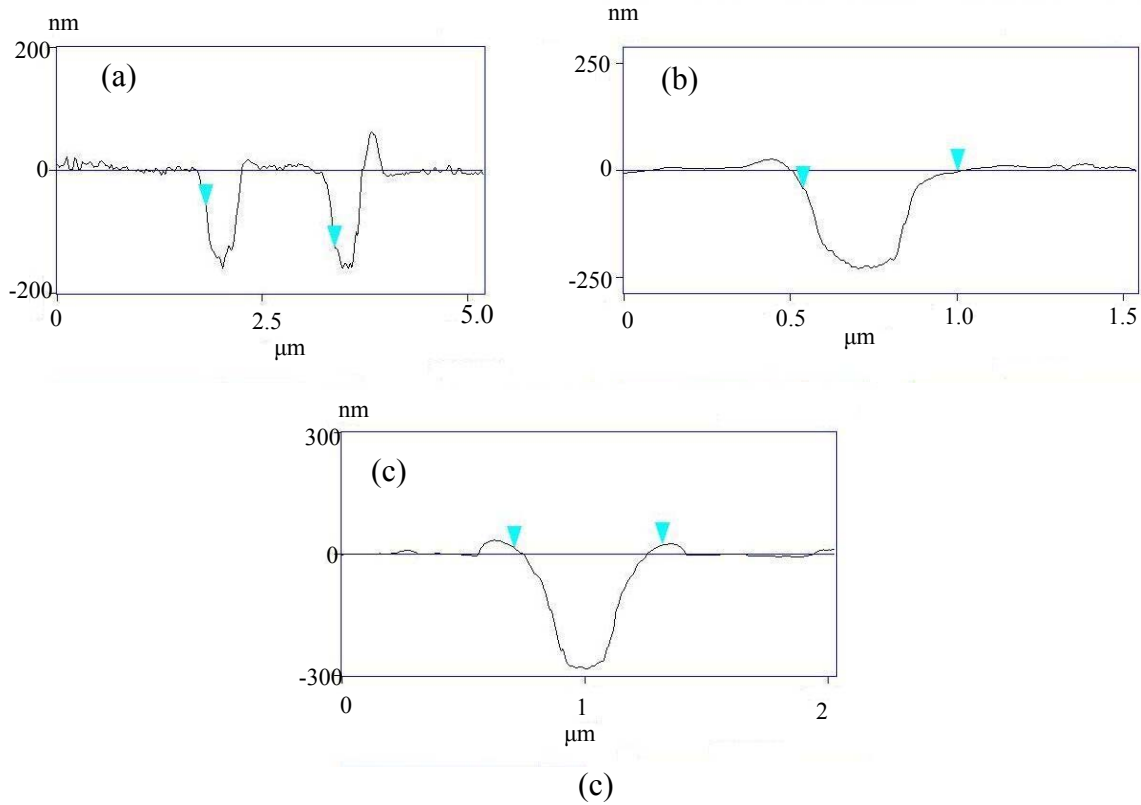
Figure 5.10: AFM cross-section profiles of the features formed on the glass substrate using microspheres with a single laser pulse irradiation (λ = 800 nm and FWHM = 100 fs) having laser fluence of (a) 230 mJ/cm^2, (b) 550 mJ/cm^2 and (c) 950 mJ/cm^2.

5.5 CONCLUSION

Submicron patterning of the SiC material is achieved with features of diameter ranging from 150 nm to 450 nm, with depths ranging from 70 nm to 200 nm depending on the laser energy. This kind of patterning in a hard material like SiC is made possible by using the optical near field enhancement, obtained by the irradiation of silica spheres with a laser beam. Also an experimental study has been performed on a borosilicate glass substrate using a fs laser. The features formed on the glass surface have diameters and depths in the order of 300 nm and 250 nm, depending on the incident fs laser intensity.

The experimentally observed damage is in good agreement with the theoretical predictions of surface modifications [20]. Therefore, it is shown that the surface features can be created below the diffraction limit and at the nanoscale. This unique technique can be used for patterning in a massive and parallel fashion, such as on a transparent and bio-compatible material like the borosilicate glass or SiC to obtain a very thin bio-membrane for bio-filter applications. Also this study would open up fabrication of new nano-devices having SiC as the main substrate.

References

[1]. J. Zhang, K. Sugioka, K. Midorikawa, "High-quality and high-efficiency machining of glass materials by laser-induced plasma-assisted ablation using conventional nanosecond UV, visible, and infrared lasers", *Applied Physics a-Materials Science & Processing*, **69**, S879-S882.

[2]. R. Reitano, P. Baeri, N. Marino, "Excimer laser induced thermal evaporation and ablation of silicon carbide", *Applied Surface Science*, **96-8**, 302-308.

[3]. J. Zhang, K. Sugioka, S. Wada, H. Tashiro, K. Toyoda, "Direct photoetching of single crystal SiC by VUV 266 nm multiwavelength laser ablation", *Applied Physics a-Materials Science & Processing*, **64**, 367-371.

[4]. D. S. Park, M. W. Cho, H. Lee, W. S. Cho, "Micro-grooving of glass using micro-abrasive jet machining", *Journal of Materials Processing Technology*, **146**, 234-240.

[5]. B. H. Yan, A. C. Wang, C. Y. Huang, F. Y. Huang, "Study of precision micro-holes in borosilicate glass using micro EDM combined with micro ultrasonic vibration machining", *International Journal of Machine Tools & Manufacture*, **42**, 1105-1112.

[6]. S. W. Youn, C. G. Kang, "Maskless patterning of borosilicate glass nanoindentation-induced etch-hillock surface using phenomena", *Journal of Non-Crystalline Solids*, **351**, 3065-3074.

[7]. D. Sciti, A. Bellosi, "Laser-induced surface drilling of silicon carbide", *Applied Surface Science*, **180**, 92-101.

[8]. Y. Y. Dong, C. Zorman, P. Molian, "Femtosecond pulsed laser micromachining of single crystalline 3C-SiC structures based on a laser-induced defect-activation process", *Journal of Micromechanics and Microengineering*, **13**, 680-685.

[9]. S. K. Sundaram, E. Mazur, "Inducing and probing non-thermal transitions in semiconductors using femtosecond laser pulses", *Nature Materials*, **1**, 217-224.

[10]. S. I. Dolgaev, A. A. Lyalin, G. A. Shafeev, V. V. Voronov, "Fast etching and metallization of SiC ceramics with copper-vapor-laser radiation", *Applied Physics a-Materials Science & Processing*, **63**, 75-79.

[11]. K. Sugioka, K. Obata, K. Midorikawa, M. H. Hong, D. J. Wu, L. L. Wong, Y. F. Lu, T. C. Chong, "Advanced materials processing based on interaction of laser beam and a medium", *Journal of Photochemistry and Photobiology a-Chemistry*, **158**, 171-178.

[12]. E. N. Glezer, E. Mazur, "Ultrafast-laser driven micro-explosions in transparent materials", *Applied Physics Letters*, **71**, 882-884.

[13]. Y. Lu, S. Theppakuttai, S. C. Chen, "Marangoni effect in nanosphere-enhanced laser nanopatterning of silicon", *Applied Physics Letters*, **82**, 4143-4145.

[14]. H. J. Munzer, M. Mosbacher, M. Bertsch, J. Zimmermann, P. Leiderer, J. Boneberg, "Local held enhancement effects for nanostructuring of surfaces", *Journal of Microscopy-Oxford*, **202**, 129-135.

[15]. S. Theppakuttai, S. Chen, "Nanoscale surface modification of glass using a 1064 nm pulsed laser", *Applied Physics Letters*, **83**, 758-760.

[16]. S. Theppakuttai, S. C. Chen, "Submicron ripple formation on glass surface upon laser-nanosphere interaction", *Journal of Applied Physics*, **95**, 5049-5052.

[17]. Y. Zhou, M. H. Hong, J. Y. H. Fuh, L. Lu, B. S. Luk'yanchuk, Z. B. Wang, L. P. Shi, T. C. Chong, "Direct femtosecond laser nanopatterning of glass substrate by particle-assisted near-field enhancement", *Applied Physics Letters*, **88**, -.

[18]. F. Korte, J. Serbin, J. Koch, A. Egbert, C. Fallnich, A. Ostendorf, B. N. Chichkov, "Towards nanostructuring with femtosecond laser pulses", *Applied Physics a-Materials Science & Processing*, **77**, 229-235.

[19]. N. Itoh, "Bond scission induced by electronic excitation in solids: A tool for nanomanipulation", *Nuclear Instruments & Methods in Physics Research Section B-Beam Interactions with Materials and Atoms*, **122**, 405-409.

[20]. A. Heltzel, A. Battula, J. R. Howell, S. C. Chen, "Nanostructuring borosilicate glass with near-field enhanced energy using a femtosecond laser pulse", *Journal of Heat Transfer-Transactions of the ASME*, **129**, 53-59.

[21]. Y. W. Zheng, B. S. Luk'yanchuk, Y. F. Lu, W. D. Song, Z. H. Mai, "Dry laser cleaning of particles from solid substrates: Experiments and theory", *Journal of Applied Physics*, **90**, 2135-2142.

[22]. Z. B. Wang, M. H. Hong, B. S. Luk'yanchuk, S. M. Huang, Q. F. Wang, L. P. Shi, T. C. Chong, "Parallel nanostructuring of GeSbTe film with particle mask", *Applied Physics a-Materials Science & Processing*, **79**, 1603-1606.

[23]. T. Ikawa, T. Mitsuoka, M. Hasegawa, M. Tsuchimori, O. Watanabe, Y. Kawata, "Azobenzene polymer surface deformation due to the gradient force of the optical near field of monodispersed polystyrene spheres", *Physical Review B*, **64**, -.

[24]. Z. B. Wang, M. H. Hong, B. S. Luk'yanchuk, Y. Lin, Q. F. Wang, T. C. Chong, "Angle effect in laser nanopatterning with particle-mask", *Journal of Applied Physics*, **96**, 6845-6850.

Chapter 6: Outlook

6.1 FINAL SUMMARY

Near-field effects for submicron patterning and developing new design for plasmonic optical devices has been explored in this dissertation. The following specific aims have been achieved (i) Tuning the extraordinary transmission by introducing an extra geometrical factor and also by using an external magnetic field, (ii) Developing a unique thermal emitter that has emission properties similar to laser by combing the plasmonics and photonic crystals, (iii) Designing a tunable superlens for subwavelength imaging by using plasmonic crystal and finally (iv) direct, parallel submicron patterning of high bandgap materials,

In the case of the first aim it was shown that with metallic gratings or holes having converging-diverging channels (CDC) the transmission peaks can be selected by varying the width of gaps at the throat. By selecting a small throat gap high transmission resonances in a very narrow band can be achieved. High transmission occurs in metallic gratings when the phases across the grating are in-phase for a Fabry-Perot or waveguide resonance to exist [1]. The CDC shape of the channel could aid the wave inside the channel to become an in-phase standing wave. In addition it was shown that for a rectangular hole pair array silver (Ag) film the presence of externally applied magnetic field $\mathbf{H}$ would alter the transmission resonance peak locations. The shift is dependent on the magnitude and the direction of the $\mathbf{H}$. This is due to the shift of cavity resonance condition as a result of the magento-induced anisotropy in the optical properties of the

121

metallic film. The proposed CDC shape along with the external magnetic field could lead to extraordinary transmission at any wavelength that has a wide range of potential applications in integrated photonic circuits, tunable filters, near-field optics, imaging nanolithography and biological sensors.

The second aim is to develop a unique thermal emitter in any wavelength range. This can be achieved by having a cavity surrounded on one side by a thin CDC Ag grating and a one-dimensional (1D) photonic crystal (PhC) on the other side. The thermal emitter has emission properties that are – highly monochromatic (FWHM ~ 4 nm) with large temporal coherence, extremely directional (FWHM ~ 1.15°) with far field spatial coherence and is *p*-polarized. The presence of cavity between the CDC gratings and 1D PhC would change the dispersion characteristics of the surface plasmons (SPs). The narrow peaks in the spectral and directional emission are mainly due to the strong resonances in the cavity supported by the Ag CDC grating and 1D PhC. The thermal source is tunable to various wavelengths and directions of emission with the choice of right materials along with the parameters of the grating, cavity length and 1D PhC. Thus, the CDC grating and 1D PhC with a cavity offers a simple multilayer structure that could have great implications in a variety of applications with diverse wavelength range of interest. Also the present thermal emitter with a varying cavity length can be used as a single light source for different colors which could make it ideal for sensitive, multicolor and multiplexing applications in molecular biology and bioengineering.

For the third aim a 2D tunable plasmonic crystal (2D tPLC) was proposed. It has a triangular array of metallic cylinders in a Si ($\varepsilon = 12$) substrate with a graphene array of holes. The 2D tPLC has an extra degree of freedom that can be used for tuning the PhC to

122

different effective refractive index (n_{eff}) at a particular frequency (Ω) and to different Ω at a particular n_{eff}. In addition the superlensing by the tPLC has been realized with $n_{eff} \sim -1$ at different frequencies, which could then be used for imaging different size objects in air. Tuning to different frequencies can be realized by varying the fluids in the holes of tPLC. It is shown that an object with a smaller size in comparison to the wavelength and when placed far from the lens, a subwavelength image can be achieved by using the present 2D tPLC model with the holes filled by a higher dielectric constant fluid. Whereas, a higher resolution image of an object that is placed closer to the lens can be achieved by using the present 2D tPLC model with a lower dielectric constant fluid in the holes of PhC. The proposed 2D tPLC can be made from materials like gold and Si to achieve subwavelength resolution for applications with novel imaging and coupling functionality in integrated optics components.

Finally for the last aim the submicron patterning on transparent high bandgap materials like the SiC and borosilicate glass is made possible by using optical near-field enhancement which is obtained by the irradiation of silica spheres with a laser beam and it can be explained by Mie scattering theory. When the diameter of the sphere is equal to or greater than the laser wavelength, light is scattered elastically and the field is enhanced several times at the exit side of the spheres. Such optical enhancement can lead to local melting or even vaporization of the substrate materials for surface patterning. Using this technique features with diameter ranging from 150 nm to 450 nm and with depths ranging from 70 nm to 200 nm were achieved depending on the laser energy. Surface patterning on a borosilicate glass substrate was achieved by using fs laser. The features formed on the glass surface have diameters and depths in the order of 300 nm and 250

123

nm depending on the incident fs laser intensity. The experimentally observed damage is in good agreement with the theoretical predictions of surface modifications [2]. Therefore, it is shown that the surface features can be created below the diffraction limit and possibly at the sub-nanometer scale. This unique technique can be used for patterning in a massive and parallel fashion on a transparent and bio-compatible material to obtain a very thin bio-membrane for bio-filter applications. Also this study would open up fabrication of new devices having SiC as the main substrate.

6.2 FUTURE WORK

In the field of metal-optics or plasmonics there are still lots of research opportunities to explore and develop. These include SPs based circuits, where electronics could merge with photonics at the nanoscale [3] for developing ultra-low loss optically functional device. The new designs proposed and analyzed in this dissertation may open a chance to implement them in non-conventional plasmonic chips. Hence it would be of significant interest to fabricate these new plasmonic optical devices and conduct experiments to confirm the tunable superlens for optical imaging with subwavelength resolution, new thermal light source with unprecedented performance and tunable optical filters with fine properties. But in order to build a complete circuit chip with plasmonic based optical devices then plasmonic couplers with high conversion efficiency and waveguides with low propagation loss comparable to the conventional optical counterparts have to be designed and demonstrated.

6.3 COMPUTATIONAL COST

The governing equation used in the present study is derived from the Maxwell's equations for an isotropic homogeneous medium with no current and charge sources assumptions. Also the electromagnetic wave is assumed to be having a harmonic propagation. Under these circumstances the present model can be used for most of the simulation studies. But, the limitation of the model lies in the macroscopic nature of the equations. The objects having dimensions in the range of 10 nm and lower can not be simulated with the present model. Since the total number of nuclei and electrons present in the object will have fluctuations that can not be spatially averaged.

In addition the present model can be used for a complex 2D simulation studies. But, for 3D simulations the computational domain has to be simple. This is due to the fact that the COMSOL 3.2a is limited in the amount of memory (4 GB) it can use for calculations. Subsequently the number of degrees of freedom that can be solved for 3D is around 1.2×10^5 and for 2D is approximately 1×10^6. But on the whole the present model is very easy to use and the accuracy of the model increases with the total number of mesh elements.

Reference

[1]. X. Jiao, P. Wang, L. Tang, Y. Lu, Q. Li, D. Zhang, P. Yao, H. Ming, J. Xie, "Fabry-Perot-like phenomenon in the surface plasmons resonant transmission of metallic gratings with very narrow slits", *Applied Physics B-Lasers and Optics*, **80**, 301-305 (2005).
[2]. A. Heltzel, A. Battula, J. R. Howell, S. C. Chen, "Nanostructuring borosilicate glass with near-field enhanced energy using a femtosecond laser pulse", *Journal of Heat Transfer-Transactions of the Asme*, **129**, 53-59 (2007).
[3]. E. Ozbay, "Plasmonics: Merging photonics and electronics at nanoscale dimensions", *Science*, **311**, 189-193 (2006).

Appendix

```matlab
clear all

clc


% CONSTANTS

    hp      = 6.626e-34;         % Planck's Constant

    cO      = 3e8;               % Speed of light in vacuum

    mu0      = 4*pi*1e-7;        % Permeability of vacuum

    es_0    = 8.5e-12;           % Permittivity of vacuum

    j_ev    = 1.602e-19;         % Joule to ev conversion


for bari = 1 : 501

   Lamda(bari) = (bari-1)*1e-7+3.5e-6;

   Lam            = Lamda(bari);

   energy         = hp*cO/(Lam*j_ev);

   esAu           = DielectricConstant(3,0,energy);    % Dielectric constant for Au

   for barj = 1 : 2

   flgc


   % INITIALIZING THE FEM STRUCUTURE

   clear fem

   fem.dim='U';
```

```matlab
fem.form='coefficient';

fem.shape=2;

fem.sshape=2;


% CREATING THE GEOMETRY

pe = 3500e-9/Lam;          % Grating period length (nm).

h  = 500e-9/Lam;           % Aperture (nm)

Sp = pe-h;                 % Width of the Metal grating (nm).

L  = pe;                   % Length of 2D computational domain.

b  = 2000e-9/Lam;          % Intermediate layer thickness (nm).

c  = 1000e-9/Lam;          % PML thickness (nm).

e  = 3000e-9/Lam;          % Grating thickness (nm).

So = 10e-9/Lam;            % Source region thickness (nm).

we = h-450e-9/Lam;         % Curvature of the Nanotip.

RX = rect2(-Lam*L/2,Lam*L/2,-c*Lam/2,c*Lam/2);

RX = move(RX,0,Lam/2*(4*b+e+2*So+c));

RIX = rect2(-Lam*L/2,Lam*L/2,-So*Lam/2,So*Lam/2);

RIX = move(RIX,0,Lam/2*(4*b+e+So));

RVIII = rect2(-Lam*L/2,Lam*L/2,-b*Lam/4,b*Lam/4);

RVIII = move(RVIII,0,Lam/2*(7*b/2+e));

RVII = rect2(-Lam*L/2,Lam*L/2,-b*Lam/4,b*Lam/4);

RVII = move(RVII,0,Lam/2*(5*b/2+e));

RVI = rect2(-Lam*L/2,Lam*L/2,-b*Lam/2,b*Lam/2);
```

```
RVI = move(RVI,0,Lam/2*(b+e));

RV  = rect2(-Lam*L/2,Lam*L/2,-e*Lam/2,e*Lam/2);

Ra  = poly2([-h*Lam/2 h*Lam/2 we*Lam/2 h*Lam/2 -h*Lam/2 -we*Lam/2],

[e*Lam/2 e*Lam/2 0 -e*Lam/2 -e*Lam/2 0]);

RV  = RV - Ra;

RIV = rect2(-Lam*L/2,Lam*L/2,-b*Lam/2,b*Lam/2);

RIV = move(RIV,0,-Lam/2*(b+e));

RIII = rect2(-Lam*L/2,Lam*L/2,-b*Lam/4,b*Lam/4);

RIII = move(RIII,0,-Lam/2*(5*b/2+e));

RII = rect2(-Lam*L/2,Lam*L/2,-b*Lam/4,b*Lam/4);

RII = move(RII,0,-Lam/2*(7*b/2+e));

RI = rect2(-Lam*L/2,Lam*L/2,-c*Lam/2,c*Lam/2);

RI = move(RI,0,-Lam/2*(4*b+c+e));

fem.geom=RX+RIX+RVIII+RVII+RVI+RV+RIV+RIII+RII+RI+Ra;


% FEM CONSTANTS

fem.const.teta      = 0;

fem.const.k         = 2*pi/Lam;

fem.const.cO        = 3e8;

fem.const.mu_0      = 4*pi*1e-7;

fem.const.es_0      = 8.85e-12;

fem.const.h_p       = 6.626e-34;

fem.const.m         = 2;
```

```matlab
fem.const.sigma        = 1e16;

fem.const.L_PML        = c*Lam;

fem.const.Lx           = L*Lam;

fem.const.W            = 2*pi*(3e8)/Lam;

fem.const.yo_bot       = -Lam/2*(4*b+e);

fem.const.yo_up        = Lam/2*(4*b+e+2*So);

if barj = =1

   fem.const.es_quartz   =  1;

   fem.const.es_Au       =  1;

else

   fem.const.es_quartz   =  1;

   fem.const.es_Au       =   real(esAu) - 1i*imag(esAu);

end


% EXPRESSIONS IN FEM STRUCUTRE.

fem.equ.expr.Ex        = 'cu1y/(es_0*i*W)';

fem.equ.expr.Ey        = 'cu1x/(es_0*i*W)';

fem.equ.expr.E         = 'sqrt(Ex*conj(Ex)+Ey*conj(Ey))';

fem.equ.expr.H         = 'sqrt(U*conj(U))';

fem.equ.expr.Sx        = '-U/Ux*cu1x^2*cO/(k*sqrt(-1))';

fem.equ.expr.Sy        = '-U/Uy*cu1y^2*cO/(k*sqrt(-1))';

fem.equ.expr.f_y_bot = '1-i*sigma/W*((y-yo_bot)/L_PML)^m';

fem.equ.expr.f_y_up  = '1-i*sigma/W*((y-yo_up)/L_PML)^m';
```
129

```matlab
fem.equ.expr.source   = 'exp(i*k*sin(teta)*x)';

fem.equ.expr.period   = 'exp(-i*Lx*k*sin(teta))';


% INITIALIZE THE MESH
fem.mesh = meshinit(fem,'hmax',6e-8);

fem.mesh = meshrefine(fem,'sdl',[11],'rmethod','regular');


% COUPLING VARIABLE ELEMENTS (PERIODIC BOUNDARY CONDITIONS)
clear elem
elem{1} = struct('elem',{'elcplextr'},...
'var',{{'pconstr1','pconstr2','pconstr3','pconstr4','pconstr5','pconstr6','pconstr7','pconstr8','pconstr9','pconstr10'}},...
            'g',{{'1'}},...
            'src',{{{{},struct('expr',{{{'U',{},{},{},{},{},{},{},{},{},{}},
{{},{},'U',{},{},{},{},{},{},{},{}}, {{},{},{},'U',{},{},{},{},{},{},{}},
{{},{},{},{},'U',{},{},{},{},{},{},{}}, {{},{},{},{},{},'U',{},{},{},{},{}},
{{},{},{},{},{},{},'U',{},{},{},{}}, {{},{},{},{},{},{},{},'U',{},{},{}},
{{},{},{},{},{},{},{},{},'U',{},{}}, {{},{},{},{},{},{},{},{},{},'U',{}},
{{},{},{},{},{},{},{},{},{},{},'U'}}},...
                   'map',{{'0','0','0','0','0','0','0','0','0','0'}},...
'ind',{{{'1'},{'2','4','6','8','10','12','14','16','18','20','21','22','23','24','25','26','27','28','29','30','31','32','33','34','35','36','37','38','39'},{'3'},{'5'},{'7'},{'9'},{'11'},{'13'},{'15'},{'17'},{'19'}}})},{{}}}},...
```

```matlab
'geomdim',{{{{},struct('map',{{{{},'1',{},{},{},{},{},{},{},{},{}},{{},{},{},'2',{},{},{},{},
{},{},{},{}},{{},{},{},'3',{},{},{},{},{},{},{}},{{},{},{},{},'4',{},{},{},{},{},{},{}},{{},{
},{},{},'5',{},{},{},{},{}},{{},{},{},{},{},{},'6',{},{},{},{}},{{},{},{},{},{},{},{},{},'7'
,{},{},{}},{{},{},{},{},{},{},{},{},'8',{},{}},{{},{},{},{},{},{},{},{},{},{},'9',{}},{{},{},
{},{},{},{},{},{},'10'}}},...
'ind',{{{'1','2','3','4','5','6','7','8','9','10','11','12','13','14','15','16','17','18','19','20','21','22','23',
'24','25','26','27','28','29'},{'30'},{'31'},{'32'},{'33'},{'34'},{'35'},{'36'},{'37'},{'38'},{'39'}
}}),{}}}},...
'map',{{struct('type',{'linear'},'sg',{'1'},'sv',{{'18','19'}},'dg',{'1'},'dv',{{'1','2'}}),...
struct('type',{'linear'},'sg',{'1'},'sv',{{'19','20'}},'dg',{'1'},'dv',{{'2','3'}}),...
struct('type',{'linear'},'sg',{'1'},'sv',{{'20','21'}},'dg',{'1'},'dv',{{'3','4'}}),...
struct('type',{'linear'},'sg',{'1'},'sv',{{'21','22'}},'dg',{'1'},'dv',{{'4','5'}}),...
struct('type',{'linear'},'sg',{'1'},'sv',{{'22','23'}},'dg',{'1'},'dv',{{'5','6'}}),...
struct('type',{'linear'},'sg',{'1'},'sv',{{'23','24'}},'dg',{'1'},'dv',{{'6','7'}}),...
struct('type',{'linear'},'sg',{'1'},'sv',{{'24','25'}},'dg',{'1'},'dv',{{'7','8'}}),...
struct('type',{'linear'},'sg',{'1'},'sv',{{'25','26'}},'dg',{'1'},'dv',{{'8','9'}}),...
struct('type',{'linear'},'sg',{'1'},'sv',{{'26','27'}},'dg',{'1'},'dv',{{'9','10'}}),...
struct('type',{'linear'},'sg',{'1'},'sv',{{'27','28'}},'dg',{'1'},'dv',{{'10','11'}})}});

    elem{2} = struct('elem',{'elpconstr'},...

                'g',{{'1'}},...

                'geomdim',{{{{},struct('constr',{{{'pconstr1-
(U*period)','0','0','0','0','0','0','0','0','0'},{'0','pconstr2-
(U*period)','0','0','0','0','0','0','0','0'},{'0','0','pconstr3-
```

```
(U*period)','0','0','0','0','0','0','0'},{'0','0','0','pconstr4-
(U*period)','0','0','0','0','0','0'},{'0','0','0','0','pconstr5-
(U*period)','0','0','0','0','0'},{'0','0','0','0','0','pconstr6-
(U*period)','0','0','0','0'},{'0','0','0','0','0','0','pconstr7-
(U*period)','0','0','0'},{'0','0','0','0','0','0','0','pconstr8-
(U*period)','0','0'},{'0','0','0','0','0','0','0','0','pconstr9-
(U*period)','0'},{'0','0','0','0','0','0','0','0','0','pconstr10-(U*period)'}}},...
'cpoints',{{{'2','2','2','2','2','2','2','2','2','2'},{'2','2','2','2','2','2','2','2','2','2'},{'2','2','2','2','2','2','
2','2','2','2'},{'2','2','2','2','2','2','2','2','2','2'},{'2','2','2','2','2','2','2','2','2','2'},{'2','2','2','2','2','2'
,'2','2','2','2'},{'2','2','2','2','2','2','2','2','2','2'},{'2','2','2','2','2','2','2','2','2','2'},{'2','2','2','2','2','
2','2','2','2','2'},{'2','2','2','2','2','2','2','2','2','2'}}},...
'ind',{{{'30'},{'31'},{'32'},{'33'},{'34'},{'35'},{'36'},{'37'},{'38'},{'39'}}}}),{}}}});
   fem.elemcpl = elem;


   % DEFINE THE BOUNDARY CONDITIONS
   fem.bnd.q={0};
   fem.bnd.g={0};
   fem.bnd.type={'neu'};
   % SPECIFY THE PDE COEFFICIENTS
   fem.equ.c = {{{'f_y_bot','0';'0','1/f_y_bot'}}, {{'1'}}, {{'1'}}, {{'1/es_quartz'}},
{{'1/es_Au'}}, {{'1/es_quartz'}}, {{'1'}}, {{'1'}}, {{'1'}}, {{'f_y_up','0';'0','1/f_y_up'}},
{{'1/es_quartz'}}, {{'1/es_Au'}}};
```

```matlab
    fem.equ.a = {{'-(k^2)*f_y_bot'}, {'-k^2'}, {'-k^2'}, {'-k^2'}, {'-k^2'}, {'-k^2'}, {'-k^2'},
{'-k^2'}, {'-k^2'}, {'-(k^2)*f_y_up'}, {'-k^2'}, {'-k^2'}};
    fem.equ.f = {{'0'}, {'0'}, {'0'}, {'0'}, {'0'}, {'0'}, {'0'}, {'0'}, {'source'}, {'0'}, {'0'},
{'0'}};
    fem.equ.ind = [1,2,3,4,5,6,7,8,9,10,11,12];


    % SOLVE THE PROBLEM
    fem.xmesh=meshextend(fem);
    fem.sol=femlin(fem);
    ElectricFlux(bari,barj) = 0;
    ElectricFlux(bari,barj) = ElectricFlux(bari,barj) +
postint(fem,'E*conj(E)','dl',[6],'edim',1,'intorder',4,'geomnum',1,'solnum',1,'phase',(0)*pi/
180);
end
Transmittance_ConvDiv(bari)= ElectricFlux(bari,2)/ElectricFlux(bari,1);
save('Final_Au_Transmittance_ConvDiv_Final_5nm_gap_moredata.dat','Transmittance_
ConvDiv','-tabs','-ascii')
end
```

Bibilography

Astilean, S., Lalanne, P. & Palamaru, M. Light transmission through metallic channels much smaller than the wavelength *Optics Communications* **175,**265-273 (2000).

Azad, A. K. & Zhang, W. L. Resonant terahertz transmission in subwavelength metallic hole arrays of sub-skin-depth thickness *Optics Letters* **30,**2945-2947 (2005).

Azad, A. K., Zhao, Y. & Zhang, W. Transmission properties of terahertz pulses through an ultrathin subwavelength silicon hole array *Applied Physics Letters* **86,**- (2005).

Barber, P. W. & Hill, S. C. *Light scattering by particles : computational methods* (World Scientific, Singapore ; Teaneck, N.J.,1990).

Barnes, W. L., Murray, W. A., Dintinger, J., Devaux, E. & Ebbesen, T. W. Surface plasmon polaritons and their role in the enhanced transmission of light through periodic arrays of subwavelength holes in a metal film *Physical Review Letters* **92,**- (2004).

Barnes, W. L., Preist, T. W., Kitson, S. C. & Sambles, J. R. Physical origin of photonic energy gaps in the propagation of surface plasmons on gratings *Physical Review B* **54,**6227-6244 (1996).

Belotelov, V. I., Doskolovich, L. L. & Zvezdin, A. K. Extraordinary magneto-optical effects and transmission through metal-dielectric plasmonic systems *Physical Review Letters* **98,**- (2007).

Ben-Abdallah, P. Thermal antenna behavior for thin-film structures *Journal of the Optical Society of America a-Optics Image Science and Vision* **21,**1368-1371 (2004).

Bergman, D. J. & Strelniker, Y. M. Anisotropic ac electrical permittivity of a periodic metal-dielectric composite film in a strong magnetic field *Physical Review Letters* **80,**857-860 (1998).

Bethe, H. A. Theory of Diffraction by Small Holes *Physical Review* **66,**163-182 (1944).

Betzig, E. & Trautman, J. K. Near-Field Optics - Microscopy, Spectroscopy, and Surface Modification Beyond the Diffraction Limit *Science* **257,**189-195 (1992).

Binnig, G., Frank, K. H., Fuchs, H., Garcia, N., Reihl, B., Rohrer, H., Salvan, F. & Williams, A. R. Tunneling Spectroscopy and Inverse Photoemission - Image and Field States *Physical Review Letters* **55,**991-994 (1985).

Binnig, G., Rohrer, H., Gerber, C. & Weibel, E. 7x7 Reconstruction on Si(111) Resolved in Real Space *Physical Review Letters* **50,**120-123 (1983).

Binnig, G., Rohrer, H., Gerber, C. & Weibel, E. Tunneling through a Controllable Vacuum Gap *Applied Physics Letters* **40,**178-180 (1982).

Boisdé, G. & Harmer, A. *Chemical and biochemical sensing with optical fibers and waveguides* (Artech House, Boston,1996).

Cao, H. & Nahata, A. Influence of aperture shape on the transmission properties of a periodic array of subwavelength apertures *Optics Express* **12,**3664-3672 (2004).

Cao, Q. & Lalanne, P. Negative role of surface plasmons in the transmission of metallic gratings with very narrow slits *Physical Review Letters* **88,**- (2002).

Carminati, R. & Greffet, J. J. Near-field effects in spatial coherence of thermal sources *Physical Review Letters* **82,**1660-1663 (1999).

Celanovic, I., Perreault, D. & Kassakian, J. Resonant-cavity enhanced thermal emission *Physical Review B* **72,**- (2005).

Collin, S., Pardo, F., Teissier, R. & Pelouard, J. L. Horizontal and vertical surface resonances in transmission metallic gratings *Journal of Optics a-Pure and Applied Optics* **4,**S154-S160 (2002).

Degiron, A., Lezec, H. J., Barnes, W. L. & Ebbesen, T. W. Effects of hole depth on enhanced light transmission through subwavelength hole arrays *Applied Physics Letters* **81,**4327-4329 (2002).

Dionne, J. A., Sweatlock, L. A., Atwater, H. A. & Polman, A. Planar metal plasmon waveguides: frequency-dependent dispersion, propagation, localization, and loss beyond the free electron model *Physical Review B* **72,**- (2005).

Diwekar, M., Kamaev, V., Shi, J. & Vardeny, Z. V. Optical and magneto-optical studies of two-dimensional metallodielectric photonic crystals on cobalt films *Applied Physics Letters* **84,**3112-3114 (2004).

Dolgaev, S. I., Lyalin, A. A., Shafeev, G. A. & Voronov, V. V. Fast etching and metallization of SiC ceramics with copper-vapor-laser radiation *Applied Physics a-Materials Science & Processing* **63,**75-79 (1996).

Dong, Y. Y., Zorman, C. & Molian, P. Femtosecond pulsed laser micromachining of single crystalline 3C-SiC structures based on a laser-induced defect-activation process *Journal of Micromechanics and Microengineering* **13,**680-685 (2003).

Dresselhaus, G., Kip, A. F. & Kittel, C. Cyclotron Resonance of Electrons and Holes in Silicon and Germanium Crystals *Physical Review* **98,**368-384 (1955).

Ebbesen, T. W., Lezec, H. J., Ghaemi, H. F., Thio, T. & Wolff, P. A. Extraordinary optical transmission through sub-wavelength hole arrays *Nature* **391,**667-669 (1998).

Fan, W. J., Zhang, S., Minhas, B., Malloy, K. J. & Brueck, S. R. J. Enhanced infrared transmission through subwavelength coaxial metallic arrays *Physical Review Letters* **94,**- (2005).

Fleming, J. G., Lin, S. Y., El-Kady, I., Biswas, R. & Ho, K. M. All-metallic three-dimensional photonic crystals with a large infrared bandgap *Nature* **417,**52-55 (2002).

Foteinopoulou, S. & Soukoulis, C. M. Negative refraction and left-handed behavior in two-dimensional photonic crystals *Physical Review B* **67,**- (2003).

Garcia-Martin, A., Armelles, G. & Pereira, S. Light transport in photonic crystals composed of magneto-optically active materials *Physical Review B* **71,**- (2005).

Garcia-Vidal, F. J. & Martin-Moreno, L. Transmission and focusing of light in one-dimensional periodically nanostructured metals *Physical Review B* **66,**- (2002).

Genet, C. & Ebbesen, T. W. Light in tiny holes *Nature* **445,**39-46 (2007).

Girard, C., Joachim, C. & Gauthier, S. The physics of the near-field *Reports on Progress in Physics* **63,**893-938 (2000).

Glezer, E. N. & Mazur, E. Ultrafast-laser driven micro-explosions in transparent materials *Applied Physics Letters* **71,**882-884 (1997).

Gordon, R., Brolo, A. G., McKinnon, A., Rajora, A., Leathem, B. & Kavanagh, K. L. Strong polarization in the optical transmission through elliptical nanohole arrays *Physical Review Letters* **92,**- (2004).

Greffet, J. J., Carminati, R., Joulain, K., Mulet, J. P., Mainguy, S. P. & Chen, Y. Coherent emission of light by thermal sources *Nature* **416,**61-64 (2002).

Greffet, J. J. & Nieto-Vesperinas, M. Field theory for generalized bidirectional reflectivity: derivation of Helmholtz's reciprocity principle and Kirchhoff's law *Journal of the Optical Society of America a-Optics Image Science and Vision* **15,**2735-2744 (1998).

Grupp, D. E., Lezec, H. J., Ebbesen, T. W., Pellerin, K. M. & Thio, T. Crucial role of metal surface in enhanced transmission through subwavelength apertures *Applied Physics Letters* **77,**1569-1571 (2000).

Hasek, T., Kurt, H., Citrin, D. S. & Koch, M. Photonic crystals for fluid sensing in the subterahertz range *Applied Physics Letters* **89,**- (2006).

Hecht, B., Bielefeldt, H., Novotny, L., Inouye, Y. & Pohl, D. W. Local excitation, scattering, and interference of surface plasmons *Physical Review Letters* **77,**1889-1892 (1996).

Heinzel, A., Boerner, V., Gombert, A., Blasi, B., Wittwer, V. & Luther, J. Radiation filters and emitters for the NIR based on periodically structured metal surfaces *Journal of Modern Optics* **47,**2399-2419 (2000).

Heltzel, A., Battula, A., Howell, J. R. & Chen, S. C. Nanostructuring borosilicate glass with near-field enhanced energy using a femtosecond laser pulse *Journal of Heat Transfer-Transactions of the Asme* **129,**53-59 (2007).

Heltzel, A. J., Theppakuttai, S., Howell, J. R. & Chen, S. C. Analytical and experimental investigation of laser-microsphere interaction for nanoscale surface modification *Journal of Heat Transfer-Transactions of the Asme* **127,**1231-1235 (2005).

Henkel, C., Joulain, K., Carminati, R. & Greffet, J. J. Spatial coherence of thermal near fields *Optics Communications* **186,**57-67 (2000).

Hesketh, P. J., Zemel, J. N. & Gebhart, B. Organ Pipe Radiant Modes of Periodic Micromachined Silicon Surfaces *Nature* **324,**549-551 (1986).

Houck, A. A., Brock, J. B. & Chuang, I. L. Experimental observations of a left-handed material that obeys Snell's law *Physical Review Letters* **90,**- (2003).

Ikawa, T., Mitsuoka, T., Hasegawa, M., Tsuchimori, M., Watanabe, O. & Kawata, Y. Azobenzene polymer surface deformation due to the gradient force of the optical near field of monodispersed polystyrene spheres *Physical Review B* **64,**- (2001).

Itoh, N. Bond scission induced by electronic excitation in solids: A tool for nanomanipulation *Nuclear Instruments & Methods in Physics Research Section B-Beam Interactions with Materials and Atoms* **122,**405-409 (1997).

Jackson, J. D. *Classical electrodynamics* (Wiley, New York,1999).

Janke, C., Rivas, J. G., Schotsch, C., Beckmann, L., Bolivar, P. H. & Kurz, H. Optimization of enhanced terahertz transmission through arrays of subwavelength apertures *Physical Review B* **69,**- (2004).

Jia, W. L. & Liu, X. H. Origin of superenhanced light transmission through two-dimensional subwavelength rectangular hole arrays *European Physical Journal B* **46,**343-347 (2005).

Jiao, X., Wang, P., Tang, L., Lu, Y., Li, Q., Zhang, D., Yao, P., Ming, H. & Xie, J. Fabry-Perot-like phenomenon in the surface plasmons resonant transmission of metallic gratings with very narrow slits *Applied Physics B-Lasers and Optics* **80,**301-305 (2005).

Joannopoulos, J. D., Meade, R. D. & Winn, J. N. *Photonic crystals : molding the flow of light* (Princeton University Press, Princeton, N.J.,1995).

Kitson, S. C., Barnes, W. L. & Sambles, J. R. Full photonic band gap for surface modes in the visible *Physical Review Letters* **77,**2670-2673 (1996).

Koerkamp, K. J. K., Enoch, S., Segerink, F. B., van Hulst, N. F. & Kuipers, L. Strong influence of hole shape on extraordinary transmission through periodic arrays of subwavelength holes *Physical Review Letters* **92,**- (2004).

Korte, F., Serbin, J., Koch, J., Egbert, A., Fallnich, C., Ostendorf, A. & Chichkov, B. N. Towards nanostructuring with femtosecond laser pulses *Applied Physics a-Materials Science & Processing* **77,**229-235 (2003).

Kraus, J. D. *Antennas* (McGraw-Hill, New York,,1950).

Kreiter, M., Oster, J., Sambles, R., Herminghaus, S., Mittler-Neher, S. & Knoll, W. Thermally induced emission of light from a metallic diffraction grating, mediated by surface plasmons *Optics Communications* **168,**117-122 (1999).

Kurt, H. & Citrin, D. S. Photonic crystals for biochemical sensing in the terahertz region *Applied Physics Letters* **87,**- (2005).

Laroche, M., Carminati, R. & Greffet, J. J. Coherent thermal antenna using a photonic crystal slab *Physical Review Letters* **96,**- (2006).

Lavrinenko, A., Borel, P. I., Frandsen, L. H., Thorhauge, M., Harpoth, A., Kristensen, M., Niemi, T. & Chong, H. M. H. Comprehensive FDTD modelling of photonic crystal waveguide components *Optics Express* **12,**234-248 (2004).

Lee, B. J., Fu, C. J. & Zhang, Z. M. Coherent thermal emission from one-dimensional photonic crystals *Applied Physics Letters* **87,**- (2005).

LeGall, J., Olivier, M. & Greffet, J. J. Experimental and theoretical study of reflection and coherent thermal emission by a SiC grating supporting a surface-phonon polariton *Physical Review B* **55,**10105-10114 (1997).

Lezec, H. J. & Thio, T. Diffracted evanescent wave model for enhanced and suppressed optical transmission through subwavelength hole arrays *Optics Express* **12,**3629-3651 (2004).

Li, Z. Y. & Lin, L. L. Evaluation of lensing in photonic crystal slabs exhibiting negative refraction *Physical Review B* **68,**- (2003).

Lide, D. R. *handbook of chemistry and physics* (CRC Press, Cleveland, Ohio,1992).

Lin, S. Y., Moreno, J. & Fleming, J. G. Three-dimensional photonic-crystal emitter for thermal photovoltaic power generation *Applied Physics Letters* **83,**380-382 (2003).

Loncar, M., Scherer, A. & Qiu, Y. M. Photonic crystal laser sources for chemical detection *Applied Physics Letters* **82,**4648-4650 (2003).

Lu, Y. & Chen, S. C. Nanopatterning of a silicon surface by near-field enhanced laser irradiation *Nanotechnology* **14,**505-508 (2003).

Lu, Y., Theppakuttai, S. & Chen, S. C. Marangoni effect in nanosphere-enhanced laser nanopatterning of silicon *Applied Physics Letters* **82,**4143-4145 (2003).

Luo, C., Johnson, S. G., Joannopoulos, J. D. & Pendry, J. B. All-angle negative refraction without negative effective index *Physical Review B* **65,**- (2002).

Maier, S. A. & Atwater, H. A. Plasmonics: Localization and guiding of electromagnetic energy in metal/dielectric structures *Journal of Applied Physics* **98,**- (2005).

Marquier, F., Joulain, K., Mulet, J. P., Carminati, R., Greffet, J. J. & Chen, Y. Coherent spontaneous emission of light by thermal sources *Physical Review B* **69,**- (2004).

Martin-Moreno, L., Garcia-Vidal, F. J., Lezec, H. J., Pellerin, K. M., Thio, T., Pendry, J. B. & Ebbesen, T. W. Theory of extraordinary optical transmission through subwavelength hole arrays *Physical Review Letters* **86,**1114-1117 (2001).

Matteo, J. A., Fromm, D. P., Yuen, Y., Schuck, P. J., Moerner, W. E. & Hesselink, L. Spectral analysis of strongly enhanced visible light transmission through single C-shaped nanoapertures *Applied Physics Letters* **85,**648-650 (2004).

Maystre, D. & Neviere, M. Quantitative Theoretical-Study on Plasmon Anomalies of Diffraction Gratings *Journal of Optics-Nouvelle Revue D Optique* **8,**165-174 (1977).

Miyamaru, F. & Hangyo, M. Finite size effect of transmission property for metal hole arrays in subterahertz region *Applied Physics Letters* **84,**2742-2744 (2004).

Moussa, R., Foteinopoulou, S., Zhang, L., Tuttle, G., Guven, G. T. K., Ozbay, E. & Soukoulis, C. M. Negative refraction and superlens behavior in a two-dimensional photonic crystal *Physical Review B* **71,**- (2005).

Munzer, H. J., Mosbacher, M., Bertsch, M., Zimmermann, J., Leiderer, P. & Boneberg, J. Local held enhancement effects for nanostructuring of surfaces *Journal of Microscopy-Oxford* **202,**129-135 (2001).

Narayanaswamy, A. & Chen, G. Thermal emission control with one-dimensional metallodielectric photonic crystals *Physical Review B* **70,**- (2004).

Nishio, K. & Masuda, H. Dependence of optical properties of ordered metal hole array on refractive index of surrounding medium *Electrochemical and Solid State Letters* **7,**H27-H28 (2004).

O'Hara, J. F., Averitt, R. D. & Taylor, A. J. Terahertz surface plasmon polariton coupling on metallic gratings *Optics Express* **12,**6397-6402 (2004).

Oldenburg, S. J., Averitt, R. D., Westcott, S. L. & Halas, N. J. Nanoengineering of optical resonances *Chemical Physics Letters* **288,**243-247 (1998).

Ozbay, E. Plasmonics: Merging photonics and electronics at nanoscale dimensions *Science* **311,**189-193 (2006).

Palik, E. D. (1985) in *Academic Press handbook series* (Academic Press, Orlando), pp. xviii, 804.

Pan, C. L., Hsieh, C. F., Pan, R. P., Tanaka, M., Miyamaru, F., Tani, M. & Hangyo, M. Control of enhanced THz transmission through metallic hole arrays using nematic liquid crystal *Optics Express* **13,**3921-3930 (2005).

Park, D. S., Cho, M. W., Lee, H. & Cho, W. S. Micro-grooving of glass using micro-abrasive jet machining *Journal of Materials Processing Technology* **146,**234-240 (2004).

Pendry, J. B. Negative refraction makes a perfect lens *Physical Review Letters* **85,**3966-3969 (2000).

Pendry, J. B., Holden, A. J., Robbins, D. J. & Stewart, W. J. Low frequency plasmons in thin-wire structures *Journal of Physics-Condensed Matter* **10,**4785-4809 (1998).

Pendry, J. B., Martin-Moreno, L. & Garcia-Vidal, F. J. Mimicking surface plasmons with structured surfaces *Science* **305,**847-848 (2004).

Popov, E., Neviere, M., Enoch, S. & Reinisch, R. Theory of light transmission through subwavelength periodic hole arrays *Physical Review B* **62,**16100-16108 (2000).

Porto, J. A., Garcia-Vidal, F. J. & Pendry, J. B. Transmission resonances on metallic gratings with very narrow slits *Physical Review Letters* **83,**2845-2848 (1999).

Prasad, P. N. *Nanophotonics* (Wiley-Interscience, Hoboken, N.J.,2004).

Qu, D. X., Grischkowsky, D. & Zhang, W. L. Terahertz transmission properties of thin, subwavelength metallic hole arrays *Optics Letters* **29,**896-898 (2004).

Raether, H. *Surface plasmons on smooth and rough surfaces and on gratings* (Springer-Verlag, Berlin ; New York,1988).

Reitano, R., Baeri, P. & Marino, N. Excimer laser induced thermal evaporation and ablation of silicon carbide *Applied Surface Science* **96-8,**302-308 (1996).

Rivas, J. G., Schotsch, C., Bolivar, P. H. & Kurz, H. Enhanced transmission of THz radiation through subwavelength holes *Physical Review B* **68,**- (2003).

Sai, H., Yugami, H., Akiyama, Y., Kanamori, Y. & Hane, K. Spectral control of thermal emission by periodic microstructured surfaces in the near-infrared region *Journal of the Optical Society of America a-Optics Image Science and Vision* **18,**1471-1476 (2001).

Sakoda, K. *Optical Properties of Photonic Crystals* (Springer, Berlin,2001).

Sambles, R. Photonics - More than transparent *Nature* **391,**641-642 (1998).

Sciti, D. & Bellosi, A. Laser-induced surface drilling of silicon carbide *Applied Surface Science* **180,**92-101 (2001).

Shchegrov, A. V., Joulain, K., Carminati, R. & Greffet, J. J. Near-field spectral effects due to electromagnetic surface excitations *Physical Review Letters* **85,**1548-1551 (2000).

Shelby, R. A., Smith, D. R. & Schultz, S. Experimental verification of a negative index of refraction *Science* **292,**77-79 (2001).

Shi, X. L., Hesselink, L. & Thornton, R. L. Ultrahigh light transmission through a C-shaped nanoaperture *Optics Letters* **28,**1320-1322 (2003).

Smith, D. R., Padilla, W. J., Vier, D. C., Nemat-Nasser, S. C. & Schultz, S. Composite medium with simultaneously negative permeability and permittivity *Physical Review Letters* **84,**4184-4187 (2000).

Soukoulis, C. M., Kafesaki, M. & Economou, E. N. Negative-index materials: New frontiers in optics *Advanced Materials* **18,**1941-1952 (2006).

Strelniker, Y. M. & Bergman, D. J. Optical transmission through metal films with a subwavelength hole array in the presence of a magnetic field *Physical Review B* **59,**12763-12766 (1999).

Sugioka, K., Obata, K., Midorikawa, K., Hong, M. H., Wu, D. J., Wong, L. L., Lu, Y. F. & Chong, T. C. Advanced materials processing based on interaction of laser beam and a medium *Journal of Photochemistry and Photobiology a-Chemistry* **158,**171-178 (2003).

Sundaram, S. K. & Mazur, E. Inducing and probing non-thermal transitions in semiconductors using femtosecond laser pulses *Nature Materials* **1,**217-224 (2002).

Tanaka, M., Miyamaru, F., Hangyo, M., Tanaka, T., Akazawa, M. & Sano, E. Effect of a thin dielectric layer on terahertz transmission characteristics for metal hole arrays *Optics Letters* **30,**1210-1212 (2005).

Theppakuttai, S. & Chen, S. Nanoscale surface modification of glass using a 1064 nm pulsed laser *Applied Physics Letters* **83,**758-760 (2003).

Theppakuttai, S. & Chen, S. C. Submicron ripple formation on glass surface upon laser-nanosphere interaction *Journal of Applied Physics* **95,**5049-5052 (2004).

Urzhumov, Y. A. & Shvets, G. Extreme anisotropy of wave propagation in two-dimensional photonic crystals *Physical Review E* **72,**- (2005).

van der Molen, K. L., Segerink, F. B., van Hulst, N. F. & Kuipers, L. Influence of hole size on the extraordinary transmission through subwavelength hole arrays *Applied Physics Letters* **85,**4316-4318 (2004).

Vinogradov, E. A., Zhizhin, G. N., Malshukov, A. G. & Yudson, V. I. Thermostimulated Polariton Emission of Zinc Selenide Films on Metal-Substrate *Solid State Communications* **23,**915-921 (1977).

Wang, Q. J., Li, J. Q., Huang, C. P., Zhang, C. & Zhu, Y. Y. Enhanced optical transmission through metal films with rotation-symmetrical hole arrays *Applied Physics Letters* **87,**- (2005).

Wang, X. & Kempa, K. Negative refraction and subwavelength lensing in a polaritonic crystal *Physical Review B* **71,**- (2005).

Wang, Z. B., Hong, M. H., Luk'yanchuk, B. S., Huang, S. M., Wang, Q. F., Shi, L. P. & Chong, T. C. Parallel nanostructuring of GeSbTe film with particle mask *Applied Physics a-Materials Science & Processing* **79,**1603-1606 (2004).

Wang, Z. B., Hong, M. H., Luk'yanchuk, B. S., Lin, Y., Wang, Q. F. & Chong, T. C. Angle effect in laser nanopatterning with particle-mask *Journal of Applied Physics* **96,**6845-6850 (2004).

Watanabe, O., Ikawa, T., Hasegawa, M., Tsuchimori, M. & Kawata, Y. Nanofabrication induced by near-field exposure from a nanosecond laser pulse *Applied Physics Letters* **79,**1366-1368 (2001).

Wolf, E. Non-Cosmological Redshifts of Spectral-Lines *Nature* **326,**363-365 (1987).

Wolf, E. & James, D. F. V. Correlation-induced spectral changes *Reports on Progress in Physics* **59,**771-818 (1996).

Xie, Y., Zakharian, A. R., Moloney, J. V. & Mansuripur, M. Transmission of light through slit apertures in metallic films *Optics Express* **12,**6106-6121 (2004).

Yan, B. H., Wang, A. C., Huang, C. Y. & Huang, F. Y. Study of precision micro-holes in borosilicate glass using micro EDM combined with micro ultrasonic vibration machining *International Journal of Machine Tools & Manufacture* **42,**1105-1112 (2002).

Ye, Y. H., Jeong, D. Y. & Zhang, Q. M. Fabrication of strain tunable infrared frequency selective surfaces on electrostrictive poly(vinylidene fluoride-trifluoroethylene) copolymer films using a stencil mask method *Applied Physics Letters* **85,**654-656 (2004).

140

Youn, S. W. & Kang, C. G. Maskless patterning of borosilicate glass nanoindentation-induced etch-hillock surface using phenomena *Journal of Non-Crystalline Solids* **351,**3065-3074 (2005).

Zayats, A. V. & Smolyaninov, I. I. Near-field photonics: surface plasmon polaritons and localized surface plasmons *Journal of Optics a-Pure and Applied Optics* **5,**S16-S50 (2003).

Zayats, A. V., Smolyaninov, I. I. & Maradudin, A. A. Nano-optics of surface plasmon polaritons *Physics Reports-Review Section of Physics Letters* **408,**131-314 (2005).

Zhang, J., Sugioka, K. & Midorikawa, K. High-quality and high-efficiency machining of glass materials by laser-induced plasma-assisted ablation using conventional nanosecond UV, visible, and infrared lasers *Applied Physics a-Materials Science & Processing* **69,**S879-S882 (1999).

Zhang, J., Sugioka, K., Wada, S., Tashiro, H. & Toyoda, K. Direct photoetching of single crystal SiC by VUV 266 nm multiwavelength laser ablation *Applied Physics a-Materials Science & Processing* **64,**367-371 (1997).

Zhang, X. D. Subwavelength far-field resolution in a square two-dimensional photonic crystal *Physical Review E* **71,**- (2005).

Zheng, Y. W., Luk'yanchuk, B. S., Lu, Y. F., Song, W. D. & Mai, Z. H. Dry laser cleaning of particles from solid substrates: Experiments and theory *Journal of Applied Physics* **90,**2135-2142 (2001).

Zhou, Y., Hong, M. H., Fuh, J. Y. H., Lu, L., Luk'yanchuk, B. S., Wang, Z. B., Shi, L. P. & Chong, T. C. Direct femtosecond laser nanopatterning of glass substrate by particle-assisted near-field enhancement *Applied Physics Letters* **88,**- (2006).

Zvezdin, A. K. & Kotov, V. A. *Modern magnetooptics and magnetooptical materials* (Institute of Physics Pub., Bristol ; Philadelphia, PA,1997).

Vita

Arvind Battula was born in Nuzividu, Krishna District, Andhra Pradesh, India on July 23rd 1979. He is the eldest son of Mr. Raja Ramana Reddy Battula and Mrs. Meena Kumari. After finishing from St. Paul's High School from his home town Hyderabad, A.P., India, he joined Indian Institute of Technology Madras, India to pursue his Bachelors in Chemical Engineering. Subsequently he got interested in the field of Computational Fluid Dynamics and started pursuing his graduate studies at Clemson University in Mechanical Engineering. After Masters he further wanted to do Ph.D and got into the University of Texas at Austin. Where, he did his research work in the general area of nanoscience and nanotechnology but with special emphasis in Nano-optics. He got married on March 18th 2006 and is expecting a baby in the first week of December 2007.

Permanent address: 2-2-1133/5/7, New Nallakunta, Hyderabad, A.P., India - 500044

This dissertation was typed by Arvind Battula.